Development of a measurement setup for dielectric characterization of SF6-free alternative gases

Tim Plantfeber

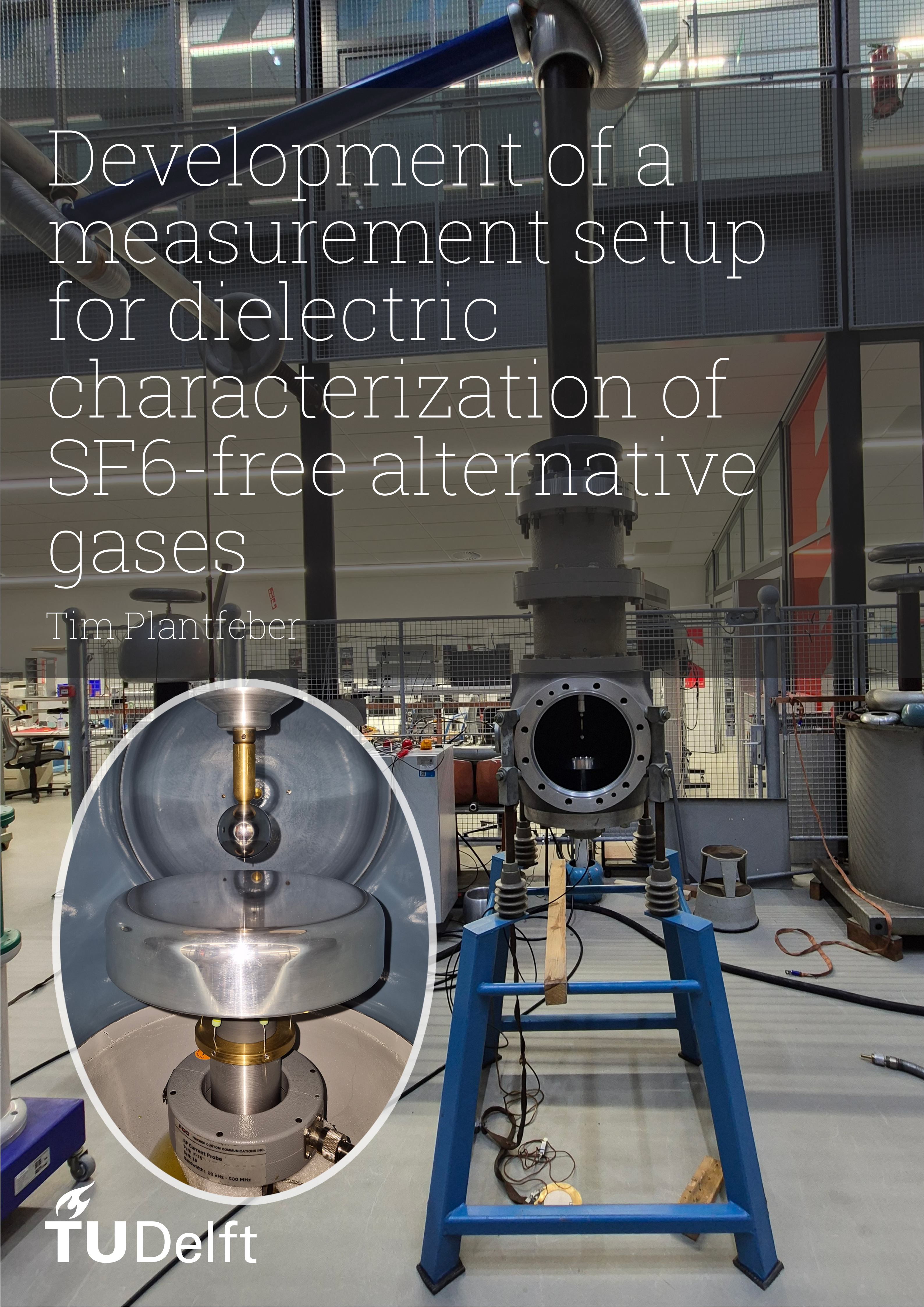

Development of a measurement setup for dielectric characterization of SF6-free alternative gases

by

Tim Plantfeber

to obtain the degree of Master of Science
at the Delft University of Technology,
to be defended publicly on Friday 8th, August 2025 at 13:00.

Student number:	4590848	
Project duration:	November 11, 2024 – August 8, 2025	
Thesis committee:	Prof. ir. P.T.M. Vaessen,	TU Delft, supervisor
	Dr. ir. D. van der Born,	TU Delft, daily supervisor
	Ir. A.G.A. Lathouwers,	TU Delft
	Dr. ir. S.A. Rivera,	TU Delft, committee

TU Delft

Abstract

The transition away from SF_6-based insulation in high-voltage equipment has accelerated interest in alternative gas mixtures with lower environmental impact. One such mixture is CO_2/O_2 (70%/30%), which is used as a carrier gas in C4-FN based mixtures but is also being explored for stand-alone insulation applications. To enable detailed characterisation of partial discharges (PDs) in such alternative gases, a high-bandwidth measurement setup was developed.

The setup is based on a custom designed test compartment that uses a needle-to-plane electrode configuration to generate corona discharges and applies a high-frequency current transformer (HFCT) as a measurement impedance.

Initial measurements using a conventional IEC 60270 configuration revealed a resonance frequency of 3.5 MHz, which limited the effective bandwidth of the system. By eliminating the traditional coupling capacitor and instead using the inherent capacitance between the conductor in the bushing and the grounded enclosure as a coupling path, the resonance frequency was shifted to 144 MHz. Aside from the significant increase in bandwidth, this also improved sensitivity.

The frequency response of each segment of the measurement circuit was characterised, allowing the derivation of the PD current from the measured voltage and enabling calibration-free charge estimation.

The setup was used to study the PD behaviour in a CO_2/O_2 (70%/30%) mixture at pressures ranging from 0.2 to 0.4 MPa and voltages up to 1.5 times the PD inception voltage. A novel phenomenon was observed: certain PDs were rapidly followed by another discharge, after which a longer interval was required for the next event.

Multiple charge estimation methods were adapted to suit the measurement circuit. After evaluation, the modified frequency domain method demonstrated the strongest correlation with peak current, especially at low discharge magnitudes. These results demonstrate that the developed measurement setup is suitable for detailed PD analysis in alternative gases and that it is able to offer new insight into the behaviour of alternative gases.

Contents

1

Introduction

Sulfur hexafluoride (SF_6) has long been the standard insulating gas in high-voltage applications due to its excellent properties. However, its extremely high global warming potential [1] (GWP) has led to an urgent search for environmentally friendly alternatives. In recent years, several gas mixtures have been proposed as substitutes for applications in gas-insulated systems (GIS) and gas-insulated lines (GIL). One promising replacement is a fluoronitrile (C4FN)-based gas mixture, which primarily consists of carbon dioxide (CO_2) and oxygen (O_2). As this mixture still contains fluorinated gas, mixtures which are entirely of natural origin such as technical air, nitrogen (N_2) and CO_2 are also being developed as an alternative.

Although the dielectric properties of many alternative gases have been examined under breakdown conditions, their recent introduction means that much remains unknown about their long-term performance and ageing behaviour. This is a concern for TenneT, the Dutch Transmission System Operator (TSO), which plans to commission a GIS substation in Maasbracht that incorporates 21 km of GIL filled with a C4FN-based mixture. To better understand how this mixture performs over time, TenneT has established a PhD position to investigate its long-term behaviour. Partial discharge (PD) activity provides early indications of localised insulation degradation and is strongly related to the generation of decomposition products. As such, PD measurements might serve as a tool to assess the long-term viability of alternative gases. However, to effectively use PD measurements as a diagnostic tool, detailed characterization of discharges arising from insulation defects or gas degradation is essential. Partial discharges occur as extremely fast transients within gas-insulated environments. The limited bandwidth of conventional (IEC60270) measurement setups restricts the amount of information that can be extracted from these signals. To address this limitation and support the PhD research, the primary research objective is formulated as follows:

Primary Research Objective

To enable detailed characterization of partial discharges in alternative gas mixtures by developing a high-bandwidth partial discharge measurement setup.

CO_2 has better arc-quenching capabilities than other natural origin gases. It is commonly mixed with O_2, as the addition not only reduces the production of soot [2], but results in a mixture with improved electric strength [2]–[4]. During development of a 168 kV circuit breaker prototype, [2] found that a gas mixture containing 70% CO_2 and 30% O_2 provided a well-balanced solution.Although CO_2 is being investigated due to its excellent arc-quenching capabilities, the focus of this research is limited to its function as a dielectric insulation medium.
These properties are why CO_2/O_2 mixtures are widely used as carrier gases in C4FN-based mixtures. By investigating the behaviour of CO_2/O_2 separately, the effect of adding C4FN can be isolated.
Although past research has characterised the breakdown strength of this mixture under varying pressure and voltage conditions, studies of its partial discharge behaviour under HV excitation remain

scarce. This makes this mixture an ideal candidate for demonstrating the capabilities of the developed measurement circuit, which leads to the formulation of the secondary research objective:

Secondary Research Objective

To evaluate the partial discharge characteristics of CO_2/O_2 (70%/30%) gas mixture under the influence of varying pressure and electric field strength through experimental evaluation.

1.1. Outline Chapters

Chapter 2 introduces gas-insulated systems, reviews the insulating gases, and explains the physical mechanisms responsible for partial discharge. Chapter 3 reviews the conventional and non-conventional techniques that can be used for PD detection.

Chapter 4 presents the development of the experimental setup. It begins with the design of the high voltage electrode arrangement and the construction of a pressurised test compartment. A conventional measurement circuit based on IEC 60270 is implemented and evaluated first. Based on these findings, an alternative circuit using a high-frequency current transformer (HFCT) is proposed to replace the external coupling capacitor and improve bandwidth and sensitivity.

Chapter 5 describes the measurement setup in detail. Aside from a circuit diagram, a equipment list the transmission parameters of the measurement circuit are shown. Chapter 6 outlines the experimental methodology. In addition to describing the test procedure and acquisition settings used to capture the PDs in the CO_2/O_2 (70%/30%) mixture, the chapter describes three methods applied to estimate the apparent charge.

The results obtained for the mixture are presented in Chapter 7. Chapter 8 starts with an interpretation of the CO_2/O_2 results. The charge estimation methods are discusses, and experiences of experiments are discussed.

Finally, Chapter 9 summarizes the outcomes of the work and proposes future research.

2

Background

2.1. Gas-Insulated Switchgear and Lines

In GIS / GIL systems, HV conductors are enclosed in grounded metallic compartments filled with pressurized insulating gas. As there are more particles present when the gas pressure is increased, free electrons travel a smaller distance during which they gain energy before colliding with another particle. This effect, which is elaborated on in Section 2.3, means that the electric field strength can be increased without having breakdowns when the gas pressure is increased. These systems can have the same voltage level while having a smaller footprint, and are thus used in places where a higher energy density is required than is reached with conventional outdoor air-insulated switchgear (AIS). Examples include densely populated urban environments and offshore platforms. The HV components are mechanically supported by epoxy insulators, often referred to as spacers.

The relevant standards for HV applications are IEC 62271-203 for GIS and IEC 62271-204 for GIL. Defined are requirements for design, ratings, and testing routines.

2.2. Insulation Gases

Insulation gases serve three technical functions [5], namely:

1. **Dielectric Insulation:** The primary function of insulation gases is to act as a dielectric medium, preventing electrical discharge and breakdown throughout the life of the equipment.
2. **Thermal Management:** The insulation gas cools the components in the compartment through convection. The density and heat-temperature coefficient are therefore important gas properties. (current flow generates heat)
3. **(Optional) Arc-Quenching:** In applications such as gas load break switches and gas circuit breakers, the insulation gas may also serve as a medium for current interruption. This arc-quenching function requires specific gas properties suitable for extinguishing electrical arcs

2.2.1. SF_6

The most commonly used insulating gas in GIS is (SF_6). It is preferred due to it being an electronegative gas. Electronegative gases have a high electron affinity [6], which refers to a gas molecule's ability to attract and capture free electrons. In insulating gases, higher electron affinity improves dielectric performance by reducing the number of free electrons that can initiate breakdown (Section 2.3).

Global Warming Potential (GWP)

Although SF_6 has excellent technical performance, it is a Fluorinated greenhouse gas [7]. When gas leaks from pressurised equipment or is handled incorrectly, it remains in the atmosphere for around 850 years [1]. Its 100-year global-warming potential (GWP_{100}) is 22,500 [8], meaning one gram of SF_6 has the same climate impact over a century as 22,5 kg of CO_2 [9].
Because of this, general usage of the gas in the European Union has been restricted. Starting in 2026 [7],

the use in electrical distribution systems will also be phased out, which means that alternative gases are required. Investigated are mixtures entirely of natural origin such as technical air, N_2 and CO_2, and other Fluorinated compounds with lower GWP values. Technical air is a synthetic gas mixture that replicates the atmosphere, containing 79% N_2 and 21% O_2 [10].

Table 2.1: Stand-alone properties of insulation gases relevant to this work. Properties are from [8], except for the GWP of C4-FN. The value of 1450 has been replaced by 2,240, which was found in the datasheet of the manufacturer [11].

Gas	GWP (100 yr)	(Atmospheric) Boiling Point (°C)	Relative Dielectric Strength (SF_6=1)
SF_6	22,500	−64	1.0
C4-FN	2,240	−4.7	~2.0
CO_2	1	−78.5	~0.23
O_2	–	−183	~0.33
N_2	–	−196	~0.38

2.2.2. C4FN

C4-FN (perfluoro-isobutyronitrile) is the most promising fluorinated alternative for SF_6, and when used as a stand-alone gas has roughly double the dielectric strength. For reasons mentioned below it is mixed with natural origin gases. The GWP_{100} of the mixture for example 5% C4-FN, 90% CO_2, and 5% O_2 by volume can be calculate by first converting the volume composition to mass fractions. The molar masses are $M_{\text{C4FN}} = 195.040\,\text{g/mol}$ [11], $M_{CO_2} = 44.01\,\text{g/mol}$, and $M_{O_2} = 15.999\,\text{g/mol}$ [12] and are used to calculate the GWP as such:

$$\begin{aligned}\text{GWP}_{\text{mixture}} &= w_{\text{C4FN}} \cdot \text{GWP}_{\text{C4FN}} + w_{CO_2} \cdot \text{GWP}_{CO_2} + w_{O_2} \cdot \text{GWP}_{O_2} \\ &= 0.1944 \cdot 2240 + 0.7894 \cdot 1 + 0.0159 \cdot 0 \\ &= \boxed{436.2}\end{aligned}$$

For this mixture, this is a reduction of 98% compared to SF_6 which is significant. It is important to note that C4-FN is not only an F-gas but also classified as a PFAS, meaning its availability may be affected by restrictions on production and use [7].

Boiling point

The boiling point of a substance is the temperature at which the gas becomes a liquid. The boiling point of the GIS should be lower than the minimum operating temperature of the GIS, as liquefaction reduces the density of the isolation gas, resulting in a lower electric strength. While SF_6 has an atmospheric boiling point of −64 °C, C4-FN has a boiling point of −4.7 °C [8].

When the pressure is increased, the atmospheric boiling point is even higher, so natural origin gases which have a much lower boiling point (Table 2.1) are added to create a mixture with a lower boiling point. For example, a gas mixture composed of 5% C4-FN, 90% CO_2, and 5% O_2 at a pressure of 0.6$\tilde{\text{M}}$Pa has a boiling point of −27.1 °C [5].

Synergism

Adding CO_2 and O_2 to C4-FN affects more than just the boiling point. Although the overall dielectric strength of the mixture is reduced compared to pure C4-FN, the effect of synergism can result in a dielectric strength that is higher than what would be expected from the individual components of the gas alone [8]. CO_2 is often chosen because it exhibits strong synergistic effects with C4-FN and offers better arc-quenching performance than N_2 [10].

At 0.6 MPa, the 5% C4-FN, 90% CO_2, and 5% O_2 mixture has a dielectric strength of 0.7-0.8 [11] times that of a SF_6 mixture at the same pressure.

2.2.3. CO_2/O_2

An alternative to fluorinated mixtures is the use of fully natural-origin gases, such as CO_2 combined with O_2. Since these gases are non-fluorinated and occur naturally, they are not classified as F-gases or PFAS, and are therefore exempt from the regulatory restrictions that apply to substances like C4-FN [7]. This makes them attractive from both an environmental and long-term availability perspective, at a cost

Table 2.2: Gas properties of SF_6 and C4-FN mixture at 0.6 MPa

Gas Mixture	Ratios	GWP (100 yr)	Boiling Point (°C)	Rel. Dielectric Strength (SF_6=1)
SF_6	100%	22,500	−20 [5]	1.0
C4-FN/CO_2/O_2	5%/90%/5%	436	−27.1	0.7-0.8

in dielectric strength.

Similar to the synergistic effects observed in C4-FN mixtures, CO_2 also exhibits synergism with O_2, leading to better insulation properties than would be expected from the individual components alone. This is because of the electron affinity of O_2 [13].

By-product generation


Pure CO_2 (Dark-brownish)
CO_2/O_2(30%) (Whitish)

Figure 2.1: Solid by-products after arcing in pure CO2 gas and CO2/O2 gas mixture after 1,900 kJ accumulative interruptions [2]

When ionization occurs within the insulating gas, stable gas molecules are turned into charged reactive components. These components can recombine into other molecules than the original gas mixtures. These can be gaseous by-products with poor insulation performance or corrosive properties [14], or solid such as conductive free Carbon [2], also known as soot. Over time, this gas degradation can reduce dielectric performance and shorten the lifetime of the equipment.

In both the C4-FN/CO_2/O_2 and CO_2/O_2 mixtures, the presence of O_2 plays a role in reducing the formation of unwanted byproducts [2], [14]. Figure 2.1, shows the change in byproduct generation reduction after arcing in pure CO2 gas and CO2/O2 gas mixture.

Since PD measurements inherently generate byproducts, the gas composition will gradually change over time. This should be considered when determining experiment durations and selecting the volume of the test compartment.

2.2.4. Experimental evaluation of alternative gases

To perform experimental evaluation on alternative gases, CIGRE working group D1.67 has developed TB849 " Electric performance of new non-SF6 gases and gas mixtures for gas-insulated systems". The technical brochure proposes a set of tests that include procedures to evaluate the electric performance of these gases in a consistent manner. Among these, a recommended protocol is provided to ensure consistent and reproducible gas handling during testing. The steps [5] are as follows:

1. **Evacuation:** Evacuate the test vessel for 30 minutes. If the vessel has not been used for a long time or if humidity ingress is suspected, a longer evacuation period is recommended to minimize residual moisture.
2. **Nitrogen Flush:** Flush the vessel with 1 bar of dry nitrogen to remove remaining contaminants.
3. **Second Evacuation:** Evacuate the vessel again to ensure purity before gas filling.
4. **Gas Filling:** Fill the vessel with the desired gas mixture. Begin with the component that has the smallest partial pressure.
5. **Homogenization:** If the gas was not pre-mixed, ensure homogeneity in the vessel. Recommended methods include:
   - Operating an internal fan for 30 minutes, or
   - Allowing the gas to settle for 36 hours (recommended for larger vessels or those with challenging aspect ratios).

2.3. Discharges in non-uniform fields

When a free starting electron appears in the gas mixture, they are accelerated by the electric field until they hit a gas molecule. The larger the distance the electron can travel, the more it is accelerated, and the larger the impact. The average length a free electron can travel is known as the mean free path λ_m.

$$W = e \cdot E \cdot \lambda_m \tag{2.1}$$

where:

W is the energy gained by an electron between collisions [J]
e is the elementary charge [1.602×10^{-19} C]
E is the electric field strength [V/m]
λ_m is the mean free path of the electron [m]

If the energy of the electron when it collides with a neutral molecule is sufficient, ionisation occurs. The molecule loses an electron and becomes positively charged. There are now two free electrons, each accelerated by the electric field until they collide with gas molecules, continuing the process and forming an chain reaction. This process is known as a Townsend avalanche.

For gases with a high electron affinity (electronegative gases), another interaction can occur, which is attachment to the molecule to form a negatively charged molecule. This limits the generation of the electron avalanche, and the resulting number of effective ionising collisions per unit length is known as the effective ionisation coefficient α_{eff}. Avalanche growth is only possible when $\alpha_{\text{eff}} > 0$.

$$\alpha_{\text{eff}}(m^{-1}) = \alpha - \eta \tag{2.2}$$

where:

α is the number of the ionizing collisions per unit length
η is the electron attachment coefficient

The higher the gas molecule density N in (m^{-3}), lower the mean free path, which is why increasing the pressure increases the electric strength. To compare gas behaviour under different conditions the reduced electric field is often used, which is E/N. The unit that is often used for display is Townsend (Td), which is equivalent to 10^{-21} V·m^2 The reduced effective ionisation coefficient is $\left(\frac{\alpha}{N}\right)_{\text{eff}}$, and is a function of the reduced electric field.

$$\left(\frac{\alpha}{N}\right)_{\text{eff}} = f\left(\frac{E}{N}\right) \tag{2.3}$$

Figure 2.2 shows the effect of adding O_2 to CO_2 has on the $\left(\frac{\alpha}{N}\right)_{\text{eff}}$. When O_2 is added, the required reduced electric field before $\left(\frac{\alpha}{N}\right)_{\text{eff}} = 0$, also known as $\left(\frac{E}{N}\right)_{\text{crit}}$ increases. The mixture consisting only of O_2 has a lower $\left(\frac{E}{N}\right)_{\text{crit}}$, which shows the effect of synergism. Two types of breakdown can occur within gases. If the Townsend avalanche can keep growing towards the anode, feedback electrons are created

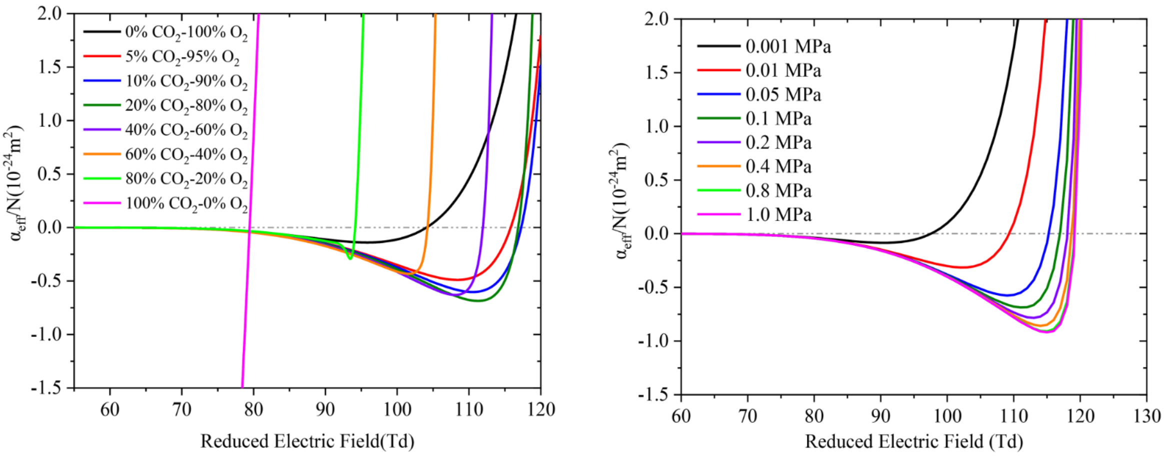

FIG. 9. α_{eff}/N of different CO_2–O_2 mixtures at 0.1 MPa.

FIG. 10. α_{eff}/N of a 20% CO_2–80% O_2 mixture at different pressures.

Figure 2.2: α_{eff}/N of different CO_2–O_2 mixtures at 0.1 MPa and α_{eff}/N of a 20% CO_2–80% O_2 mixture at different pressures which show the effect of adding a gas with a high electron affinity (O_2). Figure 9 and 10 from [15].

which create more avalanches resulting in breakdown. The other type of breakdown is the streamer breakdown. Immobile positively charged ions lag behind the fast electrons, which results in a space charge distribution that creates an electric field. As the electron avalanche, grows to 10^6 to 10^8 electrons [6], the electric field becomes such that extra ionisation occurs. The photons produced by this ionisation hit gas molecules to create a feedback effect.

Non-uniform Field

The electric field distribution is dependent on the electrode geometry. A key parameter to describe the field distribution is the *field utilization factor* η, defined as:

$$\eta = \frac{E_{\text{mean}}}{E_{\text{max}}} = \frac{V}{d \cdot E_{\text{max}}} \tag{2.4}$$

where:

$E_{\text{mean}} = V/d$ is the average electric field across the electrode gap of distance d
E_{max} is the maximum local field strength

In a perfectly uniform field, such as between two large parallel plates, $\eta = 1$. For point-plane or rod-plane geometries, the field is concentrated near the tip, reducing η. These non-uniform fields are split at the critical value η_c. Field distributions $> \eta_c$ are weakly non-uniform, and if the requirements for the Townsend or streamer breakdown are met breakdown occurs immediately. For an air mixture under standard conditions, the critical value $\eta_c \approx 0.2$.

For strongly non-uniform ($\eta < \eta_c$) fields, it is possible to have discharges without having breakdown at a lower. As the avalanche moves away from the region where the field is high, α_{eff}/N is reduced until it becomes 0 and the avalanche stops growing. In Figure 2.3 the voltage relating to this partial discharge can be seen, which is lower than the breakdown voltage. The discharge behaviour in a strongly non-uniform field can change significantly with increasing pressure [6].

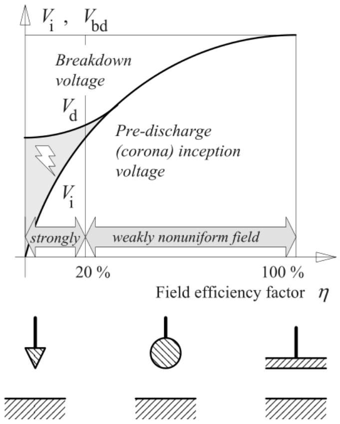

Figure 2.3: Pre-discharge (corona) inception and breakdown voltage in strongly and weakly non-uniform fields at constant electrode distances. Figure 3.2-24 from [6]

2.4. Partial Discharge: Corona Discharge

A partial discharge is defined in [17] as a "localized electrical discharge that only partially bridges the insulation between conductors and which can or can not occur adjacent to a conductor". If ideally measured, the partial discharge is unipolar and non-oscillatory [18]. The partial discharge type investigated in this thesis is the HV side corona discharge, for which the non-uniform geometry shown in Figure 2.3 is on the side of the HV supply. A picture showing corona discharges on the HV side can be seen in Figure 2.4.

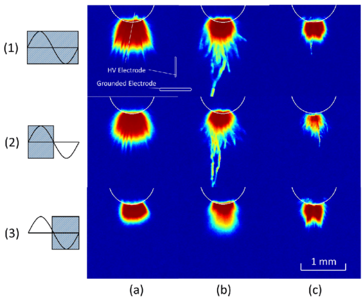

Figure 2.4: Positive and Negative corona discharge (HV side) in SF6 [16]

2.4.1. Effects of PD

When a PD occurs, a multiple of physical effects occur. These are as follows: [19]

- An electrical current flows.
- This electrical current will stimulate electromagnetic (EM) radiation.
- The flow of electrons and ions in the discharge will also heat the surrounding gas or liquid, giving rise to a pressure wave (sound).
- When the excited atoms that occur in a discharge return to their ground state, photons are emitted

2.4.2. Frequency Spectrum

As a result of the high pressure environment and the properties of the gases the risetimes of the PDs can be extremely fast. For SF_6, a risetime of 24 ps was measured which was still limited by the bandwidth of the measurement circuit [20]. Table 2.3 shows the risetimes for dry air and CO_2. While dry air has a large difference for positive and negative PD pulses, CO_2 does not have this effect. The higher the pressure, the shorter the pulse risetime. These short risetimes transforms into a frequency domain signal in the UHF region (300 MHz to 3,000 MHz) [19]. spectrum.

Table 2.3: Rise time of PD current pulses [21]

Gas	**Rise time (PD current pulse)**	
Dry air	0.4 – 2 ns	(Negative pulse)
	3 – 12 ns	(Positive pulse)
CO_2	0.7 – 4 ns	(Negative pulse)
	0.6 – 4 ns	(Positive pulse)

3

PD Detection (in GIS)

This chapter describes the function of PD detection in GIS systems, as well as the methods that can be used to detect which are based on the physical phenomena of the PDs. PD events in GIS occur as fast phenomena due to the pressurised environments.

GIS systems are made of a combination of several individual sections, which can be modelled as capacitive devices. As a result the assembled bays or lines have a large capacitance, which can cause issues when performing tests on the fully completed systems [19]. Equipment can be tested either during normal operation, known as an online test, or with a voltage being supplied as part of the experimental setup, referred to as an offline test.

3.1. Purpose of Partial Discharge Detection

PD detection can serve as a diagnostic tool for GIS, offering early insight into insulation degradation and potential failure mechanisms. The discharge magnitude is strongly correlated with the amount of decomposition, which results in degradation of the gas [14].

Figure 3.1 shows typical defects in GIS which result in PDs. The fixed protrusion on the HV side is the fault that will be investigated.

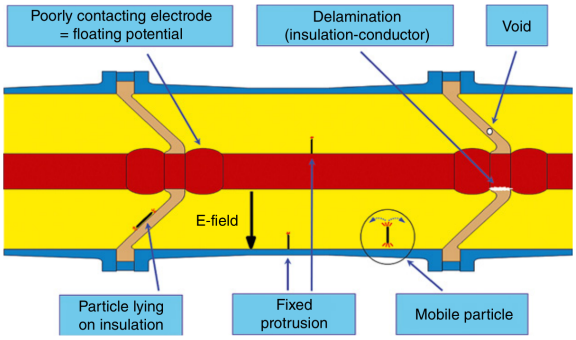

Figure 3.1: Diagram showing typical PD defects in GIS [19]

3.2. Overview Detection Methods

Based on the physical phenomenon described in Section 2.4.1, several detection techniques have been developed. The charge-based method is standardised in IEC 60270 [22] as is known as the conventional method. Non-conventional methods are UHF detection, acoustic, and optical detection. IEC 62478 [23] does not provide standardisation, but instead contains recommendations on these methods. While chemical detection cannot directly identify partial discharges, it is listed as it has the ability to provide insights into the long-term impact of PDs on gas quality.

Table 3.1: Overview of PD Detection Methods in GIS

Detection Method	Physical Phenomenon Detected	Type of Sensor Used
Conventional (IEC 60270)	Charge-Based (electrical)	Quadripole/Resistor
HFCT	Charge-Based (electrical)	HFCT (bandwidth up to 500 MHz)
UHF Detection	EM radiation (electrical)	UHF antenna or capacitive sensor
Acoustic Detection	Acoustic pressure waves	Piezoelectric acoustic sensor
Optical Detection	Light emissions (UV/visible)	Photomultiplier tubes / UV sensors
Chemical Detection	Byproducts	Gas sensors

3.2.1. Partial Discharge Inception Voltage (PDIV)

PDIV is the voltage at which discharges can occur, which was already mentioned in Section 2.3. In IEC 60270, the PDIV is defined as the voltage at which repetitive partial discharges are first observed in the test object [17].

Figure 3.2 shows the breakdown, positive and negative inception voltages of a CO_2/O_2 (87.23%/12.77%) mixture at various pressures. The η of the configuration used is 3.85%. It can be seen that the negative PDIV increases linearly with pressure.

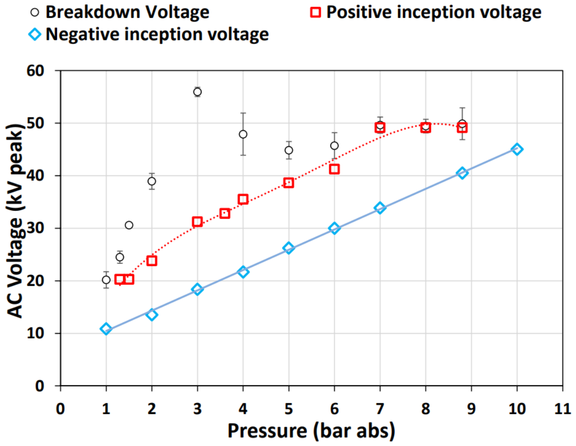

Figure 3.2: Breakdown, positive and negative inception voltages as a function of gas pressure for a CO_2/O_2 (87.23%/12.77%) mixture. Figure 9 from [4]

3.3. Measurable Quantities

The following quantities are commonly measured in PD experiments and serve as key indicators to characterise discharge behaviour. These parameters provide insight into the severity and type of the discharges.

- Partial Discharge Inception Voltage (PDIV)
- Partial Discharge Extinction Voltage (PDEV)
- Apparent charge magnitude q_i occurring at time instant t_i. When an AC voltage is applied, the phase angle ϕ_i or the location of the PD on the AC cycle provides more information.
- Discharge polarity (positive or negative)
- Pulse count rate / repetition rate (pulses per cycle, PPC)
- Pulse rise time and fall time
- Pulse duration or width
- Frequency spectrum of the PD signal

The sensitivity of a detection circuit is defined in [24] as "as the smallest discharge impulse, measured in pC, that can just be distinguished from background noise". The better the sensitivity, the smaller the discharges that the measurement circuit can detect.

3.4. Charge-Based Detection

Charge-Based detection is based on detection of the current produced during a discharge event, usually through a measurement impedance which is connected to the terminal of the device under test.

3.4.1. Electrical Detection Model: ABC

The source of this current can be described through the ABC model, in which the equipment under test C_{EUT} is represented through three capacitances. The test object is assumed to be primarily capacitive, as in that case the inductive HV source can be simplified to be an open circuit for the fast PD event. The three capacitances by which the circuit as seen in Figure 3.3a are formed are[19]:

- C_a is the capacitance representing the entire insulation, except the part that is in series with the defect
- C_b is the capacitance of the insulation in series with the defect
- C_c is the capacitance of the defect

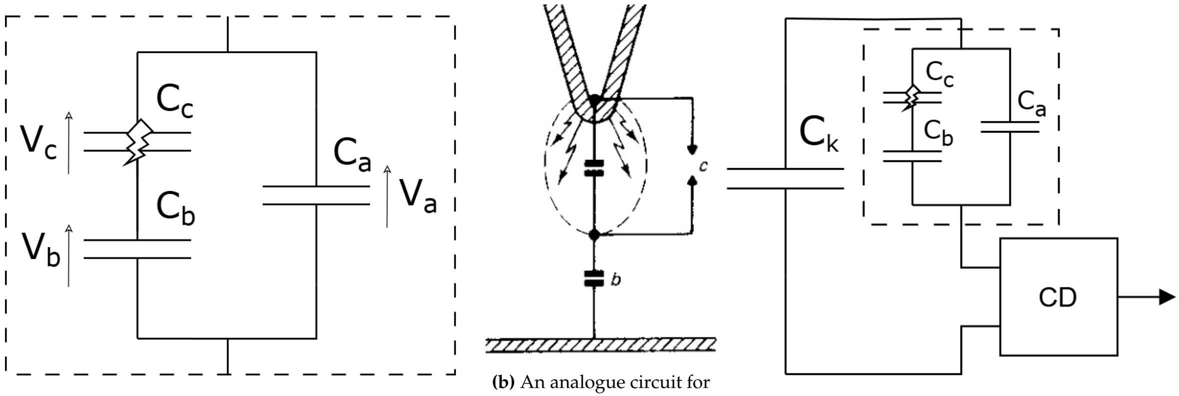

(a) Model to represent DUT

(b) An analogue circuit for corona discharges [25]

(c) Including Coupling Capacitance and Device

Figure 3.3: ABC Model

As C_c depends on the location, size and type of PD its value is unknown. In general, it can however be assumed that $C_b << C_c << C_a$. In the model, the occurrence of a PD results in C_c being being discharged. V_c drops to zero and the charge of the PD is $q_{PD} = \Delta V_c \cdot C_c$. As a result there is a voltage imbalance ΔV_c between C_a and C_b, which is restored through a charge transfer from C_a. This charge transfer can be measured and is what is called the apparent charge q_{app} (Equation 3.1).

$$\begin{aligned} \Delta V_a &= \Delta V_c \cdot \frac{C_b}{C_a + C_b} \\ q_a = \Delta V_a \cdot C_a &= \Delta V_c \cdot \frac{C_b \cdot C_a}{C_b + C_a} \approx \Delta V_c \cdot C_b \end{aligned} \tag{3.1}$$

Instead of measuring q_{PD} directly, a smaller (Equation 3.2) induced charge is what can be detected.

$$q_{app} = C_B \cdot \Delta V_C < C_C \cdot \Delta V_C = q_{PD} \tag{3.2}$$

Detection requires a measurement impedance, which is an issue since this effect takes place within the test object. By placing a capacitor (C_k) over the test object, an alternative current path in which a measurement impedance can be placed is created. The sensitivity of this detection circuit seen in Figure 3.3c depends on the ratio between C_k and C_{EUT} according to Equation 3.3.

$$q_k = \frac{1}{1 + (C_k / C_{EUT})^{-1}} q_{app} \tag{3.3}$$

3.4.2. Conventional IEC 60270

IEC 60270 is the internationally recognised standard for charge-based partial discharge measurements. It defines test circuits, calibration procedures, and system requirements to ensure consistency and comparability across tests. All test circuits are based on the concept of the coupling capacitor mentioned in Section 3.4.1, with variations based on the goal that "the current pulses resulting from partial discharges have magnitudes and shapes that are most favourable for detection" [22].
Two test circuits can be seen in Figure 3.4. Figure 3.4a shows the circuit with the measurement impedance under the coupling capacitor, which is known as an indirecht measurement circuit. These circuits measure the PD signal with inversed polarity compared to when the measurement impedance would be located directly under the test device. Figure 3.4b shows one of the alternative circuits, in which the bushing is used as a coupling capacitor and the bushing tap is used to connect a measurement impedance.

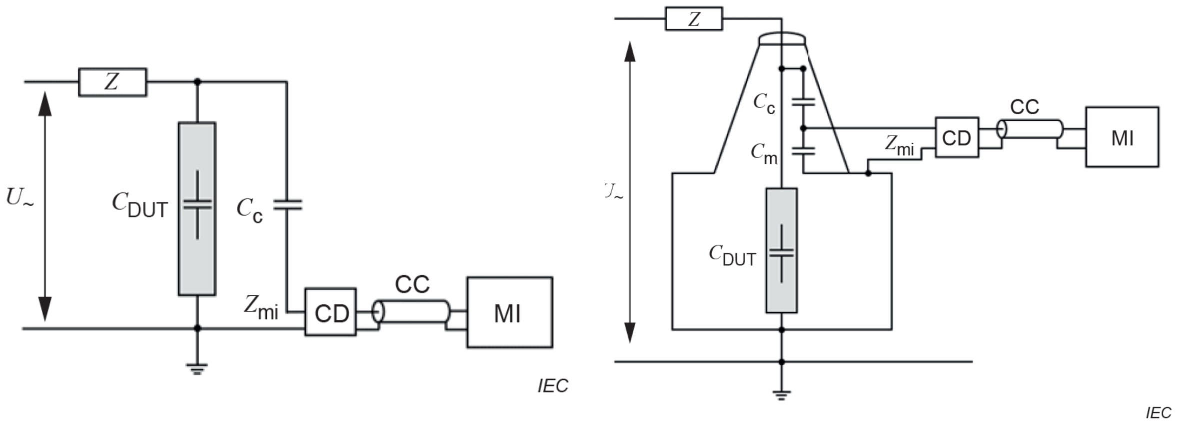

(a) Coupling device in series with coupling capacitor[22] which is an indirect measurement circuit

(b) Test circuit for measurement at a bushing tap[22]

Figure 3.4: Two test circuits described by IEC 60270

To quantify partial discharges, IEC 60270 uses a method called quasi-integration which is based on analog bandpass filtering. The frequency response is designed such that the output signal is proportional to the apparent charge. A more detailed explanation on the theory behind the method can be found in Section 6.2.2. IEC 60270 describes a Wideband and a Narrowband system. The Wideband filter has a lower limit frequency between 30 and 100 kHz, and a minimum bandwidth of 100kHz. The bandwidth of the narrowband system should be between 9 and 30 kHz and its mid-band frequency can be located between 100 and 1000 kHz. If there a lot of interference, this system can be deployed to evaluate a bandwidth where the noise is not present.

Quadripole

The most common type of coupling device is the Quadripole[17], which converts the the input current into two voltage signals, one for the PD signal and one for AC synchronization. In Figure 3.5 the schematic of a passive version of a quadripole can be seen. Included is a measurement resistor R_M, which in combination with C_k acts as a high-pass filter (Equation 3.4).

$$f_0 = \frac{1}{2\pi R_M C_k} \tag{3.4}$$

The capacitor C_m on the parallel path creates a capacitive voltage divider with C_k, which provides the synchronisation signal. The inductor L_m is chosen so that the components of the PD pulse flow through the branch, while not blocking the AC signal.

Calibration

Calibration devices mimic the PD by injecting a pulse with a known charge over the terminals of the test device while no voltage is applied. If the injected signal represents the apparent charge pulse of a PD

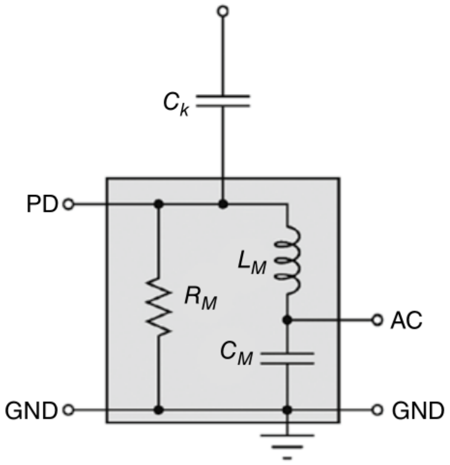

Figure 3.5: Passive quadripole device, from [19]

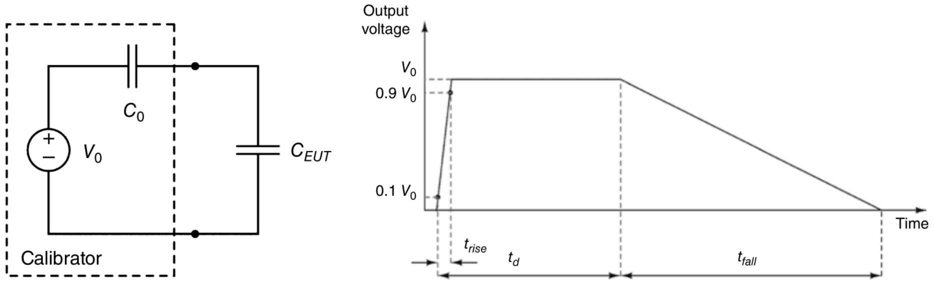

Figure 3.6: Figure 31 and 32 from [19], showing the calibrator structure and an ideal calibrator pulse

accurately, the processed output of the measurement circuit is similar to that of a real PD. By comparing the output voltage to the known charge, a calibration constant $k = Q_{\text{cal}}/V_{\text{cal}}$ can be determined. During the high voltage test, the apparent charge can now directly be evaluated by multiplying the readings with the constant. Calibration of the complete test arrangement can be done without having a voltage applied to the system.
Important requirements to ensure validity of the calibration procedure are [17]:

- Only if the test object is capacitive in nature can the calibration procedure be used.
- To assure accuracy at magnitude of the PDs the calibration factor should be based on a calibration charge which should be within 50% to 200% of the PD magnitude.
- If any component within the circuit, or any setting of the measurement setup is changed, the calibration procedure should be repeated.

Calibration Devices

Figure 3.6 shows the structure of a calibration device and its ideal signal output. to ensure complete charge transfer (>95%) by the calibrator to the test object, IEC 60270 contains another requirement. C_0, the internal capacitance of the calibrator must be $C_0 < 0,1 \cdot C_{EUT}$ If this requirement is met, the calibration pulse is equivalent to a PD pulse with charge magnitude $Q = V_0 \cdot C_0$.

The requirements the calibrator pulse in Figure 3.6 must adhere to are defined in IEC 60270 and are as follows: [26]

- **Rise time:** $t_r \leq 60$ ns
- **Time to steady state:** $t_s \leq 200$ ns

- **Step voltage duration and decay time:** $t_d \geq 5\ \mu\text{s}$
- **Deviation of the step voltage U_0 between t_s and t_d:** $\Delta U \leq 0.03\, U_0$
- **Fall time (time interval until voltage reaches $0.1\, U_0$):** $t_{\text{fall}} \geq 100\ \mu\text{s}$

3.4.3. High-Frequency Current Transformer

High-Frequency Current Transformers (HFCTs) are a type of measurement impedance which can be used for non-intrusive partial discharge detection. These sensors operate based on inductive coupling and are placed around a conductor to capture high-frequency components of the discharge current. HFCTs offer a broad detection bandwidth of up to 500 MHz, but do not capture lower frequency components [27]. Capturing the PD waveforms allows for new charge estimation methods [28] instead of quasi-integration method proposed by IEC 60270. Important to keep in mind when performing charge estimation methods, is that when frequencies extend into the HF-UHF range, not all test objects can be represented as a lumped capacitance which invalidates the calibration method [29].

Figure 3.7 shows an ideal model of a HFCT and its equivalent representation as a measurement impedance. The transfer impedance, in dBΩ can be derived as follows:

$$\frac{I_s}{I_p} = \frac{N_p = 1}{N_s} \quad \text{and} \quad I_s = \frac{V_s}{50\Omega} \tag{3.5}$$

$$I_p = \frac{\frac{V_S}{50\Omega}}{N_s} = \frac{V_s}{Z_t} \tag{3.6}$$

$$TI(dB) = 20 \cdot \log_{10} Z_T \tag{3.7}$$

$$I(\text{dBA}) = V(\text{dBV}) - TI(\text{dB}\Omega) \tag{3.8}$$

Based on the transfer impedance and the measured voltage, the current that is flowing through the main conductor can be derived. Increasing the number of turns in the secondary winding of an HFCT can raise the output signal amplitude. However, this also increases inter-turn capacitance and self-inductance, which lowers the upper cut-off frequency and limits the sensor's bandwidth [19]. This means that the sensor design is a trade-off between bandwidth and sensitivity.

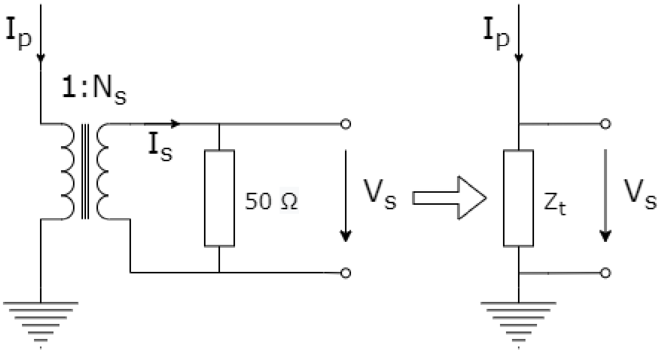

Figure 3.7: Ideal HFCT with a 50Ω Load Impedance and the Transferred Impedance equivalent

3.5. Electromagnetic Detection (UHF)

In UHF-based PD detection, the GIS enclosure can be seen as a coaxial waveguide [19]. This makes sense because GIS has a central high-voltage conductor surrounded by a grounded metal enclosure. PD events in pressurised gases happen very quickly and produce signals with frequency components in the hundreds of MHz up to the GHz range.

Detection is done with UHF sensors, such as capacitive sensors. Since the sensor measures the wave that travels through the GIS and not the discharge itself, it is difficult to directly relate the signal to the size of the discharge in pC. A sensitivity check according to IEC61934[30] can be performed to estimate the magnitude. UHF detection can thus be used to check if PD is present, to estimate its location, and to analyse its pattern. It works especially well for online monitoring, where it offers good noise immunity as high frequency noise decays quickly. The grounded housing additionally has a shielding effect on the sensors.

3.6. Optical, Acoustic and Chemical Detection

In addition to electrical and electromagnetic signals, partial discharges can also be detected by the light, sound, or chemical by-products they produce. Optical sensors detect light from ionization, which depends on the gas type and recombination process. Since GIS is fully enclosed, the sensor must be placed inside but is then immune to interference. Acoustic sensors detect sound waves from PD and can be used to locate the source of discharges. Chemical detection involves sampling gases to identify PD by-products. This method is invasive and slow but can help assess long-term gas degradation.

3.7. Summary

Each detection method has specific advantages and limitations, so a thorough evaluation is needed to select the one most appropriate for a given application.

The methods described in IEC 60270, while older and with known limitations, are still widely referred to as the "conventional method" due to their standardised procedures and user-friendly calibration. The usage of a HFCT as a measurement impedance can provide new methods to estimate the apparent charge. Non-conventional methods offer alternative capabilities. UHF detection is well suited for online monitoring because of its high immunity to noise and adaptability across longer GIS lengths by using multiple sensors. Acoustic detection can be used for locating defects. Optical methods, while requiring line-of-sight, can provide useful information on discharge by-products through spectral analysis. This can be particularly beneficial for evaluating the condition of alternative gas mixtures, which are still relatively new and not extensively tested. Chemical detection, though slower and invasive, can reveal long-term changes in gas composition.

3.8. Noise & Interference

Noise and interference are unwanted signals that can distort partial discharge measurements, but they differ in origin. Noise refers to random background signals generated by thermal motion or electronic components. One common type is Johnson-Nyquist noise, which is thermal noise generated in resistive components and is described as follows:

$$V_n = \sqrt{4k_\mathrm{b}TR\Delta f} \tag{3.9}$$

Noise is always present and must be taken into account when integrating signals to estimate discharge charge [31], as this can result in an overestimation of the value. As mentioned in the UHF section, high frequency components decay faster. As a result electromagnetic noise energy is concentrated below several MHz [23]. As a result PD detection systems that operate above this range often achieve a better signal-to-noise ratio. PD sources are typically closer to the sensor than distant noise sources, so higher frequency components from PD tend to dominate. Interference refers to disturbances from other active sources that can imitate or overpower PD signals. These include:

- Conducted interference via grounding or power systems, such as:
  - Common impedance coupling: Shared paths for current lead to voltage offsets.
  - Ground loops: Multiple grounding paths form loops where magnetic fields induce current.

  These effects can be reduced by using single-point grounding with thick conductors [19].
- Radiated electromagnetic interference (EMI) or radio frequency interference (RFI) from nearby equipment [17].
- PD activity from equipment that is not being tested, such as the transformer.

Offline tests offer better control of environmental and voltage conditions, making interference suppression more effective [19]. EM interference can be blocked by performing the test in a Faraday cage. By performing the test in a measurement Performing the test in a Faraday cage shields the measurement from electromagnetic noise. By characterising the measured PDs some sources of interference can

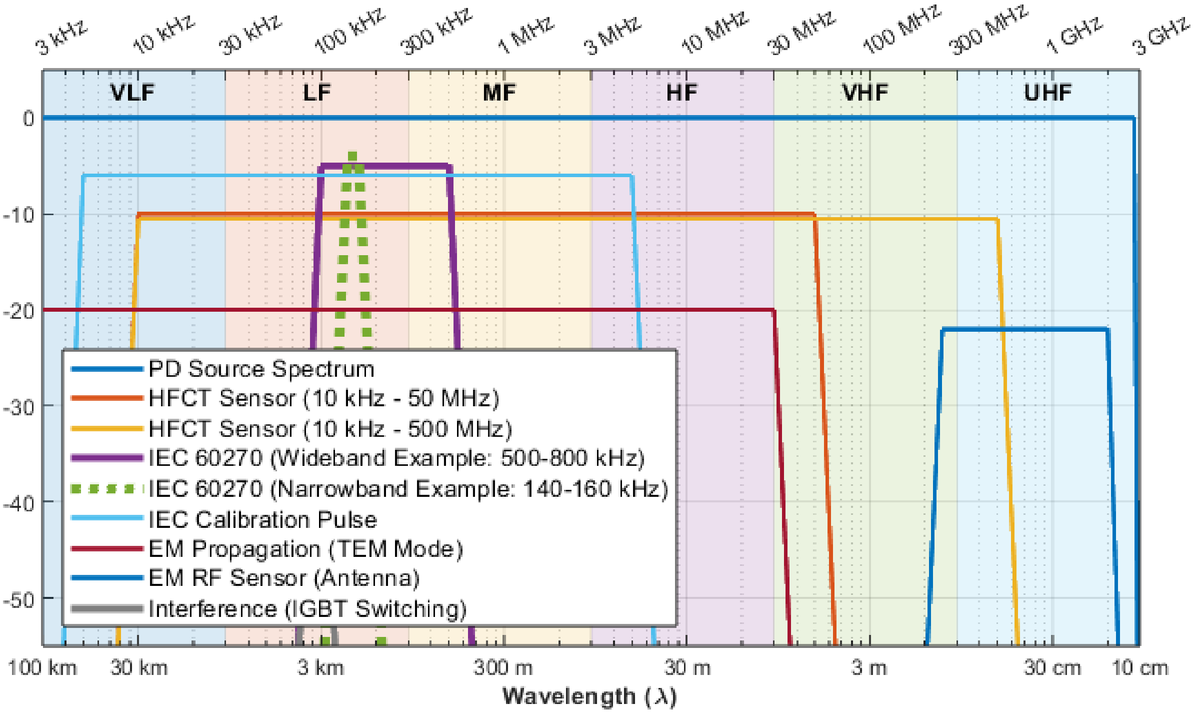

Figure 3.8: Overview of frequency spectrum relevant for PD detection

be easily be distinguished from the actual PDs, for example through their phase in the AC cycle or magnitude.

3.9. Frequency Spectrum

Figure 3.8 shows an overview of the frequency spectrum relevant for PD detection. The frequency definitions are based on those found in [23].

4

Development of experimental setup

This chapter describes the development of an experimental setup used to evaluate PD behaviour in alternative insulation gases under AC voltages. The type of defect that will be simulated is that of a protrusion on the HV side of the system, which will generate HV side corona discharges. Section 4.1 describes the electrode configuration developed to generate the required non-uniform electric field distribution. The results of the COMSOL model developed to evaluate the impact of electrode dimensions on the field utilization factor is also discussed. Section 4.2 describes the test compartment required to contain and handle the gas. The bushing, which is required to apply a voltage to the electrode configuration inside the pressurized compartment is also discussed in this section.

For Section 4.3 a measurement circuit which makes use of an external coupling capacitor was setup, and its limitations regarding bandwidth resulting from the dimensions of the physical current loop are discussed.

In Section 4.4 the inherent capacitance of the bushing is evaluated by adapting the COMSOL model. After this realisation, this capacitance is used to create a measurement circuit in Section 4.5 that uses this inherent capacitance as a coupling capacitor. The modifications to the circuit required for these changes and further improvements are discussed in this section as well.

4.1. Electrode Arrangement

The type of defect that will be simulated is that of a protrusion on the HV side of the system, which will generate HV side corona discharges. To generate this non-uniform electric field a needle-plane configuration is used. The electrode configuration is based on Test 9: "PD activity in strongly non-uniform arrangement" of the CIGRE Technical Brochure 849 [5]. Adherence to these test parameters should allow for comparison with results found in the literature for other gas mixtures. The geometry of this arrangement can be seen in Figure 4.1a, and the dimensions can be found in Table 4.1. The field utilization factor (η) of the configuration is provided, and is 5.6%.

On the HV side, a needle is connected to a rod extending from the bushing. The needle has a small tip radius of 0.125 mm and is made of tungsten to prevent degradation of the surface material when discharges occur. To ensure all discharges occur at the needle tip, the needle extends out of a smoothing sphere with a radius of 20 mm. This sphere suppressing field enhancement in any other part than near the needle tip. This way material finish or non rounded corners do not result in the generation of PDs. The ground electrode, which is distanced 15 mm from the needle tip is a plane electrode with rounded corners. The electrode with while the grounded electrode is a flat plane with a diameter of 200 mm. Figure 4.1b shows the electrode arrangement including the distance reference, which is a brass cylinder with a length of 15 mm used to ensure correct gap distance. The plane is electrically grounded through the physical connection to the compartment housing. Figure 4.13 shows the entire electrode arrangement including the connecting material.

As can be seen in Table 4.1, the tip radius and plane electrode diameter differ from the suggested configuration. To evaluate the impact of these differences on the η, the electric field was simulated using a FEM model for varying geometric parameters.

Table 4.1: Geometrical parameters of electrode setup

Parameter	Value TB849 HV Strongly non-uniform (mm)	Value Test Setup (mm)
Needle tip radius	0.2	0.125
Needle protrusion length from sphere	3	3
Smoothing sphere diameter	40	40
Plane electrode diameter	140	200
Gap distance (needle tip to plane)	15 (±1%)	15

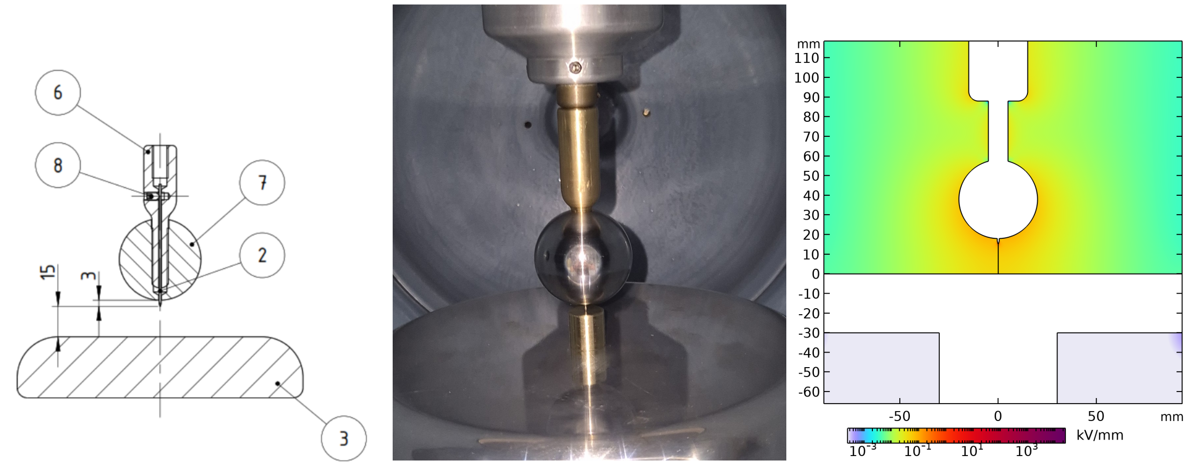

(a) Electrode geometry as recommended by CIGRE TB849, adapted from Figure 5-12 in [5]

(b) Photograph of the implemented arrangement with the 15 mm Distance cylinder present, used as a gap distance reference

(c) Simulated electric field distribution (using COMSOL) of the test setup for a needle tip radius of 0.125 mm after applying 1 kV

Figure 4.1: Comparison of the reference (TB849) and implemented electrode configuration, including the simulated electric field distribution of the needle-plane arrangement in the test setup.

4.1.1. Electric Field Strength

Table 4.2: Parametric Sweep Settings

Parameter Name	Parameter Value List	Parameter Unit
tip_radius	0.05, 0.1, 0.125, 0.15, 0.2, 0.25, 0.3	mm
smoothing_sphere_enable	0, 1	–

By evaluating the electric field maximum after applying 1 kV, η is calculated as follows:

$$\eta = \frac{E_{\text{mean}}}{E_{\text{max}}} = \frac{V}{dE_{\text{max}}} = \frac{1kV}{15mm \cdot E_{\text{max}}} \tag{4.1}$$

Figure 4.2 shows the η for different values of tip radius found through simulation. The left y-axis shows the E_{max} values (solid lines) from which the η values are calculated. Included are the results of the simulation performed with and without the smoothing sphere. The η corresponding to the geometry in the setup and of the TB849 are marked. The η of the TB849 geometry of 5.6% matches the number provided by the standard. The field distribution of the implemented geometry is even more non-uniform, with η = 4.0%

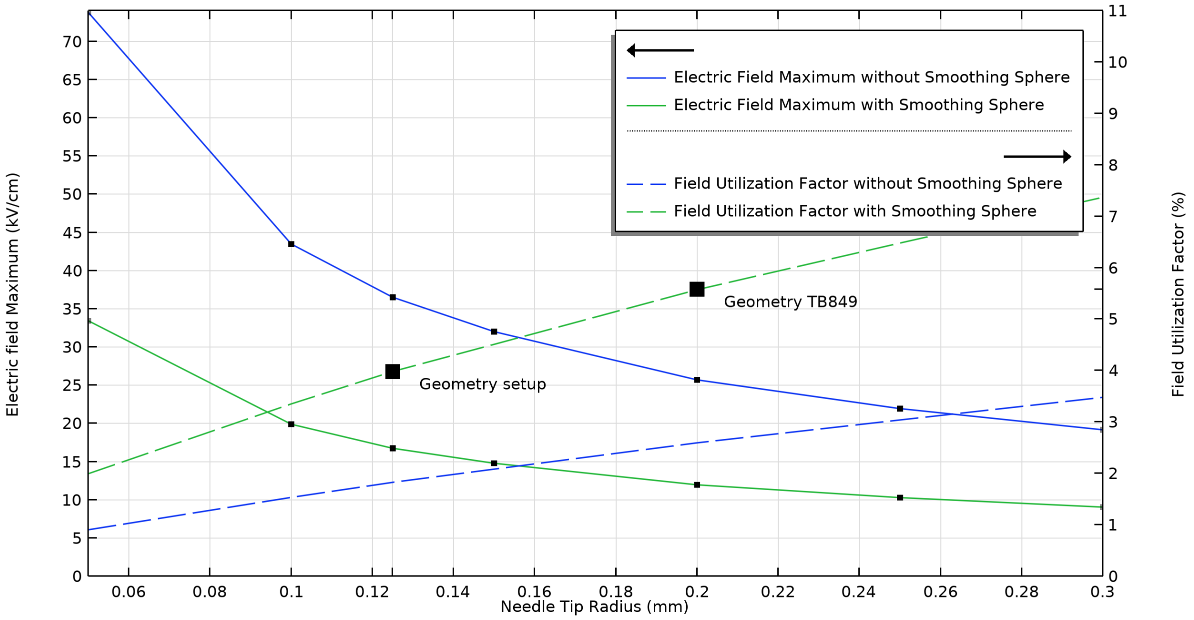

Figure 4.2: E_{max} for $V_{\text{applied}} = 1kV$ and corresponding field utilization for different needle tip radiuses

4.2. Test Compartment

A gas tight compartment is required to contain the gas. A refurbished GIS was adapted by the lab technician into a test compartment to be used in experiments. To connect the HV source to the electrode configuration a bushing is required. This bushing, which can be seen before and after installation in Figure 4.3 is further discussed in the next section.
The compartment is placed on a base physically connected through isolators. The raised compartment allows for easy operation, and the isolators make it possible to control the ground path. The isolated base, including the components related to gas handling can be seen in Figure 4.3c.

As the the core aluminium structure is refurbished detailed documentation is not available. The gas volume is approximately 112 litres which is based on the following assumptions.

$$\begin{aligned}
\text{Cylinder part:} \quad & r = 0.15\,\text{m}, \quad h = 0.5\,\text{m} \\
& V_{\text{cyl}} = \pi r^2 h = \pi \cdot (0.15)^2 \cdot 0.5 \approx 0.035\,\text{m}^3 \\
\text{After 30\% reduction (bushing):} \quad & V_{\text{cyl,adj}} = 0.035 \cdot 0.7 = 0.0245\,\text{m}^3 \\
\text{Bottom tank (core part):} \quad & V_{\text{tank}} = 0.5 \cdot 0.5 \cdot 0.35 = 0.0875\,\text{m}^3 \\
\text{Total volume:} \quad & V_{\text{total}} = V_{\text{cyl,adj}} + V_{\text{tank}} = 0.0245 + 0.0875 = 0.112\,\text{m}^3
\end{aligned}$$

4.2.1. Bushing

To connect the electrode to HV, a Resin Impregnated Paper (RIP) Condenser Bushing is mounted at the top of the compartment. The bushing is rated for a nominal voltage of 145 kV and a continuous current of 400 A. Figure 4.3a shows a picture of the bushing before installation onto the compartment. As a capacitive-graded bushing, the central conductor is insulated from the grounded enclosure through a series of floating conductors which homogenise the field distribution. In Figure 4.4 the construction of such a bushing can be seen. Capacitance C1 represents the combined capacitance between the central conductor and the last of the floating conductors. C2 represents the capacitance from the last floating layer to the grounded flange. Connected to the last layer is a test tap that is grounded during normal operation, short-circuiting C2 so that only C1 remains. [32] The bushings nameplate provides values $C_1 = 270$ pF and $C_3 = 231$ pF, the latter likely referring to the combined series capacitance of C1 and C2. Thus, C2 can be derived according to Equation 4.2.1, which seems to be in line with the expectation that

(a) Bushing before installation **(b)** Bushing installed, window side **(c)** Isolated base, gas handling side

Figure 4.3: Pictures of the test compartment components

C2 should be larger than C1[32].

$$C_1 = 270\text{ pF}, \quad C_3 = 231\text{ pF} \tag{4.2}$$

$$\text{Given:} \quad C_3 = \left(\frac{1}{C_1} + \frac{1}{C_2}\right)^{-1} \Rightarrow C_2 = \left(\frac{1}{C_3} - \frac{1}{C_1}\right)^{-1} = \left(\frac{1}{231\text{ pF}} - \frac{1}{270\text{ pF}}\right)^{-1} = 1.6\text{ nF} \tag{4.3}$$

If the test tap is not grounded, the C1 and C2 form a capacitive voltage divider. The voltage applied to the main conductor can be derived from the voltage at the test tap through the following ratio.

$$V_2 = V_1\left(\frac{C1}{C1 + C2}\right) = 0.144 \cdot V_1 \tag{4.4}$$

As the internal structure of the bushing is unknown, a simplified internal structure has been used for construction of the FEM model. This does not impact the electric field distribution found for the electrode arrangement, but does impact the field distribution near the bushing significantly.

4.3. Measurement Circuit 1: Conventional (IEC60270)

The first measurement circuit evaluated follows the conventional configuration specified in IEC 60270. A coupling capacitor with a capacitance of 1 nF is connected to create a measurement path for the

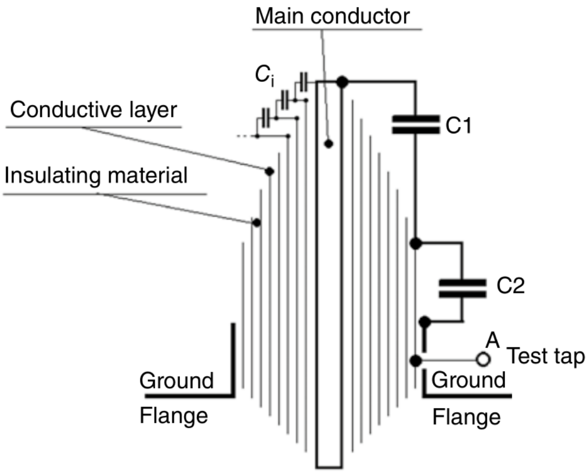

Figure 4.4: Capacitive graded bushing from [19]

apparent charge. The arrangement, which can be seen in Figure 4.5a forms a closed current loop. When the current flowing through this loop changes, an electromotive force (EMF) is induced in the same conductor. The ratio between the induced voltage and current is described by the self-inductance and depends on the physical dimensions of the loop. [33]. The self-inductance in combination with the capacitance of the coupling capacitor and the capacitive test compartment, form a series LC circuit for which the diagram can be seen in Figure 4.5b. The self-inductance is represented as a lumped inductance L_{self}, and the physical dimensions of the setup are included.

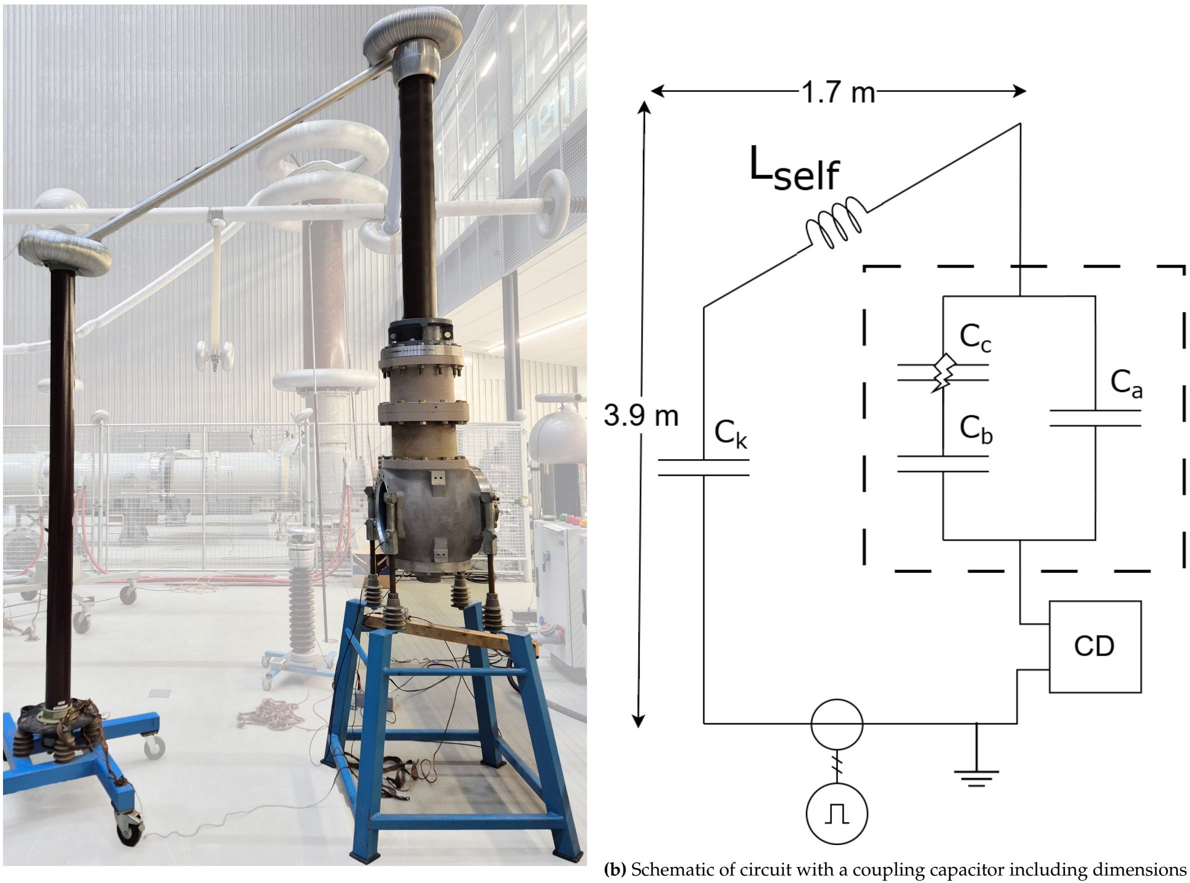

(a) The test compartment connected to a coupling capacitor

(b) Schematic of circuit with a coupling capacitor including dimensions and an Inductance L representing the selfinductance

4.3.1. Evaluation of electrical parameters

By injecting a fast pulse according to the procedure proposed in [34], the parameters of the circuit can be evaluated based on the resonance frequency. By performing this procedure with and without the capacitive test object present through shorting the device internally with a copper foil, the capacitance of the test object can be evaluated.

When the test object was absent and only the 1 nF external coupling capacitor C_k is connected, the resonance frequency is 1.63 MHz. Using Equation 4.5, the self-inductance L_{self} was found to be 9.5 µH. This value is in agreement with the loop inductance that should be expected according to [35], which suggests a value of 1 µH per meter as a rough guide.

$$f_0 = \frac{1}{2\pi\sqrt{LC_k}} = 1.63\ \text{MHz} \quad \Rightarrow \quad L_{\text{self}} = C_k \cdot \left(\frac{1}{2\pi f_0}\right)^2 = 9.5\ \mu\text{H} \tag{4.5}$$

When both the 1 nF external coupling capacitor and the test object (C_{EUT}) are connected, an increased resonance frequency of 3.5 MHz was observed. Using these resonance frequencies, the equivalent capacitance of the test object was calculated to be approximately 276 pF according to Equation 4.6.

$$f_0 = \frac{1}{2\pi\sqrt{LC_{eq}}} = 3.5\ \text{MHz} \quad \Rightarrow \quad \text{C}_{\text{EUT}} = \left(\frac{1}{C_{eq}} - \frac{1}{C_k}\right)^{-1} = 276\ \text{pF} \tag{4.6}$$

4.3.2. Resonance Issues

For this measurement circuit, the resonance frequency thus is 3.5 MHz. This resonant behavior distorts the high-frequency content of the PD pulse, resulting in a limited effective bandwidth of the detection system. Computation of PD parameters such as charge and energy are impacted by this distortion, resulting in an estimation error [34].

These effects depend on the self-inductance. For low values the parameters are overestimated through resonance, while for high values the systems acts as a filter resulting in underestimation [36].

4.4. Concept C_{a1} and C_{a2}

As this bandwidth limit is barely above the limit of 1 MHz set in IEC 60270, this limit should be improved. The key limiting factor is the self-inductance, which is related to the physical detection path. To figure out an alternative geometry for this current path, this section further investigates the capacitive test device.

The capacitance of the test compartment found in Section 4.3.1 (C_{EUT} =276 pF) is only a bit larger than the capacitance of the bushing Section 4.2.1 (C_1 =270 pF), this suggests that most of the compartment's capacitance is dominated by the coupling between the conductor in the bushing and compartments enclosure. The objective of this section is to extract this component from the total capacitance of the system. If this can be quantified and is reasonable, this capacitance can be evaluated for usage as an alternative PD path. To describe this split, we define C_{a1} and C_{a2} as follows:

- C_{EUT} (Equipment Under Test) The total capacitance of the compartment, which was evaluated in Section 4.3 based on the resonance peaks.
- C_{a1}: the capacitance between the electrode configuration and the ground plane (electrode system).
- C_{a2}: the capacitance between the conductor in the bushing and enclosure structure.

As C_{EUT} is known, C_{a2} or C_{a1} could be found if one is known as such:

$$C_{a2} = C_{\text{COMPARTMENT}} - C_{a1} \tag{4.7}$$

4.4.1. FEM simulation to estimate C_{a1}

To evaluate the value of C_{a1}, the FEM model is adapted to develop a Maxwell capacitance matrix. By disconnecting the ground plane from the test compartment, an extra terminal is created. As the ground plane is physically supported by the connection to the ground plane, this is complicated to do in the actual setup. If possible, the method described below would work in a similar manner.

Figure 4.6 shows the extra terminal, as well as the new circuit. The capacitances between terminals are described through the maxwell capacitance matrix according to Equation 4.8.

$$\begin{pmatrix} Q_1 \\ Q_2 \end{pmatrix} \mathbf{V}^{-1} = \begin{bmatrix} C_{11} & C_{12} \\ C_{21} & C_{22} \end{bmatrix} = \begin{bmatrix} C_{m11} + C_{m12} & -C_{m12} \\ -C_{m21} & C_{m21} + C_{m22} \end{bmatrix} \tag{4.8}$$

The values of interest correspond to

$$C_{m11} = C_{a2} \quad C_{m12} = C_{m21} = C_{a1}$$

By performing a source sweep, which is supplying only one terminal with a voltage while grounding the others, the values in the matrix can be evaluated. Appendix A.3 contains a detailed description of the method and the implementation for this model. The capacitance matrix is as follows:

$$\begin{pmatrix} Q_1 \\ Q_2 \end{pmatrix} \mathbf{V}^{-1} = \begin{bmatrix} C_{11} & C_{12} \\ C_{21} & C_{22} \end{bmatrix} = \begin{bmatrix} 145.15 & -3.05 \\ -3.05 & 28.6 \end{bmatrix} \quad \text{(pF)} \tag{4.9}$$

Using Equation 4.8, we extract that $C_{m11} = C_{a2} = 142.1$ pF and $C_{m12} = C_{m21} = C_{a1} = 3.05$ pF. Here it can be clearly seen that the simplified model of the bushing (Section 4.2.1) has a large impact on the evaluation of the systems capacitance. C_{11} is only 145 pF, while the capacitance C_{EUT} found through the RLC method is 276 pF. The evaluated C_{a2} thus is clearly wrong. As the geometry of C_{a1} is well described, we can use this value to estimate C_{a2}:

$$C_{a2} = C_{\text{COMPARTMENT}} - C_{a1} = 276 - 3 = 273 \text{ pF} \tag{4.10}$$

The difference between the capacitance of the bushing (270 pF) and the capacitance found here can be attributed to the capacitance from the HV conductor to the outside compartment which is not part of the bushing capacitance.

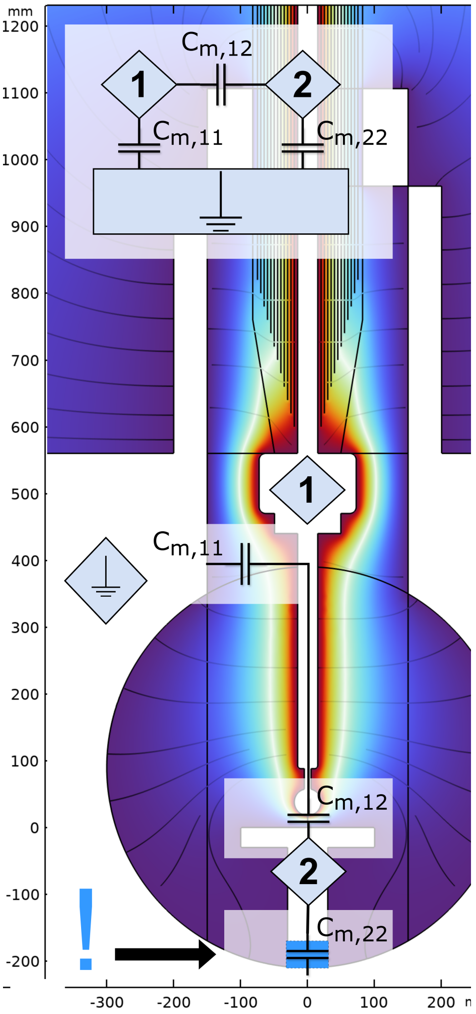

Figure 4.6: Simulation results showing the voltage distribution, overlaid with the circuit made through (digital) disconnection of the compartment to the ground plane.

4.5. Measurement Circuit 2: Internal Coupling Capacitor

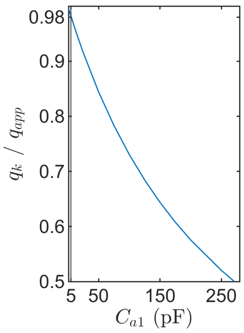

Figure 4.7: Divider ratio for different values of C_{a1}. C_{a1} of the setup is marked

If C_{a2} is used as a coupling capacitor, the dimensions of the current loop can be greatly reduced. Additionally, since $C_{a2} >> C_{a1}$ the sensitivity is increased, as the ratio according to Equation 4.11 is 0.98. Even if C_{a1} is increased through a different electrode arrangement, the current division ratio stays great as can be seen in Figure 4.7.

$$q_k = \frac{1}{1 + (C_k/C_{EUT})^{-1}} q_{app} \Rightarrow \frac{q_k}{q_{app}} = \frac{1}{1 + (C_{a2}/C_{a1})^{-1}} \tag{4.11}$$

This section details the necessary adjustments to the setup to accommodate this approach. In Figure 4.8 the circuit diagram of the conventional circuit [17] and the proposed circuit can be seen. The differences are marked and numbered. Change ① is the removal of C_k which is replaced by C_{a2}, which was made possible through the extraction of C_a into C_{a1} and C_{a2}.

4.5.1. Measurement Impedance

When a measurement resistor of 50 Ω would be used to prevent reflections in the measurement circuit, the high-pass filter constructed with the series C_{a2} has a cut-off frequency of 11.5 MHz. This high cut-off frequency would exclude a significant portion of the relevant signal spectrum, making this option undesirable. Furthermore, since the ground plane is structurally connected to the compartment, inserting a measurement resistor into its path would require significant modifications.

$$f_0 = \frac{1}{2\pi R_M C_k} = \frac{1}{2\pi \cdot 50 \cdot 276 \cdot 10^{-12}} = 11.53\,\text{MHz} \tag{4.12}$$

The usage of a HFCT, which can be placed around the rod connecting the ground plane to the compartment housing as can be seen in Figure 4.13, solves both of these problems. In Figure 4.8 the altered location is marked ②. To connect the HFCT to the oscilloscope, an SMA connector was installed through a drilled opening at the bottom of the compartment ③. Epoxy was applied to ensure the connection was gas-tight.

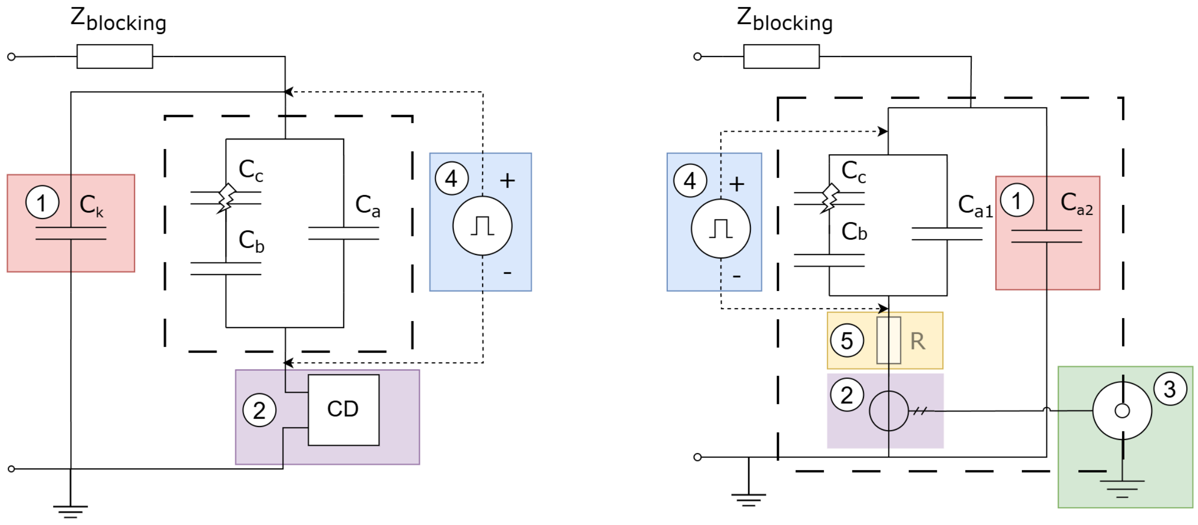

(a) Conventional Measurement circuit

(b) Measurement Circuit after modifications

Figure 4.8: The original and modified measurement circuit. The numbers are modifications required to be able to use C_{a2} as a coupling capacitor and are described in this section.

4.5.2. Calibration

The location that the calibration charge is injected must also be changed in accordance with IEC 60270. The new location is over C_{a1}, which is marked with a ④. This is only possible with the lid open, as can be seen in Figure 6.2.

This does not cause an issue, as the electric field distribution does not change for other gases, since the relative permittivity (ϵ_r) at 20 ° C can be assumed 1.00. Only after the 4th significant digit does the permittivity start to differ [12] for the gases of interest. As the lid is quite far from the HV electrode the effect on the capacitance is also limited.

The IEC 60270 requirement from Section 3.4.2, that $C_0 < 0.1 \cdot C_{EUT}$ can no longer be adhered to. Since C_{EUT} now is C_{a1}, the required treshold is $0.1 \cdot C_{a1} = 0.3$ pF. As $C_0 \approx 100$ (Section), this exceeds the limit by over two orders of magnitude.

4.5.3. Phase Synchronisation

To determine the phase location of each PD within the AC cycle, a phase-synchronized reference signal is required. This is necessary because the HFCT used in the setup has a lower cutoff frequency of 10 kHz, which excludes the 50 Hz component of the applied voltage from the recorded signal.

A separate synchronisation signal is therefore generated using a dedicated device: the SYNCH BOX WITH PHASE SHIFTER 400-01. This device creates a linear sawtooth waveform that resets at each positive zero crossing of the applied voltage. The period of the sawtooth matches that of the AC waveform, and its ramp is linear throughout the cycle, with a fixed amplitude of $\Delta V = 4.54$ V. In Figure 4.9, the AC reference signal provided to the box and the corresponding sawtooth ramp signal can be seen. When a PD event is detected, the oscilloscope simultaneously records the PD pulse and the instantaneous voltage of the sawtooth signal, from which the corresponding phase can be derived. The internal circuit diagram of this device is available in Figure 1b of [37].

In the current measurement setup, the synchronisation unit is connected to a phase different from that of the HV source, resulting in a phase difference of -120°. The AC signal of the HV source is also shown in Figure 4.9. Additionally the sawtooth signal is flat for 0.2 ms after a zero crossing, before resuming a linear ramp at approximately 0.8 ms. This would not be an issue when the phase of the source is similar to that of the experiment, as no corona is expected at the zero crossing. As a result of the shift, this drop actually occurs at $360 - 120 = 240^\circ$, which is in the region where negative PDs occur resulting in missing phase data. For this reason, the sawtooth ramp is shifted by an additional -60°, so that this zero crossing is moved to 180° in the AC HV source. These shifts are taken into account when processing the synchronisation signals.

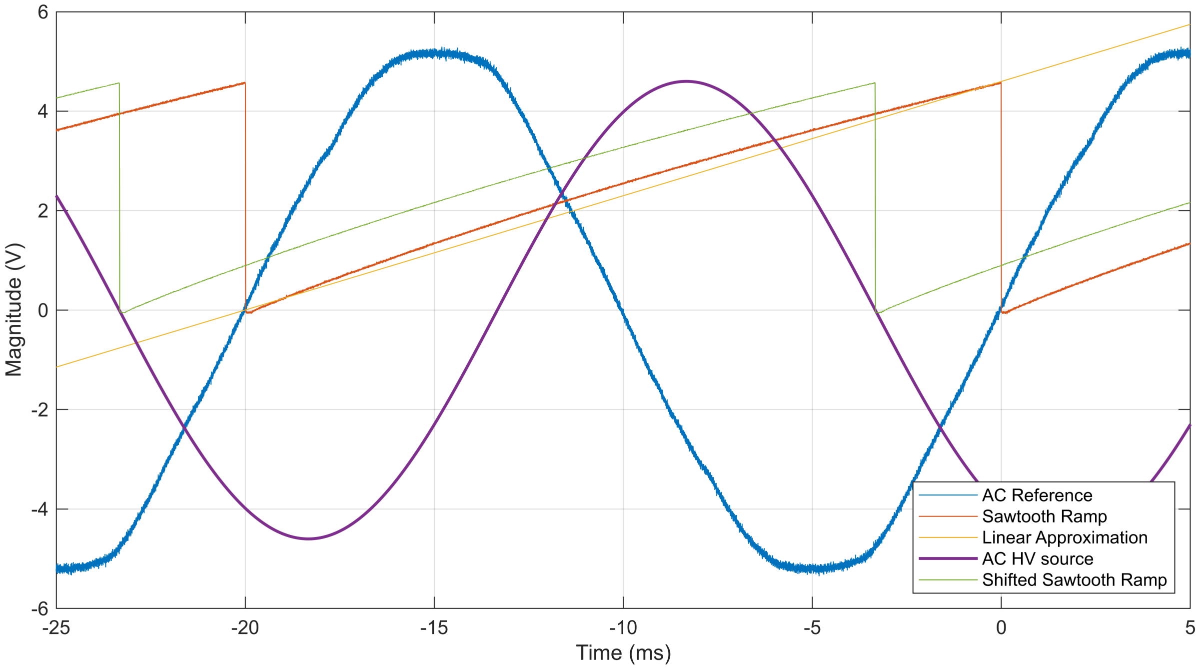

Figure 4.9: Overview of synchronization signals. Shown are the original AC reference signal, the generated sawtooth ramp, and the actual high-voltage waveform of the test setup. The sawtooth ramp is shifted by an additional 60° for which reasons are provided in the supporting text.

Translating Voltage to phase

The simplest method to relate the measured voltage to the phase, is to approximate the ramp as linear function. Function 4.13 can be directly evaluated, with $a = V_{\mathrm{ramp\ max}}/T = 4.6/0.02 = 230\ \mathrm{V\,s^{-1}}$ for a 50 Hz signal.

$$V(t) = a \cdot t \tag{4.13}$$

As the ramp signal is not linear as could be seen in Figure 4.9, this approximation results in an error which is shown in Figure 4.10. The error is maximized halfway a period, where it results in an error of 18° or 1 ms.

A polynomial function can be fitted to more accurately represent the sawtooth ramp according to Function 4.14. For $\begin{bmatrix} p1 & p2 & p3 \end{bmatrix} = \begin{bmatrix} -2890.5 & 287.34 & -0.03756 \end{bmatrix}$, the coefficient of determination (R-Squared) of the polynomial is 0.99985, which results in a negligible error.

$$V(t) = p1 \cdot t^2 + p2 \cdot t + p3 \tag{4.14}$$

The drawback is that a quadratic equation must be solved to evaluate t, which is computationally more expensive. The code for both methods is included in the hvsoftware toolbox as phaseDetermination.m (Appendix B). As the error is quite significant this is the method that is used to evaluate the phase.

$$p_1 t^2 + p_2 t + (p_3 - V_{\text{meas}}) = 0 \tag{4.15}$$

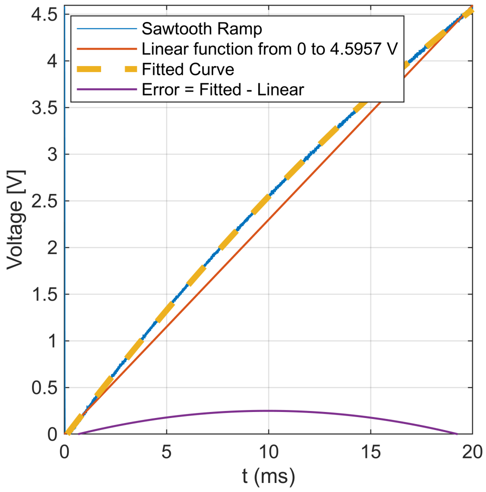

Figure 4.10: One period of the sawtooth signal, the linear approximation and the fitted polynomial. The error between the sawtooth wave and linear approximation is maximized at 10 ms

4.5.4. RLC Compensation

Although the traditional coupling capacitor is removed, the detection circuit still forms a series LC network due to residual capacitances and the self-inductance of the current loop. To evaluate the new resonance behaviour, the frequency spectrum of a corona discharge in air was analysed, revealing a peak at 144 MHz. As noted in [34], resonance caused by specific combinations of inductance and capacitance can distort the PD pulse shape, introducing significant errors in the estimation of parameters such as apparent charge and energy. To mitigate these effects, a damping resistor can be introduced in series with the test object. The damping factor is determined through Equation 4.16.

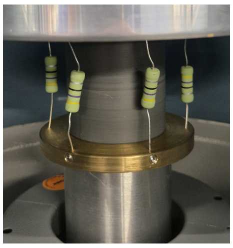

Figure 4.11: Damping resistor block present in circuit

$$\zeta = \frac{R}{2}\sqrt{\frac{C}{L}} = 1 \tag{4.16}$$

Since the self-inductance to be damped is associated with the current path through C_{a2}, the series resistance required to achieve critical damping ($\zeta = 1$) is calculated using Equation 4.17 and yields a value of $8\,\Omega$.

$$\zeta = \frac{R}{2}\sqrt{\frac{C_{a_2}}{L_{\text{self}}}} = 1 \Rightarrow R = 2\sqrt{\frac{L_{\text{self}}}{C_{a_2}}} = \frac{2}{\omega_0 \cdot C_{a_2}} = 8\,\Omega \tag{4.17}$$

A resistor damping block was developed that holds 6 resistors in a radial configuration and was installed directly under the ground plane as shown in Figure 4.11. This modification is marked ⑤ in the circuit diagram (Figure 4.8).

Based on the frequency peak, the new L_{self} is evaluated in Equation 4.18 to 4.36 nH. This is significantly lower than the initial measurement circuit, which is not only a result of the smaller current loop, but also because of the fact that this current path is radial [33].

$$f_0 = \frac{1}{2\pi\sqrt{LC_k}} = 144\text{ MHz} \quad \Rightarrow \quad L_{\text{self}} = C_{a2} \cdot \left(\frac{1}{2\pi f_0}\right)^2 = 4.36\text{ nH} \tag{4.18}$$

Resistor specifications

Six resistors of 47 Ω are placed in parallel to achieve a resistance value of 7.8 Ω. Even though PD measurement have a very small average current, the power rating should be chosen such that the resistors, which are connected between the ground plane and the ground, can manage the current at breakdown. If breakdown occurs and the resistors are not rated for the current spike, they are destroyed and the whole compartment and gas mixture are contaminated. This happened during the experiments, which is why no resistors are present in the experimental setup used to evaluate the CO_2/O_2 mixture. Figure 4.12 shows the burnt resistors and the resulting contamination.
As the step up transformer (Emil Haefely & Cie. AG. type TEOS 200/100) has a maximum operating current of 0.5 A, the required power rating of the resistors (for the calculated 8 Ω) can be evaluated as follows:

$$P_{\text{max}} = I^2 \cdot R = 0.25 \cdot 8 = 4W \tag{4.19}$$

The resistors that were selected after the breakdown incident are ceramic resistors meant for anti-pulse surge applications by KOA, which have part number PCF2C470K. As these resistors are not wound they minimal self-inductance. The resistors have a power rating of 2 W for a combined power rating of 12 W, which provides a safety margin of a factor four.

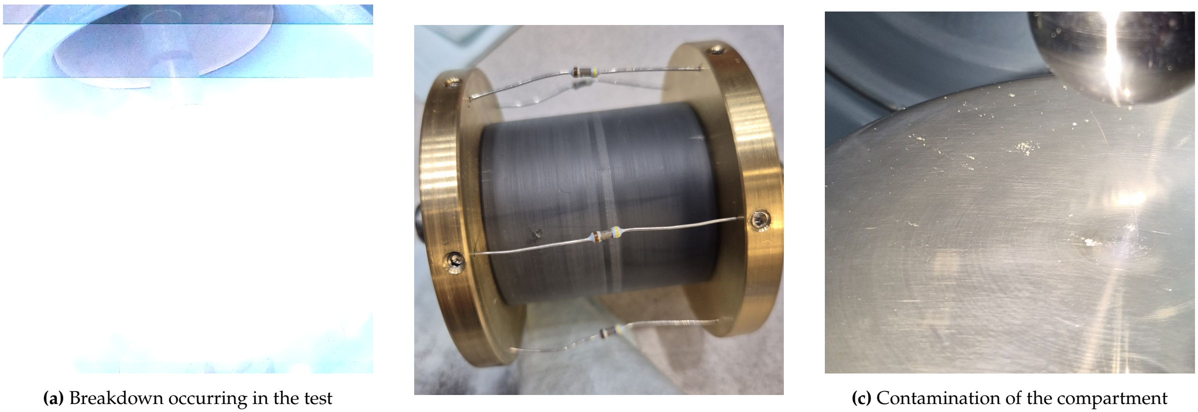

(a) Breakdown occurring in the test compartment

(b) Burnt resistors after a breakdown event.

(c) Contamination of the compartment following resistor breakdown.

Figure 4.12: Inadequately rated resistors can lead to destructive failure during breakdown events, contaminating the compartment and gas. Shown are the aftermath of such an incident and the upgraded resistor components with higher pulse tolerance.

4.6. Conclusion

This chapter presented the design and implementation of an experimental setup for evaluating the partial discharge behaviour in alternative insulation gases under AC voltage stress. A needle-plane electrode arrangement with a non-uniform electric field (η = 4.0%) was developed to generate corona discharges in the test compartment.

Initial measurements using a conventional IEC 60270 configuration revealed a resonance frequency of 3.5 MHz, limiting the effective bandwidth for PD measurements. This behaviour was attributed to the large self-inductance of the physical current loop. To address this, the internal capacitance of the setup was analysed using both measurements and FEM simulation. The total compartment capacitance (C_{EUT}) was decomposed into two components: C_{a1}, between the HV electrode and ground plane, and C_{a2}, between the bushing conductor and the GIS enclosure.

By using C_{a2} as a coupling capacitor, the resonance frequency is moved to 144 MHz, and the sensitivity is increased. Some modification to the setup are required before deciding to this as the coupling capacitance. The most significant change was the move of the measurement impedance (HFCT), which is now located in the test compartment.

To further negate the impact of the resonance frequency on the captured signals, a resistor block which critically damps the the RLC circuit was developed. This results in less pulse distortion which is beneficial for PD parameter estimation.

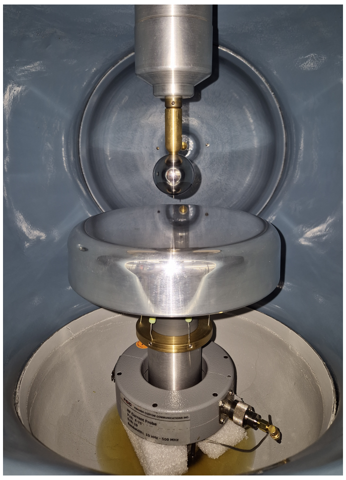

Figure 4.13: Picture showing the setup within the compartment after all modifications have been performed. Visible are the HFCT, the epoxy required for the gas tight connection and a part of the resistor damping block.

- C_{EUT} =276 pF: The total capacitance of the compartment, which was evaluated in Section 4.3 based on the resonance peaks.
- C_{a1} = 3 pF: the capacitance between the electrode configuration and the ground plane (electrode system).
- C_{a2} 273 pF: the capacitance between the conductor in the bushing and enclosure structure

5

Experimental setup

This chapter describes the setup used to perform experiments in the CO_2/O_2 mixture specified in Section 5.1.1, and is based on the measurement circuit using the internal coupling capacitor described in Section 4.5.
First the circuit and corresponding equipment of the full setup are shown and listed. In Section 5.3 a detailed overview of the measurement circuit including interconnections is shown. Some sections of the measurement circuit are analyzed using a Vector Network Analyzer (VNA) to provide further analysis on the measurement circuit.
Section 5.4 discusses the safety precautions taken while performing the experiments and finally some pictures of the experimental setup can be seen in Figure 5.5 and Figure 5.6.

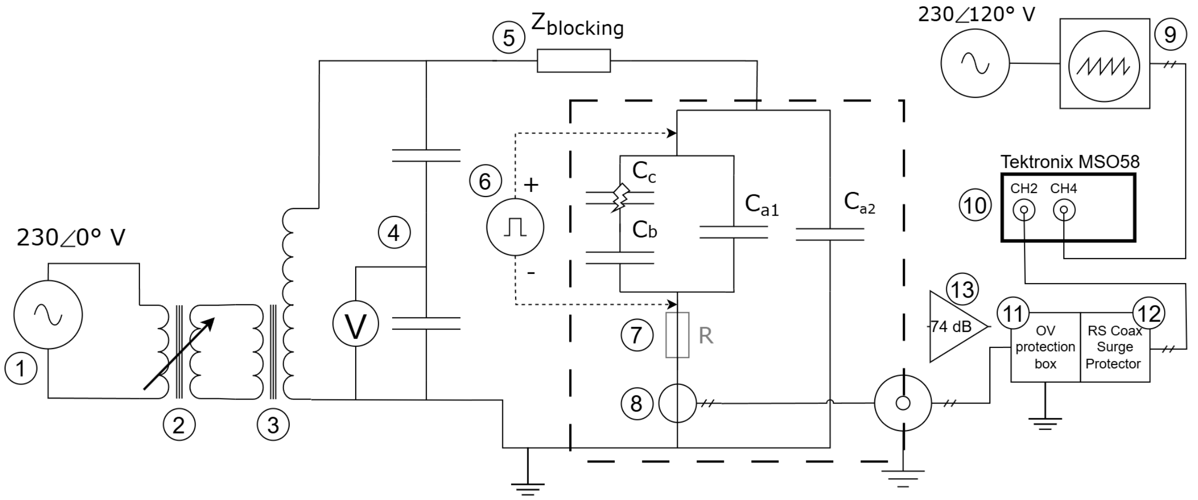

Figure 5.1: Circuit diagram of the setup with a simplified representation of the measurement circuit

5.1. Test Compartment

5.1.1. Gas mixture

The gas mixture provided was filled with a gas mixture contained in a 50 L cylinder at an approximate pressure of 64 bar. The mixture consisted of:

- Oxygen: 31.7% ± 2%
- Carbon dioxide: 68.3% ± 2%

5.2. Equipment

This section contains an overview of the equipment implemented in or used during the experiments. All the entries are numbered corresponding to the numbers used in the schematic (Figure 5.1. If available, the specific lab unit numbers are placed after the device names in brackets. Unless specified otherwise, provided voltages and currents are RMS values.

① **Power supply** 0930HVI-1/9f (9f) supplies an AC signal 230V 50Hz. The device has overcurrent protection which is rated at 80A.

② **Variable Autotransformer ("Variac")** Unknown (11.36) is an autotransformer, which consist of one winding. By changing the connection point of the secondary side to the winding, the ratio of turns between the primary & secondary side and thus the output voltage can be varied. This is done by turning a knob, which moves a carbon brush to allow for continous adjustment in connection point location. The output voltage can be ranged from 0 - 525 V, although it is unspecified what input voltage is required to achieve the maximum. The peak output power is 25 kVA, but for testing periods this should be limited to 8kVA.

③ **Step up transformer** Emil Haefely & Cie. AG. type TEOS 200/100 (20.02) is a single phase step up transformer for high voltage testing purposes. The first type number refers to the maximum output voltage (in kV), which is reached at the maximum input voltage of 500 V. The second number is the maximum load (in kVA) at that voltage level for non-continuos operation. The current limit of the protection of the transformer must be set at $I = P/U = 200/100 = 0.5$A to ensure the equipment is not damaged.

④ **Capacitive voltage divider** A capacitive divider for HV measurement purposes by Emil Haefely & Cie. AG. (41.05) is connected to measure the system voltage.

⑤ **Blocking Resistor** A 1 $k\Omega$ (±3%) resistor is used to connect the HV supply to the bushing. The resistor reduces the signal strength of interference and limits the discharge current if a breakdown were to occur. This component fullfils the role of blocking impedance specified in the circuit diagrams of IEC 60270 [17].

⑥ **Calibrator** The CAL 141 by onsite high voltage (37.11) injects a pulse with a known amount of charge at a specified time interval. The amount of charge injected can be chosen from a discrete set of values ranging from 1 pC to 10 nC. The datasheet of this specific model is not available online, but the datasheet of the CAL 165 mentions a calibrator capacitance (C_0) of 100pF.

⑦ **Critical Damping Resistor block** The damping resistor developed in Section 4.5.4 was not present during the experiments.

⑧ **HFCT** The Fischer F-75[27] is a split-core current probe with a usable bandwidth of 10 kHz to 500 MHz. The transfer impedance flattens from 1 MHz onwards where it is 1 Ω (±3dB), as can be seen in Figure 5.2. The probe is calibrated with a 50 Ω Load Impedance to prevent reflections in the measurement circuit. The inside diameter of 70 mm allows the HFCT to fit around the rod connecting the ground plane to the housing as was seen in Figure 4.13

⑨ **External Phase Synchronization Source** The SYNCH BOX WITH PHASE SHIFTER (400-01) is used to generate a Sawtooth signal as described in Section 4.5.3. Note the phase shift of the AC source supplying the SYNCH box, which is 120 degrees ahead of the HV source.

⑩ **Oscilloscope** The MSO58 by Tektronix is an 8 channel oscilloscope with a bandwidth up to 2 GHz that can capture signals with a sample rate of up to 6.25 GS/s. For an input impedance of 1 MΩ ±1%, the bandwidth is limited to 500 MHz. The acquisition memory can be segmented into a series of frames in the FastFrame mode. This allows the oscilloscope to capture the waveforms of a large number of PDs occuring in a short period, which can then be further processed.

⑪ **Overvoltage Protector** The OV protection device is in in place to prevent damage to equipment or operators when a breakdown occurs. It is rated for 5 V with a maximum current of 5 A and a capacitance of 12 pF.

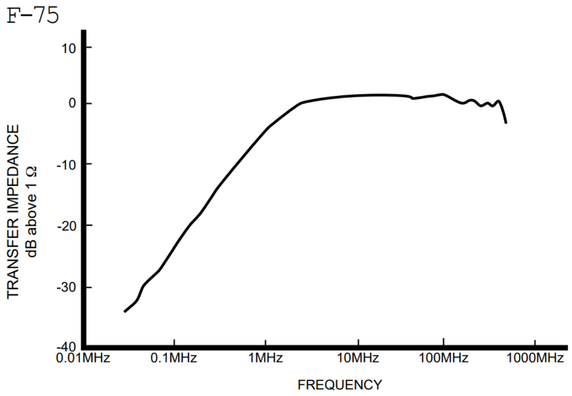

Figure 5.2: F-75 Current Probe Transfer Impedance vs Frequency according to the datasheet [27]

⑫ **Coax Surge Protector** RS 90 V / 10 kA coaxial line arrester (model 288-187), with a characteristic impedance of 50 Ω and an operating frequency range up to 11 GHz.

⑬ **Amplifier** The HCA-400M-5K-C is a High-Speed Current Amplifier and was **not** utilized for the CO_2/O_2 tests and is therefore not connected in Figure 5.1. The amplifier is used for other purposes, such as in Section 6.2.3 and is therefore listed. In those cases, it is connected between the HFCT and the OV protection box. The device [38], which is optimized for low pulse distortion has bandwidth of 400 MHz and a theoretical rise time of 1.0 ns. With a transimpedance of 5000 V/A but only a output voltage range of $\pm 1.0V$ for linear operation, the amplifier is excellent for amplifying small signals such as PD's. As the HFCT outputs a voltage to the amplifier which has a 50 Ω match, the gain of amplifier is $\frac{5000V/A}{50\Omega} = 100$.

The following equipment was used, but was not present while performing measurements, either because they are not active or are not connected.

Pressure Sensor Unknown (68.04). Displays the pressure within the test compartment,

Vacuum Pump Unknown

Vector Network Analyzer (VNA) Rhode & Schwarz ZVB 4

5.2.1. Protection Devices

Aside from the protection devices listed on the equipment list, a protective breaker is connected before the transformers which trips based on a set current limit. Not only does this protect the transformers from overloading, the protection also trips whenever a breakdown occurs. This limits the energy dissipated during the discharge, minimizing damage to the electrode configuration and equipment.

5.3. Detailed Measurement circuit

In Figure 5.3 a detailed version of the measurement circuit can be seen. The equipment is connected using coaxial cables of varying lengths, with the exception of the gas-tight connection, which is SMA. As the input impedance of the oscilloscope is set to 1 MΩ ±1%, a BNC T connector with a 50 Ω characteristic impedance is used as an impedance match.

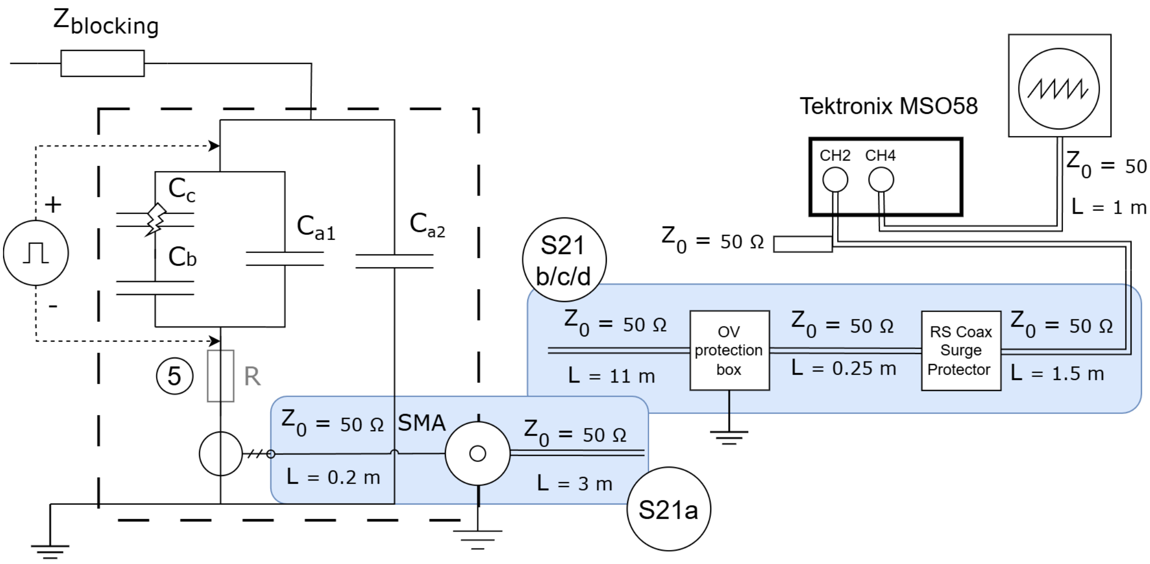

Figure 5.3: Detailed diagram of the measurement circuit

5.3.1. Transmission Parameters

The Vector Network Analyzer (VNA) was used to analyse transmission parameters of the measurement circuit. Measured were the S21 ($V_{transmitted}$ / $V_{incident}$) parameters from 300 kHz to 4 GHz for the transmission paths shown in Figure 5.3.

S21a Figure 5.4a shows the transmission from the HFCT to the outside of the compartment, through the gas tight connection. The -3 dB cutoff frequency, indicating a 50% power transmission loss, occurs at 424MHz for this section of the measurement circuit.

S21b is the transmission from the compartment to the oscilloscope with the OV protection device in place and can be seen in Figure 5.4b. The coax cable of 11 m and 1.5 m to connect the devices is also present. The -3 dB cutoff is at 148 MHz.

S21c In the same figure, the transmission parameters of the measurement circuit where the OV protection device is replaced by the RS Coax Surge Protector is seen. The -3 dB cutoff is at 284 MHz.

S21d The last transmission parameter corresponds to the same path, but with no protection devices present. The -3 dB cutoff is at 460 MHz.

5.4. Safety

The voltage can only be applied to the experimental setup whenever the area in which the HV transformer and test compartment are placed, which is surrounded by grounded fences, is fully enclosed. If this is no longer the case, such as when the entry door is opened the interlock system trips and the LV supply is cut off. In combination with a grounded stick which must be connected to the HV bus before touching any components electric shock is prevented.
Aside from adherence to the document "General rules for research testing in the high-voltage Laboratory (v1)", a risk analysis for the experiment was performed.

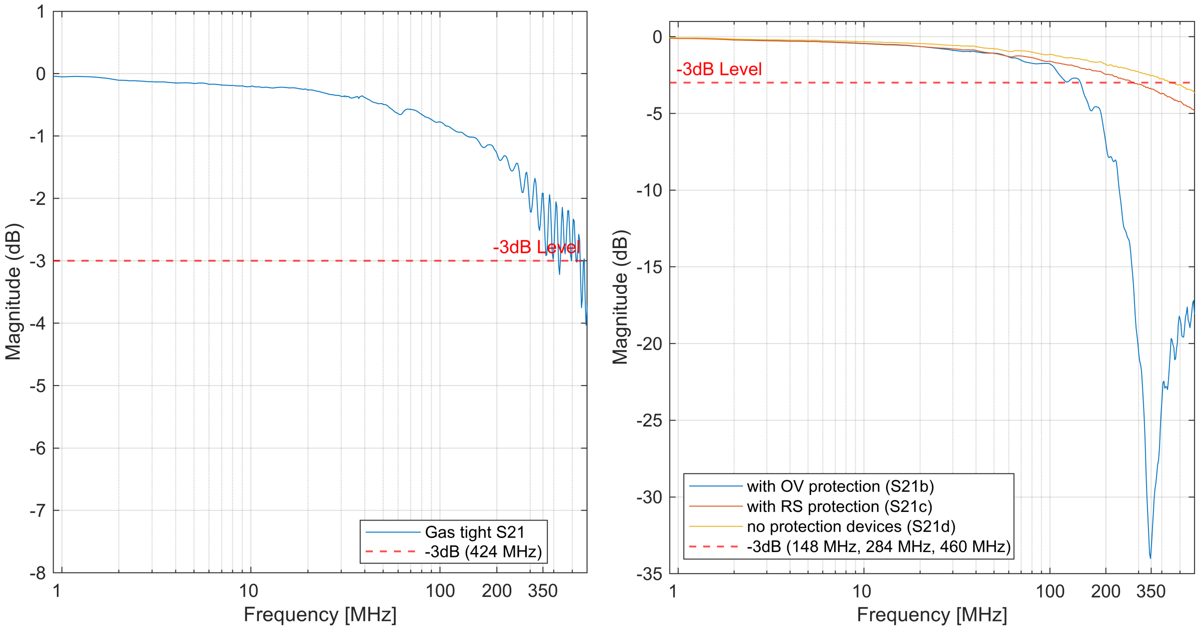

(a) S21a: Transmission parameters from the HFCT, through the gas tight connection to the outside of the compartment.

(b) S21b/c/d: Transmission parameters from the compartment to the oscilloscope

Figure 5.4: Transmission parameters of the sections shown in Figure 5.3 evaluated with a VNA.

5.5. Images of the experimental setup

Figure 5.5: Capacitive voltage divider and the HV transformer connected to the test compartment through the (blue) blocking resistor

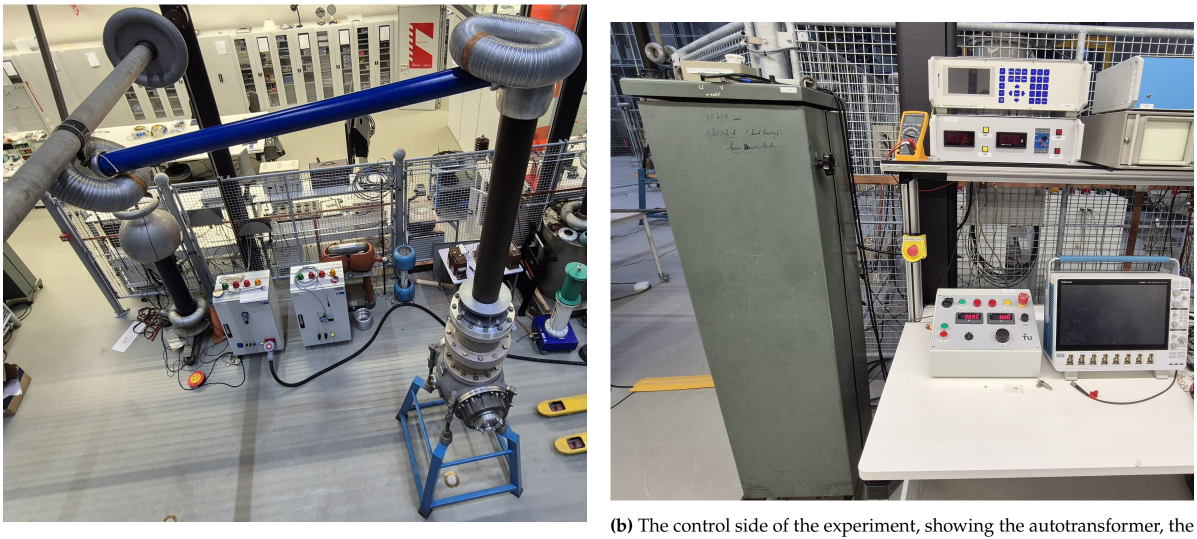

(a) Blocking Resistor which doubles as the connection to the HV source

(b) The control side of the experiment, showing the autotransformer, the oscilloscope and the control devices

Figure 5.6: Pictures of the experimental setup

6

Methodology

This chapter outlines the experimental methodology used to investigate PD behaviour in a CO_2/O_2 (70%/30%) gas mixture at varying pressure levels. The procedures for gas preparation, test execution, and data acquisition are detailed in Section 6.1. In Section 6.2 the three methods used to estimate the apparent charge are described. In addition to explaining the underlying theory, the selection of key parameters is justified. The final Section 6.3 contains a detailed description of the signal processing steps applied to each measurement set.

6.1. Test Methodology

6.1.1. Electrode preparation

The electrode configuration described in Section 4.1 is used for the experiment, and is cleaned with ethanol and lint free wipes before closing up the compartment to remove any contamination. To ensure that the needle-to-plane gap is correct, the needle was slowly lowered until the 15 mm brass distance cylinder barely made contact. Figure 4.1b shows a photograph of the electrode configuration with this distance cylinder present. The plane electrode is grounded through its physical connection to the compartment housing.

6.1.2. Gas Handling

Prior to testing, the gas compartment was evacuated to a pressure of 10 mbar and maintained at this level for 5 minutes to ensure adequate removal of residual gases. After evacuation, the chamber was filled with the premixed CO_2/O_2 70%/30% mixture up to a pressure of 0.4 MPa. The gas was allowed to settle for at least 15 minutes before starting the measurements. Additional measurements were performed at lower pressures of 0.3 MPa and 0.2 MPa by venting gas.

6.1.3. Testing Voltages

At each pressure level, AC voltage was applied to the test electrodes until the PDIV was reached. PDIV was defined as the voltage at which **repetitive** PD's were detected, repetitive being multiple per AC cycle. Further measurements were then conducted at 1.2 and 1.5 times this PDIV to observe the evolution of PD behaviour under increased electric field stress.

6.1.4. Oscilloscope Capture settings

At each of these voltage levels, 10,000 consequential pulses were recorded in the oscilloscope operating at a sampling rate of 1.5625 GS/s. Each measurement set is stored as a set of frames. Each frame contains a sampled voltage value recorded over a 1 µs time window, which includes 300 ns of data before the pulse trigger event. The sampled signal contains 1563 datapoints. The window trigger voltage threshold is set to ± 2 mV and was kept constant throughout the measurements. The threshold was selected to exceed the background noise level. Typically, the noise remained around ±0.9 mV, but it temporarily increased to ±1.6 mV during the 0.2 MPa measurement at 1.5 PDIV. Table 6.1 contains a summary of the settings.

Table 6.1: MSO58 oscilloscope settings

Setting	CH2 (PD Signal)	CH4 (Synchronization Signal)
Timebase	200 ns/div	200 ns/div
Sampling Rate	1.25 GS/s	–
Vertical Scale	Varying (based on PD magnitude)	–
Coupling	DC	DC (sawtooth starts at 0V)
Trigger	Window Trigger ±2 mV	–
Input Impedance	1 MΩ	1 MΩ

6.1.5. Verification of PD source

To verify that all recorded discharges originated from the electrode configuration under test, a control measurement was performed in which the test voltage was applied without the needle electrode installed. This step ensured that no discharges occurred elsewhere in the setup.

6.2. Apparent Charge Estimation

Three digital methods are used to estimate the apparent charge. This section outlines the underlying theory and provides a high-level description of their implementation. Detailed information about all required inputs can be found in the hvsoftware toolbox (Appendix B). The three methods and their function name in the toolbox are as follows:

- Quasi-integration with calibration according to IEC 60270 (`PDCalcCharge.IECFilter()`)
- Time Domain Integration (`PDCalcCharge.timeDomain()`)
- Frequency Domain Integration (`PDCalcCharge.freqDomain()`)

To explain the influence of key parameters and clarify how the methods operate on signals measured during the experiment, two sets of results are used. These are the lowest (0.2 MPa) and highest (0.4 MPa) pressure tests at PDIV, containing only negative corona. The differences in pulse magnitude and frequency content between these cases is maximized and as these affect the resulting charge values depending on the applied charge estimation method evaluating these signals shows how the signal characteristics play a role when performing charge estimation.and highlight how each method responds to varying signal characteristics.Their differences in frequency content and magnitude evaluate the influence of these c how these influence the methods.

6.2.1. Voltage-to-current conversion for integration methods

The integration methods require the current to evaluate the charge. As the captured signal `y[n]` is a time-varying voltage, the signal must first to be translated to a current. This is done by describing the measurement circuit, which is mainly dependent on the transfer impedance of the HFCT and amplification devices (not present during this experiment). Losses in the measurement circuit are not accounted for, as they are frequency dependent and thus complex to account for. Section 5.3.1 describes these losses, which occur primarily in the overvoltage protection and gas tight connection. As these losses (generally) increase with frequency, the spectral component of the signal is underestimated in the upper bandwidth of the HFCT. The transfer impedance of the HFCT is also frequency dependent, but is evaluated as a constant impedance of 1 Ω, which is the value within the flat region (Section 5.2). Based on these simplifications, **the current is directly proportional (factor of 1)** to the measured voltage.
This step is not necessary for the quasi-integration method, as the calibration procedure accounts for the measurement characteristics, provided that the calibration signal is captured and processed using the same setup.

6.2.2. IEC 60270 Bandpass filtering (Quasi-Integration)

The method described in this section follows the signal processing approach of IEC 60270 [17]. The next section (Section 6.2.3) contains the calibration results for the measurement setup.

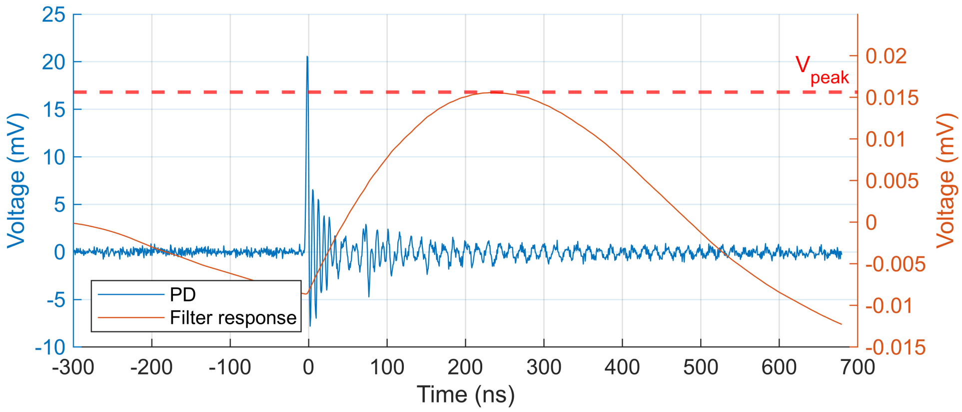

Figure 6.1: Example of a pulse before and after bandpass filtering. V_{peak}, which is used to estimate the apparent charge is marked.

By (digitally) applying a second-order Butterworth bandpass filter with a sufficiently low upper cut-off frequency compared to the frequency component of the PD, the signal is quasi-integrated. The specifications of the applied bandpass filter can be found in Table 6.2. The filter design is based on Filter #15 from [31], which demonstrated the lowest deviation from the mean on five different types of waveform representing PD signals recorded with different measurement circuits.

Quasi-integration is not true integration but instead yields a voltage output with a significantly altered waveform. The peak value of this voltage is proportional to the charge. By first evaluating the peak of this voltage output for a known calibration pulse through the use of a calibration device, a scale factor ($k = Q_{\text{cal}}/V_{\text{cal}}$) is determined. The apparent charge of each signal can be estimated by multiplying the peak value of the filtered waveform by this calibration factor, according to Equation 6.1. Figure 6.1 shows the original pulse as well as the filtered response for a PD taken in the measurement. For this charge value to be valid according to IEC60270, the requirements mentioed in Section 3.4.2 must be adhered to.

Table 6.2: Butterworth Bandpass Filter Specifications

Parameter	**Value**
Filter type	Bandpass
Filter order n	2
f_{low}	500 kHz
f_{high}	800 kHz
Normalized cutoff W_n	$\left[\dfrac{f_{\text{low}}}{2 \cdot f_s}, \dfrac{f_{\text{high}}}{2 \cdot f_s}\right]$

$$q_{\text{IEC}} = k \cdot \max(\mathtt{y_{filtered}[n]}) \tag{6.1}$$

6.2.3. IEC 60270 Calibration

To inject calibration pulses at the location in Figure 5.1 (6), the calibration device is connected between the needle and the ground plane as shown in Figure 6.2. Calibration pulses with a known charge ranging from 5 pC to 5 nC were recorded with and without the usage of an amplifier. The specifications of the calibration device and the amplifier can be found in Section 5.2.

These signals were processed according to the method described in Section 6.2.2, and the calibration factor is calculated according to Equation 6.2.

$$k = \frac{Q_{\text{cal}}}{V_{\text{peak}}} \quad \text{where } V_{\text{peak}} = \max(\mathtt{y_{bandpass\ filtered}[n]}) \tag{6.2}$$

For each calibration level 100 waveforms were captured. At each calibration level the calibration factor was calculated for five manually selected waveforms to ensure calibration signals and not interference is used to evaluate k. The average of the five calibration factors is evaluated to arrive at a single value for k. This process was repeated for a range of charge values to arrive at the calibration factors listed in Table 6.3. The calibration factor set obtained with the amplifier includes an additional column showing the factor multiplied by 100, which is the amplifier gain, to enable comparison with the calibration

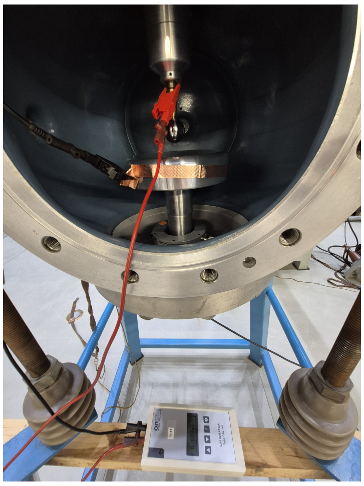

Figure 6.2: Picture showing the connection of the calibration device to the circuit

factors measured without amplification.

Table 6.3: Calibration Factors ($k = Q_{\text{cal}}/V_{\text{max}}$) for different injected charge calibration values

Calibration Charge (pC)	**With Amplifier**		**No Amplifier**
Q_{cal}	k	$k \cdot 100$	k
5	0.867×10^{-8}	0.867×10^{-6}	(Below Noise floor)
50	1.76×10^{-8}	1.76×10^{-6}	1.36×10^{-6}
100	1.76×10^{-8}	1.76×10^{-6}	1.89×10^{-6}
200	1.77×10^{-8}	1.77×10^{-6}	2.07×10^{-6}
500	1.83×10^{-8}	1.83×10^{-6}	1.64×10^{-6}
1000	2.48×10^{-8}	2.48×10^{-6}	1.77×10^{-6}
2000	4.00×10^{-8}	4.00×10^{-6}	1.76×10^{-6}
5000	(Amplifier Saturation)		1.75×10^{-6}

Manual selection is necessary to avoid basing the calibration factor on interference, which the measurement circuit with the amplifier is particularly susceptible to. This issue can be seen in Figure 6.3, which shows several detected waveforms, one of which is interference (Frame 1). Selection is based on evaluation of the signals in the time domain, as calibration pulses can easily be distinguished from interference. Calibration pulses have a consistent waveform as can be seen in Figure 6.4b compared to interference seen in Figure 6.3.

With an ideal measurement circuit the calibration factor should be consistent over the full range of injected charges, which is not the case. For both set of measurements k decreases for calibration pulses with a smaller magnitude. This increase in peak value of the filtered signal ($k \propto \frac{1}{V_{\text{peak}}}$) can be explained by comparing the 50 and 100 pC calibration signals captured without an amplifier. As shown in Figure 6.4a, the 50 pC calibration pulses (Frames 3 & 7) are barely distinguishable from the background noise. For the 100 pC (Figure 6.4b) pulses, the difference between the calibration pulse and noise is much larger. As the background noise is also quasi-integrated, the addition of noise to the calibration pulse results in an increased voltage peak value, leading to an underestimation of k. The smaller the calibration pulse, the greater the underestimation due to the relatively greater influence of noise.

For the calibration factors found with the amplifier this effect is also present, but there is an additional effect for larger charge values. As the amplifier approaches its non-linear operating region (see Section 5.2), the output voltage no longer scales linearly with the input. This results in a reduced peak voltage, which increases the calibration factor starting from a calibration charge of 500 pC. At 5 nC, the output signal of the amplifier becomes clipped, and is fully saturated.

In summary, the calibration factor k is sensitive to both noise and nonlinearity. This is not necessarily

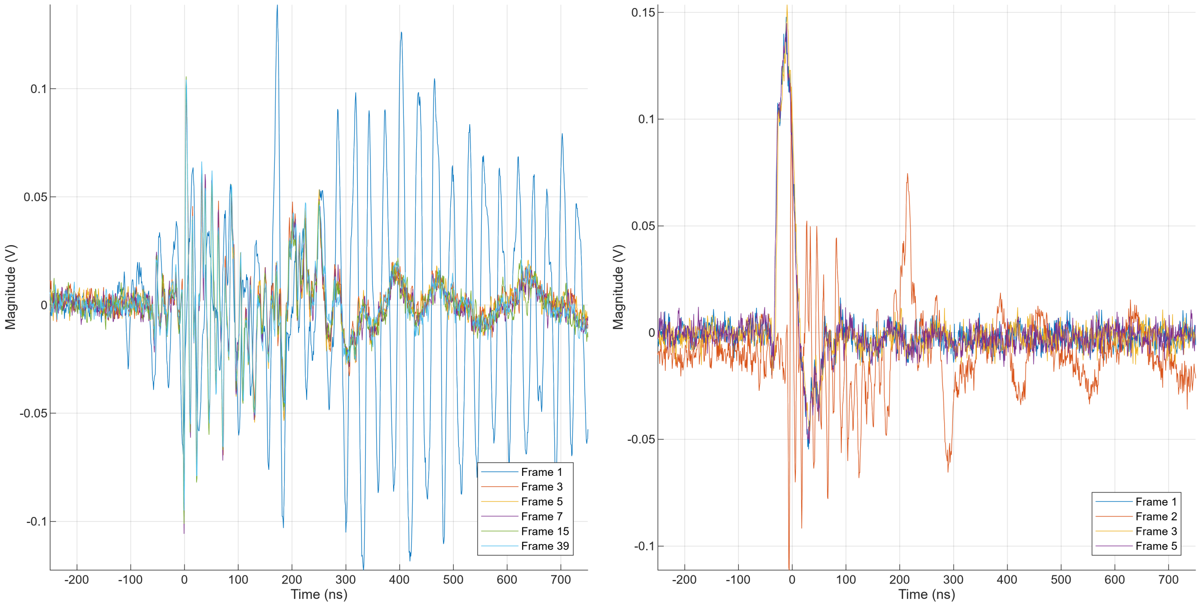

(a) 5 pC Calibration Signal with Amplifier in circuit **(b)** 50 pC Calibration Signal with Amplifier in circuit

Figure 6.3: Calibration Signal with 5000x Amplifier in circuit

an issue, as the concept of the IEC 60270 calibration method is that the calibration pulse emulates the PD pulse. If this is the case, the impact of the measurement setup is equivalent and the effects are compensated for through k. For this reason, IEC 60270 specifies that the calibration factor should be based on a calibration charge which should be within 50% to 200% [17] of the PD magnitude.

6.2.4. Time Domain Integration

Integration of the current signal over time allows for direct evaluation of the apparent charge. The trapezoidal method is used to approximate the area under the curve constructed by a set of sampled datapoints:

$$q_{\text{Time}} = \int i(t)dt \approx \sum_{n=i_a}^{i_b} \frac{\texttt{y[n]} + \texttt{y[n+1]}}{2} \cdot \Delta t \quad \text{where } \Delta t = \frac{1}{F_s} \tag{6.3}$$

Before integration, the waveforms are filtered by a low-pass filter with a cut-off frequency f_c of 25 MHz. The originally unipolar PD pulse is detected as an oscillatory pulse, due to the response of the measurement circuit. This oscillation affects integration, and as a result the method can no longer be used to correctly estimate the apparent charge [31]. The source proposes the usage of a low-pass filter to address this issue. Filtering has the additional benefit that the integration limits can now be easily evaluated again. These are the zero crossings of the first peak, called i_a and i_b in Equation 6.3. By limiting integration to these limits, the effect of noise and disturbances can be mitigated [31].

Table 6.4: Butterworth Low-Pass Filter Specifications

Parameter	Value
Filter type	Low-pass
Filter order n	4
Cut-off frequency f_c	25 MHz
Normalized cut-off W_n	$\frac{f_c}{F_s/2}$

The filter specifications can be found in Table 6.4. The f_c of 2 MHz proposed by the paper has been adapted to better suit the experiment. In Figure 6.5 a single PD measured at PDIV for two pressure levels (0.2 MPa & 0.4 MPa) can be seen. Overlaid are low-pass filtered versions of the PD for different cut-off frequencies, with the version filtered with the selected f_c of 25 MHz having a thicker line. This value removes the oscillations of the very fast PDs, while keeping waveform detail and limiting the integration range.

Figure 6.6 shows that the zero crossings of the filtered signal can now easily be evaluated. Using these indices as bounds, the integration can now be performed according to Equation 6.3 to evaluate the area

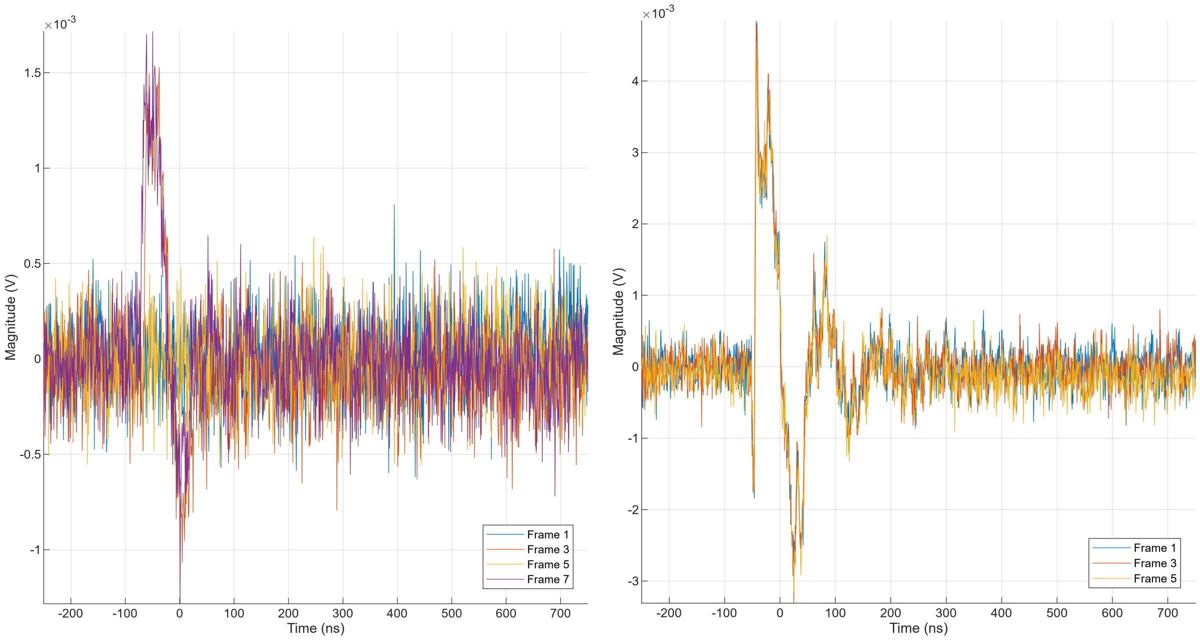

(a) 50 pC Calibration Signal without Amplifier in circuit

(b) 100 pC Calibration Signal without Amplifier in circuit

Figure 6.4: Calibration Signal without Amplifier

under the curve, marked in blue.

6.2.5. Frequency Domain Method

Apparent charge estimation in the frequency domain is based on analysis of the signal's frequency spectrum. As the integral of a signal corresponds to the DC component of its Fourier transform, the charge could be evaluated according to Equation 6.4.

$$q = \int i(t)\,dt \approx \sum_{n=0}^{N-1} i[n] \cdot \Delta t = \frac{I[\omega = 0]}{F_s} \tag{6.4}$$

However, the HFCT is not capable of measuring the DC component, which means that the information required is not available. Using the property of a fast PD signal that it has a flat frequency spectrum within the bandwidth of the measurement system, the DC component can be extrapolated from the spectral magnitude at non-zero frequency. Figure 6.7 from [31] illustrates this concept, where f_1 is 1 MHz for the measurement circuit, which is the start of the flat frequency band of the HFCT.

In practice, the full measurement circuit does not have a flat transfer function as in the image, which is the source [31] proposes to evaluate the spectral component only within a limited frequency range. Within this lower frequency range, the DC component is extrapolated based on the maximum spectral component. The upper limit f_{lim} (in Hz) is chosen such that $f_1 \leq f_{\text{lim}} \leq f_2$. As the FFT is based on frequency bins, f_{lim} is translated to an index based on the resolution of the frequency bins. The apparent charge evaluated based on the spectral peak within this frequency range as follows:

$$q_{\text{Freq}} = \frac{1}{F_s} \max_{k \in [1,\ldots,k_{lim}]} |\mathrm{Y[k]}| \quad \text{where } k_{lim} = \left\lfloor \frac{f_{lim} \cdot N_{samples}}{F_s} \right\rfloor \quad \text{and } \mathrm{Y[k]} = \mathrm{FFT}(\mathtt{y[n]}) \tag{6.5}$$

Figure 6.8 shows the frequency spectrum of a single PD measured at PDIV for two pressure levels (0.2 MPa & 0.4 MPa). As shown in Figure 6.8b, the DC component is not captured. The PDs at 0.2 MPa have the smallest (relatively) flat spectral band up to about 30 MHz, which is therefore the frequency selected for f_{lim}.

Figure 6.9a shows five PDs from the 0.2 MPa measurement set which were selected based on the similarity of their peak magnitude in the time domain. The frequency spectrum of interest for the estimation

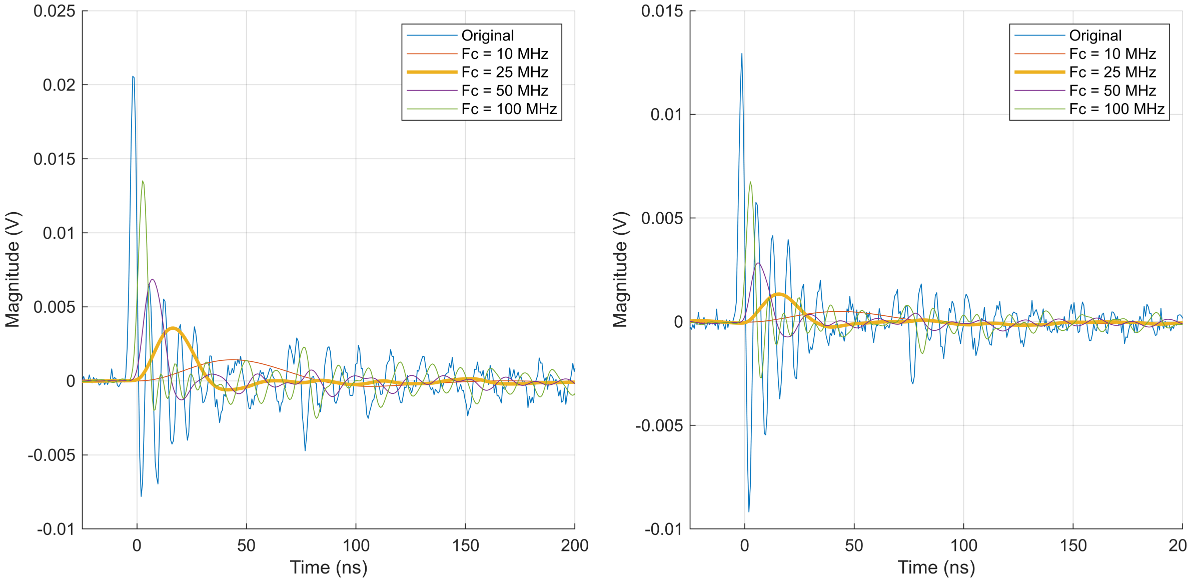

(a) Low-pass filtering of sample pulse 0.2 MPa 1 PDIV

(b) Low-pass filtering of sample pulse 0.4 MPa 1 PDIV

Figure 6.5: Variations in f_c for the low-pass filter of Table 6.4 applied to 2 measured signals.

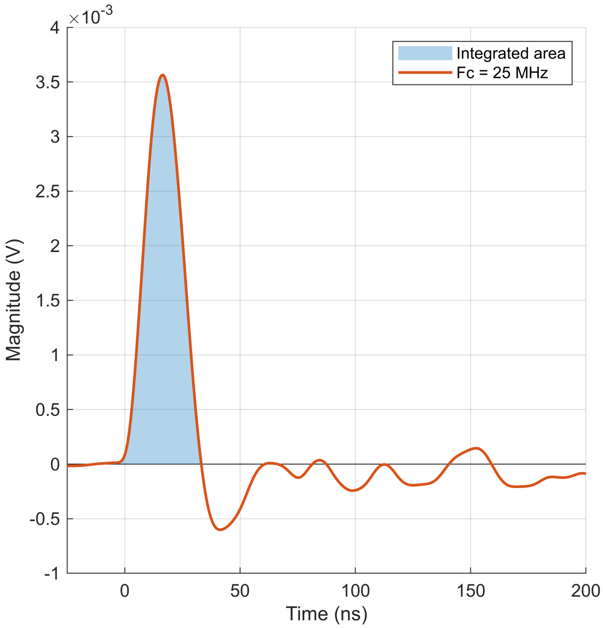

Figure 6.6: Integration limits for the sample from the 0.2 MPa 1 PDIV measurement set filtered with a f_c of 25 MHz.

method is shown in Figure 6.9b. Although the signals have a similar spectral mean component, they have a high variability. Table 6.5 shows the estimated charge of these PDs for a f_{lim} of 5 MHz and 30 MHz. At the lower frequency limit of 5 MHz, the estimated charge values show considerable variation, despite being expected to be relatively consistent. This difference arises from the inter-signal variability in spectral content, which is less of a concern when the frequency content is evaluated over a larger range. This does result in a more consistent evaluation of the charge, but as the maximum of the highly variable signal is taken, this does result in an overestimation of the charge. Instead of taking the maximum value, the method is therefore adapted to evaluate the mean value over $[f_1, f_{\text{lim}}]$. The charge values found using this method and for comparison the time domain integration method can also be found in Table 6.5.

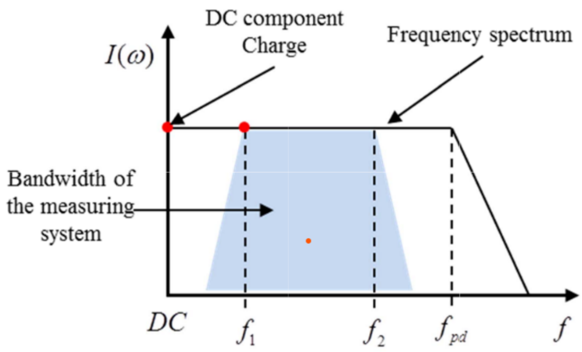

Figure 6.7: Theoretical frequency spectrum of a fast pulse showing a flat region until the frequency f_{pd} and the DC component, which is related to the pulse charge. Figure 4 in [31].

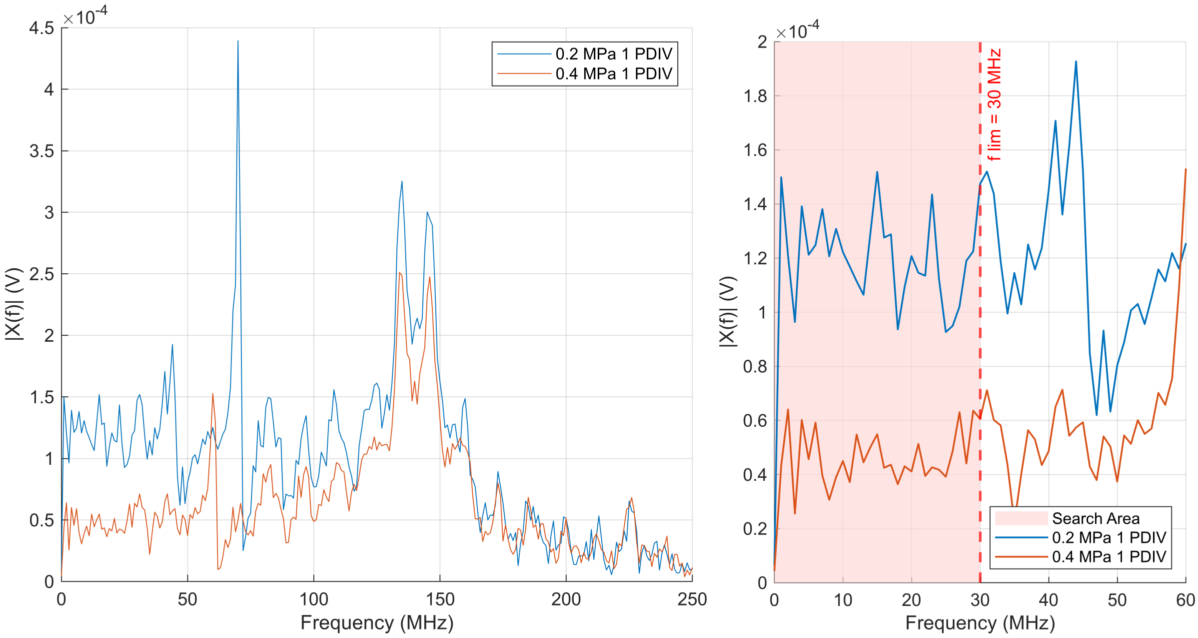

(a) Full Frequency Spectrum

(b) Frequency Spectrum for region of interest

Figure 6.8: Frequency Spectrum of sample pulse 0.2 & 0.4 MPa for 1 PDIV

Table 6.5: Comparison of charge estimation results for the discharges shown in Figure 6.9. The frequency domain method is evaluated using both the maximum and mean magnitude methods. For reference, the charge found using the time domain integration method is also included.

Frame #	**qFreq max()** (pC) $f_{\mathrm{lim}} = 5$ MHz	$f_{\mathrm{lim}} = 30$ MHz	**qFreq mean()** (pC) $f_{\mathrm{lim}} = 30$ MHz	**qTime** (pC) $f_c = 25$ MHz
68	46.1	46.1	29.3	20.3
575	26.2	41.6	25.1	20.3
606	38.2	38.8	26.6	16.9
1236	27.7	42.0	27.0	26.0
1243	33.7	37.3	23.0	24.2

6.2.6. Summary

Three methods are used to evaluate the apparent charge. The IEC method is based on the conventional method found in IEC 62070. By describing the measurement circuit in detail, the measured voltage can now directly be related to a current, which allows for alternative charge estimation methods. These two estimation techniques are adapted from [31] and are the time integration and frequency domain method.

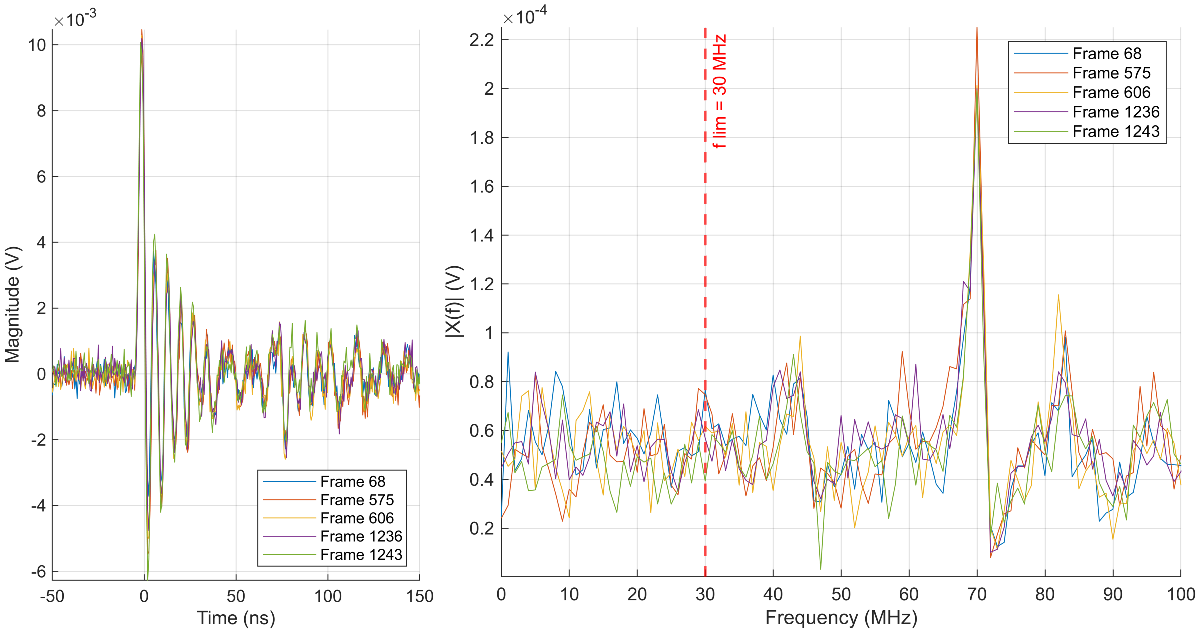

(a) Time Domain

(b) Frequency Spectrum of interest

Figure 6.9: Evaluation of Frequency Spectrum for a set of similar discharges (0.2 MPa for 1 PDIV)

$q_{\textbf{IEC}}$

For the IEC method, the signals are first filtered with a bandpass filter specified in Table 6.2. The maximum value of the filtered signal is multiplied by a calibration factor k of 1.36×10^{-6}. This is the factor found for the 50 pC calibration charge without amplifier from Table 6.3. This calibration charge value is nearest to the PD charge magnitudes found for this method during the experiments, which are below 50 pC.

$$q_{\text{IEC}} = k \cdot \max(\texttt{y}_{\texttt{filtered}}\texttt{[n]}) \quad \text{where } k = 1.36 \times 10^{-6} \tag{6.6}$$

$q_{\textbf{Time}}$

For the Time integration method, the signals are first filtered with a low-pass filter specified in Table 6.2. The f_c of 25 MHz is different from the 2 MHz found in [31]. The zero crossings of the now no longer oscillatory signal serve as the bounds for trapezoidal integration.

$$q_{\text{Time}} = \sum_{n=i_a}^{i_b} \frac{\texttt{y}_{\texttt{filtered}}\texttt{[n]} + \texttt{y}_{\texttt{filtered}}\texttt{[n+1]}}{2} \cdot \Delta t \quad \text{where } \Delta t = \frac{1}{F_s} \tag{6.7}$$

$q_{\textbf{Freq}}$

For the frequency domain estimation method, the signal is converted to the frequency domain through a Fast Fourier transform. Based on the mean value instead of the maximum of the spectral magnitude within a limited frequency range ($[f_1, f_{\text{lim}}]$ = [1 MHz, 30 MHz]) the DC component is approximated. As the DC component divided by the sampling frequency F_s is equivalent to the integral of the current signal, the output is the charge.

$$q_{\text{Freq}} = \frac{1}{F_s} \text{mean}_{k \in [1,\ldots,k_{lim}]} |\text{Y[k]}| \quad \text{where } k_{lim} = \left\lfloor \frac{f_{lim} \cdot N_{samples}}{F_s} \right\rfloor \quad \text{and } \text{Y[k]} = \text{FFT}(\texttt{y[n]}) \tag{6.8}$$

6.3. Signal Processing Methodology

After finishing the results the measurements 9 sets of 10000 waveforms that should contain PD events. The captured signal for the synchronisation source is directly simplified to a single voltage value per frame as this signal is effectively flat over the captured length of 1 μs.
The first part of this section describes the processing required required to determine parameters relating to a single PD. These are the phase in the AC wave, the apparent charge found using the different estimation methods. The peak value of the current in the waveform was additionally evaluated.
Each waveform is evaluated to one value per parameter type. As the complete set of a measurement, or all 10000 values are still a significant number statistical analysis are used to further quantify the results. The statistical methods used are described in Section 6.3.2.

6.3.1. Determination of PD parameters

This section describes the steps performed on all 10000 waveforms captured for a single dataset to evaluate the PD parameters, which can also be seen in Equation 6.9. N is the number of datapoints present in the sampled signal, which is 1563. M is the total number of waveforms captured in a measurement, which is 10000.

- Determine the phase based on simplified voltage magnitude from the synchronization signal according to the method described in Section 4.5.3.
- Remove any DC offset in the PD signal by subtracting the mean value of the first 100 datapoints. At a sampling frequency of 1.5625 GS/s, this corresponds to the first 64 ns of the signal.
- Determine the peak current magnitude ($I_{\text{peak},i}$) from the maximum absolute value in the time domain.
- Before calculating the PD parameters, any polynomial trend in the signal was removed.

$$\mathbf{Y} = \begin{bmatrix} \texttt{y[1,1]} & \dots & \texttt{y[1,N]} \\ \vdots & \ddots & \vdots \\ \texttt{y[M,1]} & \dots & \texttt{y[M,N]} \end{bmatrix} \quad \Rightarrow \quad \mathbf{i}_{\text{peak}} = \begin{bmatrix} i_{\text{peak}}[1] \\ \vdots \\ i_{\text{peak}}[\text{M}] \end{bmatrix}, \quad \mathbf{q}_{\text{IEC}} = \begin{bmatrix} q_{\text{IEC}}[1] \\ \vdots \\ q_{\text{IEC}}[\text{M}] \end{bmatrix}, \quad \text{etc.} \tag{6.9}$$

6.3.2. Processing steps used for analysis of the results

The results belonging to a measurement at a specific pressure and voltage level are further evaluated through the methods described here.

- The mean and standard deviation were calculated for the phase degree and the I_{peak}.
- Additionally, the Pearson correlation coefficient is calculated between all of the magnitude methods. Equation 6.10 shows the calculation for the correlation value between q_{IEC} and i_{peak}, but the variables can be replaced to evaluate the correlation between the other magnitude parameters. All correlation coefficients (7 options for 4 sets of data) are calculated.

$$r(\mathbf{q}_{\text{IEC}}, \mathbf{i}_{\text{peak}}) = \frac{\sum_{m=1}^{M} \left(q_{IEC,m} - \bar{q}_{IEC}\right)\left(i_{\text{peak},m} - \bar{i}_{\text{peak}}\right)}{\sqrt{\sum_{m=1}^{N} \left(q_{IEC,m} - \bar{q}_{IEC}\right)^2} \sqrt{\sum_{m=1}^{N} \left(i_{\text{peak},m} - \bar{i}_{\text{peak}}\right)^2}} \tag{6.10}$$

6.3.3. Time based processing

6.3.4. Interference suppression

Two digital interference suppression methods were implemented, but were **not** necessary to evaluate the measurement results of this experiment. The implementations can be found in the HV toolbox (Appendix B) in `MeasurementSeperation.m`. The two implemented methods operate as follows:

Discarding pulses based on Similarity. External interference has a different waveshape, an example is Frame 39 in Figure 6.3a.

Similarity As external interference has a different waveshape, waveforms can be discarded based on similarity to a known good PD. An example of interference can be seen in Figure 6.3a, where Frame 39 is interference. After cross correlating the signals to the known good pulse, frames which have a poor similarity can be discarded.

Gating As the PDs in this setup are fabricated through the electrode configuration, the type of PD is known. As each type normally occurs within a certain locations of the AC wave, pulses can be discarded based on their phase. This is a form of gating [19].

7

Results

7.1. HV side Corona Discharge in CO_2/O_2 (70%/30%)

A total of nine measurement sets were recorded, each consisting of 10,000 pulses. The measurements were carried out at three different pressure levels: 0.2 MPa, 0.3 MPa, and 0.4 MPa. For each pressure level, PD activity was evaluated at three voltage levels: at the PD inception voltage (PDIV), and at 1.2 and 1.5 times the PDIV. None of the recorded pulses were discarded. All results presented in this section are based on the complete set of 10,000 discharges per measurement. Almost all of the PDs occurred within the negative part of the AC cycle. Only for the measurements at 1.5 PDIV at 0.2 MPa and 0.4 MPa were cycles observed with multiple PDs in the positive part. For the 0.4 MPa measurement this was only 1 cycle with 4 PDs, whereas at 0.2 MPa, positive PDs appeared in nearly every cycle.

7.1.1. PDIV & Repetition Rate

The PD inception voltage was determined for each pressure level, after which the 1.2 and 1.5 times PDIV were calculated. The voltage levels at which each measurement was taken, including the peak voltage, can be found in Table 7.1. This table also includes the repetition rate. As expected, the repetition rate increases with applied voltage. Notable is the lower repetition rate at PDIV for the 0.3 MPa measurement compared to those at 0.2 and 0.4 MPa.

Table 7.1: Voltage, peak voltage, and repetition rate at different pressure levels and PDIV multiples

Pressure (MPa)	**PDIV** (%)	$\mathbf{V}_{\mathrm{RMS}}$ (kV)	$\mathbf{V}_{\mathrm{Peak}}$ (kV)	**Repetition Rate** (pulses/s)
0.20	100	15.2	21.4	740
	120	18.2	25.7	5143
	150	22.7	32.2	21173
0.30	100	16.0	22.6	357
	120	19.2	27.2	3700
	150	24.0	33.9	11862
0.40	100	19.7	27.9	761
	120	23.6	33.4	5105
	150	29.6	41.8	17403

7.1.2. PD Waveform Analysis

Sample Waveforms – Negative PD

Figures 7.2 show a single captured waveform at each applied voltage level for all three tested pressures. The presented waveforms are not representative of the full measurement set, but provide a general impression of the signal characteristics. The measured pulse shapes are consistent within each pressure level. The amplitude varies for different voltages, but no conclusions should be drawn from this. As later can be seen, the amplitude varies within each measurement set, but has a consistent mean value at

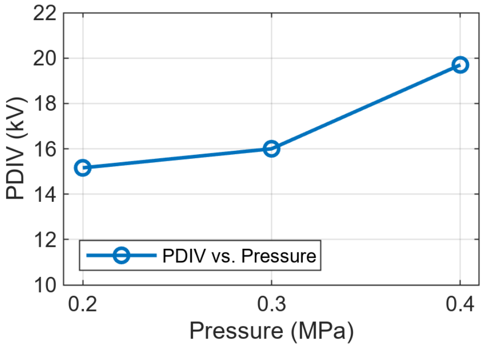

Figure 7.1: PDIV versus Pressure

a certain pressure level. As the pressure increases, a reduction in peak amplitude can be observed. At a pressure of 0.4 MPa, the waveforms have a relatively larger oscillatory swing compared to those recorded at 0.2 MPa. This indicates that the higher pressure waveforms contain higher frequency components at elevated pressures. The main pulse is followed by a series of repetitive excitations. These excitations occur with a period of approximately 13 ns.

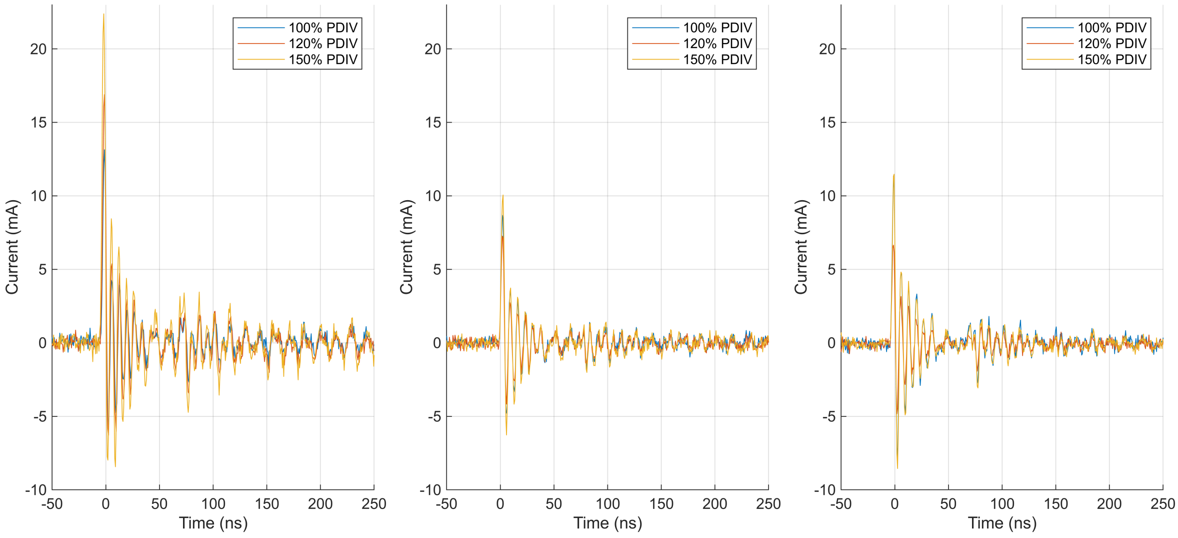

(a) 0.2 MPa **(b)** 0.3 MPa **(c)** 0.4 MPa

Figure 7.2: A waveform for negative PDs captured at a voltage of 100%, 120% and 150% PDIV. The figures show the waveforms at a pressure level of (a) 0.2, (b) 0.3 and (c) 0.4 MPa.

Risetime

The risetime (10% to 90%) of partial discharge pulses was evaluated for negative PDs in each measurement set by averaging the risetime of the first 20 PDs. Positive PDs were only analysed at 0.2 MPa for 150% of the PDIV, as this was the only case where more than 20 positive PDs were recorded. The results are summarized in Table 7.2.

No significant change in rise times was observed between any of the measurements.

Figure 7.3 shows the frequency content of three discharges at different pressure levels. As the frequency content does not significantly change for measurements at a certain pressure value, discharges are only shown at 1.0 PDIV. A spike in magnitude can be seen at 60 to 70 MHz, which moves to a lower frequency range as the pressure increases. By evaluating the difference between the 0.3 and 0.4 MPa measurement, it additionally becomes clear that the magnitude at this spike reduces as the pressure is increased.

An additional peak around 144 MHz is visible, corresponding to the resonance observed during the 0.1 MPa air measurement described in Section 4.5.4.

Table 7.2: Mean risetime of the first 20 PD pulses at different pressure levels and PDIV values.

Pressure (MPa)	**PDIV** (kV)	**Mean Risetime Neg. PD** (ns)	**Mean Risetime Pos. PD** (ns)
0.20	100	2.9	-
	120	2.8	-
	150	2.9	2.9
0.30	100	2.8	-
	120	2.8	-
	150	2.9	-
0.40	100	2.6	-
	120	2.7	-
	150	2.8	-

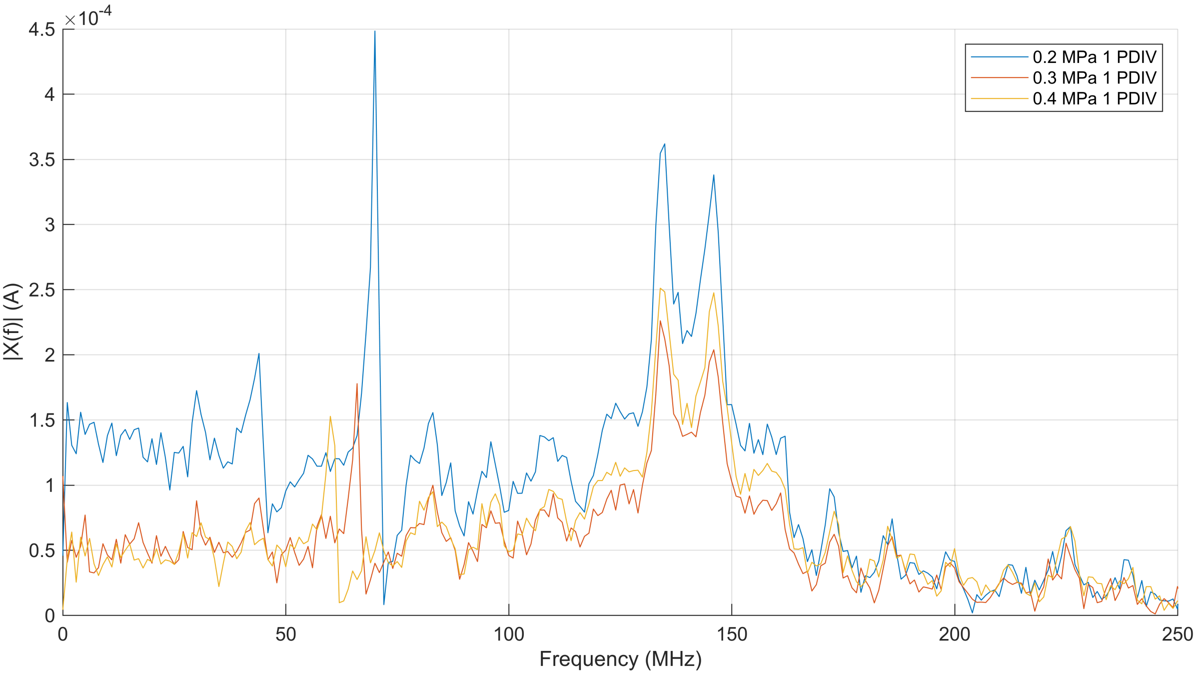

Figure 7.3: Single-Sided Amplitude Spectrum of a single waveform at each pressure level

7.1.3. PD location in AC cycle

Table 7.3 shows statistics on the phase location of PDs occurring in the negative part of the AC cycle. As the applied voltage increases, the standard deviation of the phase angle also increases. This indicates that PDs occur across a broader portion of the cycle. The PDs occuring on the positive cycle, at the 0.2 MPa 1.5 PDIV measurement, are centered around 102 ° For the 102 degrees for 0.2 MPa 1.5 PDIV

As the applied voltage increases, the standard deviation of the phase angle also increases. This indicates that partial discharges (PDs) occur across a broader portion of the negative half-cycle of the AC waveform. For example, at 0.2 MPa and 150% PDIV, the standard deviation reaches 23.5°, corresponding to a spread of over 100° within the negative cycle.

7.1.4. Phase-Resolved Partial Discharge patterns

Using these phase angles, PRPD patterns are constructed for each measurement set using the peak current amplitude. Figures 7.4, 7.5, and 7.6 show the PRPD patterns for the mixture at pressure levels of 0.2 MPa, 0.3 MPa, and 0.4 MPa, respectively.
A voltage related magnitude can be seen for the 0.2 MPa measurement in Figure 7.4. This effect becomes less pronounced as the pressure is increased. While it remains observable at 0.3 MPa (Figure 7.5), it is no longer apparent at 0.4 MPa.

Table 7.3: Phase angle statistics of negative PDs at different pressure and PDIV levels

Pressure (MPa)	PDIV (%)	# Pos. PDs	# Neg. PDs	Mean Phase (°)	Std (deg)
0.2	100	0	10000	277	8.9
	120	0	10000	280	17.0
	150	439	9561	279	23.5
0.3	100	4	9996	275	5.4
	120	0	10000	278	15.6
	150	0	10000	278	22.1
0.4	100	9	9991	278	7.4
	120	0	10000	280	14.5
	150	9	9991	279	22.4

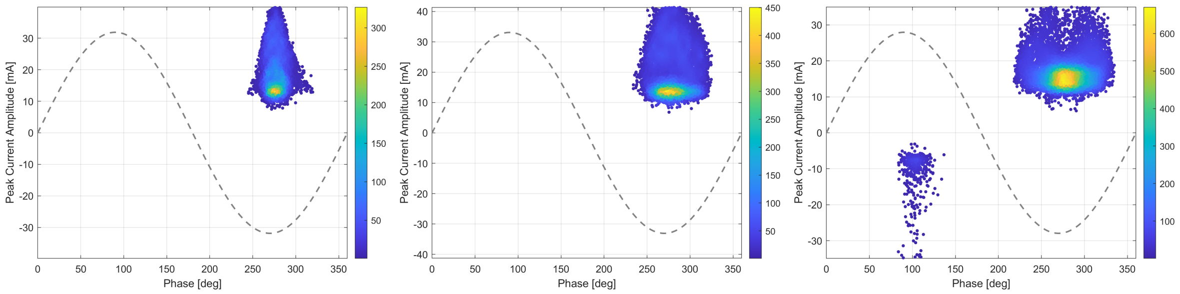

(a) (b) (c)

Figure 7.4: PRPD patterns for CO_2/O_2 mixture at 0.2 MPa, measured at a voltage of (a) 100%, (b) 120% and (c) 150% PDIV. Peak magnitude is the maximum pulse magnitude.

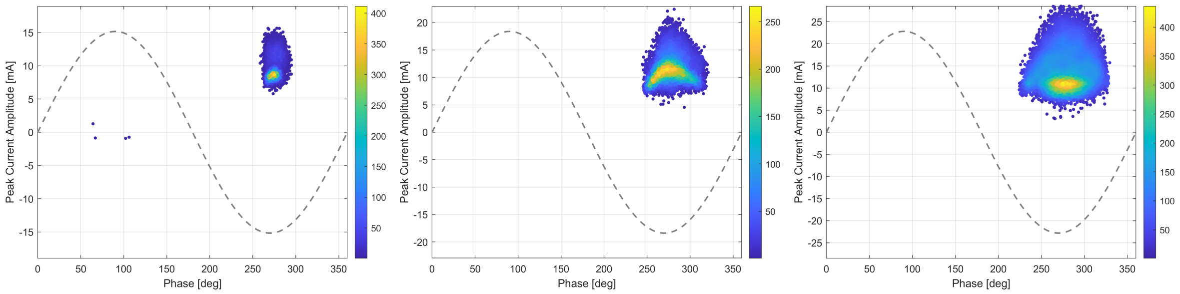

(a) (b) (c)

Figure 7.5: PRPD patterns for CO_2/O_2 mixture at 0.3 MPa, measured at a voltage of (a) 100%, (b) 120% and (c) 150% PDIV. Peak magnitude is the maximum pulse magnitude.

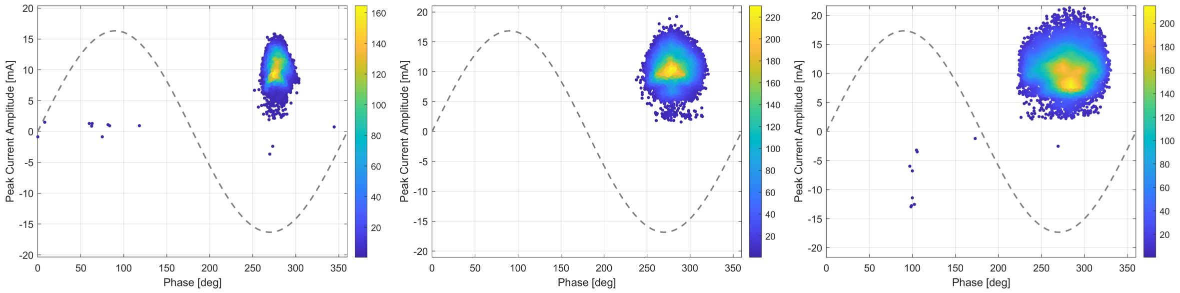

(a) (b) (c)

Figure 7.6: PRPD patterns for CO_2/O_2 mixture at 0.4 MPa, measured at a voltage of (a) 100%, (b) 120% and (c) 150% PDIV. Peak magnitude is the maximum pulse magnitude.

7.1.5. Apparent Charge Mean Magnitudes for the different methods

All waveforms processed as described in Section 6.2.6. The mean apparent charge values obtained from each estimation method are presented in Table 7.4. As the pressure increases, a decrease in magnitude is observed for all methods. The frequency domain method results in the highest mean charge magnitude, closely followed by the time integration method. The IEC quasi-integration method results in significantly lower values, less than half of those found using the other methods. PRPD patterns have been made for all of the charge estimation methods, and can be found in Appendix C.1.

Table 7.4: Mean charge magnitudes and the peak at various pressure levels and PDIV multiples

Pressure (MPa)	**PDIV** (%)	$\bar{q}_{\text{IEC}}$ (pC)	$\bar{q}_{\text{Time}}$ (pC)	$\bar{q}_{\text{Freq}}$ (pC)	$\bar{i}_{\text{peak}}$ (mA)
0.2	100	18.5	44.8	56.6	19.9
	120	19.0	46.0	58.1	20.7
	150	15.6	36.5	47.1	17.5
0.3	100	7.3	16.1	21.2	9.5
	120	8.7	19.7	25.6	11.5
	150	10.4	24.0	31.4	14.3
0.4	100	6.6	15.1	19.7	10.2
	120	6.8	15.6	20.3	10.5
	150	7.0	16.0	20.8	10.8

Correlation

Table 7.5 shows the correlation between charge estimation methods at different pressure and voltage levels with the peak amplitude of the current. The IEC and time method have a decent correlation at the 0.2 MPa measurements. For the measurements at higher pressures, the correlation is low, especially for the measurements at 1.0 PDIV. For the measurements where the voltages are increased, the correlation does increase. The frequency method has a strong correlation to the peak current amplitude at all measurements. The correlation between all methods, rather than only the peak current, can be found in Figure 7.7. Here it can be seen that the correlation between the time integration method and the IEC method is larger than their correlations to the peak current amplitude.

Table 7.5: Correlation between charge estimation methods at different pressure and voltage levels to the peak amplitude of the current

Pressure (MPa)	**PDIV** (%)	$r(i_{\text{peak}}, q_{\text{IEC}})$	$r(i_{\text{peak}}, q_{\text{Time}})$	$r(i_{\text{peak}}, q_{\text{Freq}})$
0.2	100	0.93	0.98	0.99
	120	0.96	0.99	0.99
	150	0.84	0.95	0.99
0.3	100	0.38	0.71	0.96
	120	0.54	0.83	0.98
	150	0.77	0.94	0.99
0.4	100	0.39	0.73	0.96
	120	0.46	0.79	0.98
	150	0.59	0.87	0.98

7.1.6. Time based analysis - Negative AC (180° - 360°)

To further investigate the results, the charge magnitude and phase angle of the PDs are evaluated for individual AC cycles (20 ms). This section focuses on PDs occurring during the negative half-cycle of the AC waveform (180° - 360°). Positive-cycle PD activity is treated separately in the following section, as it was only observed for the 0.2 MPa measurement at 150% PDIV.

Figure 7.8 shows the first AC cycle of the first measurement of the experiment, which is cycle 1 of 677 of the 0.2 MPa 100% PDIV measurement. Each line represents the occurrence of a single discharge. In Figure 7.8b the apparent charge value found with all three methods is marked with a different icon. The voltage of the AC wave was not measured but can be extrapolated from Table 7.1. The voltage maximum and minimum are marked with a dotted line to improve readability.

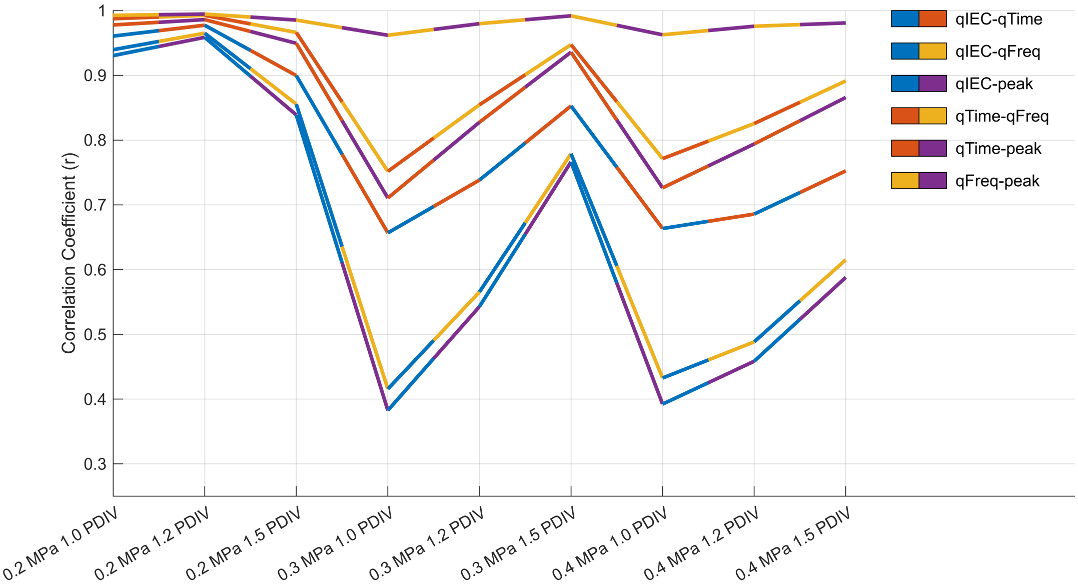

Figure 7.7: Cross correlation between all charge estimation methods and the peak current amplitude

The time it takes between PD events varies. In addition to the time between discharges decreasing as the voltage increases, an extra effect can be seen. Some discharges are quickly followed up by another discharge with a smaller magnitude. This effect is seen for all measurements, except for the 0.3 MPa 100% PDIV measurement.

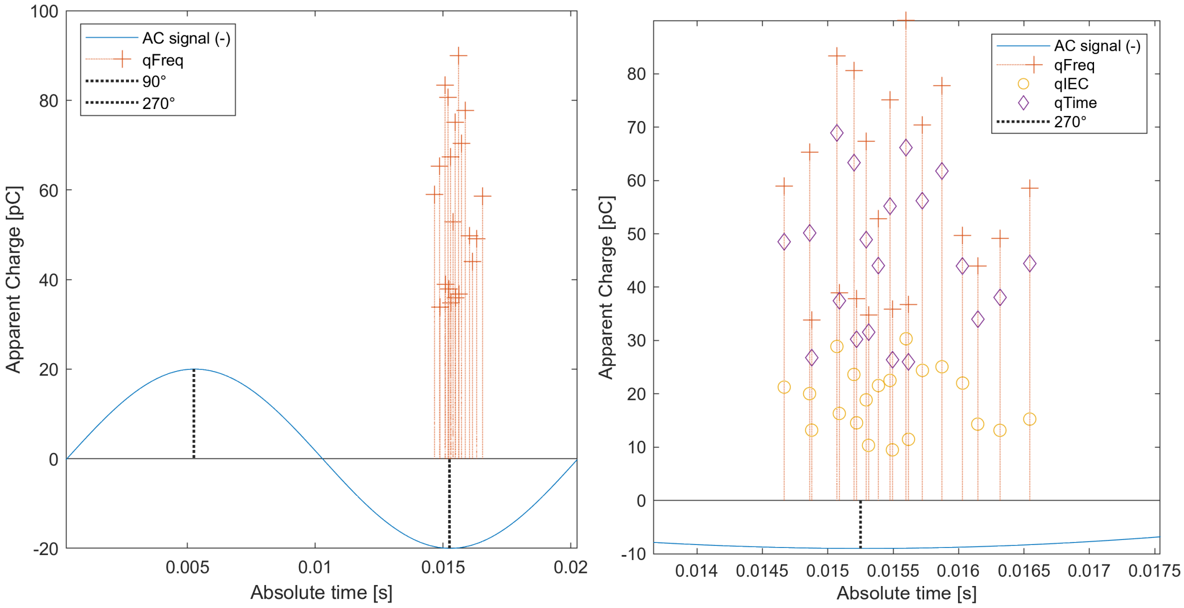

(a) AC cycle 1 (Full) only showing the charge magnitude only for the frequency method

(b) Zoomed version containing all Charge estimation methods

Figure 7.8: The PD events plotted in absolute time, for AC Cycle 1 (of 677) of the 0.2 MPa 1.0 PDIV measurement.

Figure 7.9 shows the first cycle of measurements at the same pressure of 0.2 MPa but for 120% PDIV and 150% PDIV, which shows an increase in the repetition rate. The development of the charge magnitude over voltage is different. In the measurement at 120% of PDIV the charge magnitude increases as the voltage increases, but this is not the case for the measurement at 150% PDIV.

Figure 7.10a shows the first cycle of the 0.3 MPa measurement at 1.00 PDIV. The PDs which quickly follow

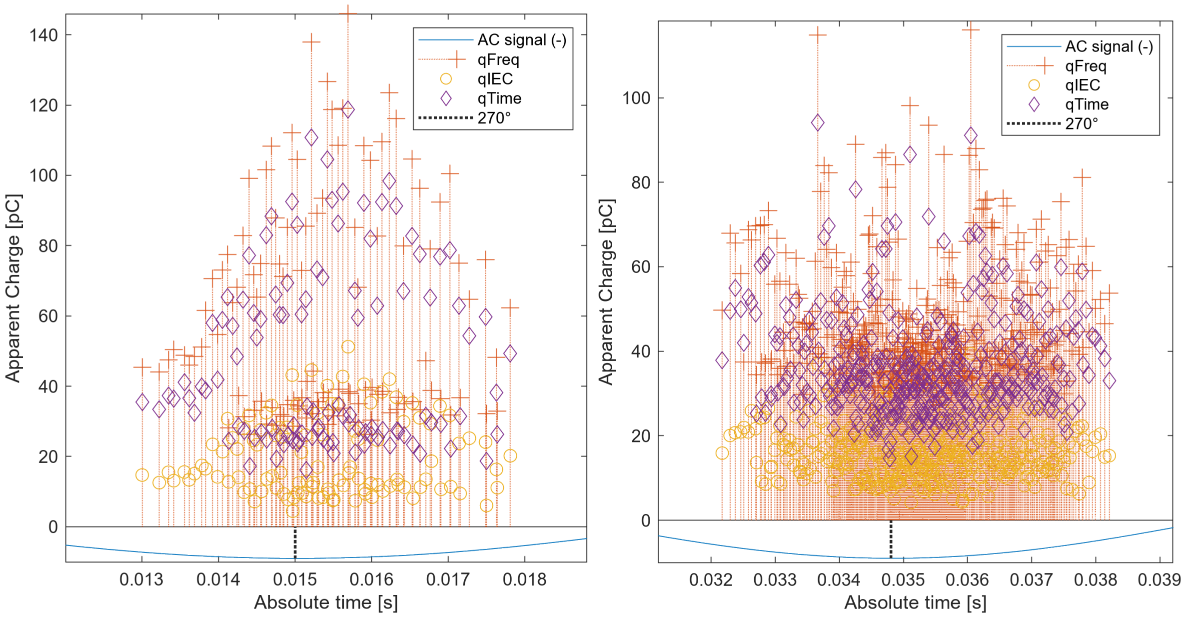

(a) AC cycle 1 (of 98) at 1.20 PDIV **(b)** AC cycle 2 (of 22) at 1.50 PDIV

Figure 7.9: The PDs plotted in absolute time, for AC Cycle 1 of the 0.2 MPa measurement at 1.2 PDIV & 1.5 PDIV.

up another PD can not be seen, but are again present at a higher voltage of 1.20 PDIV (Figure 7.10b).

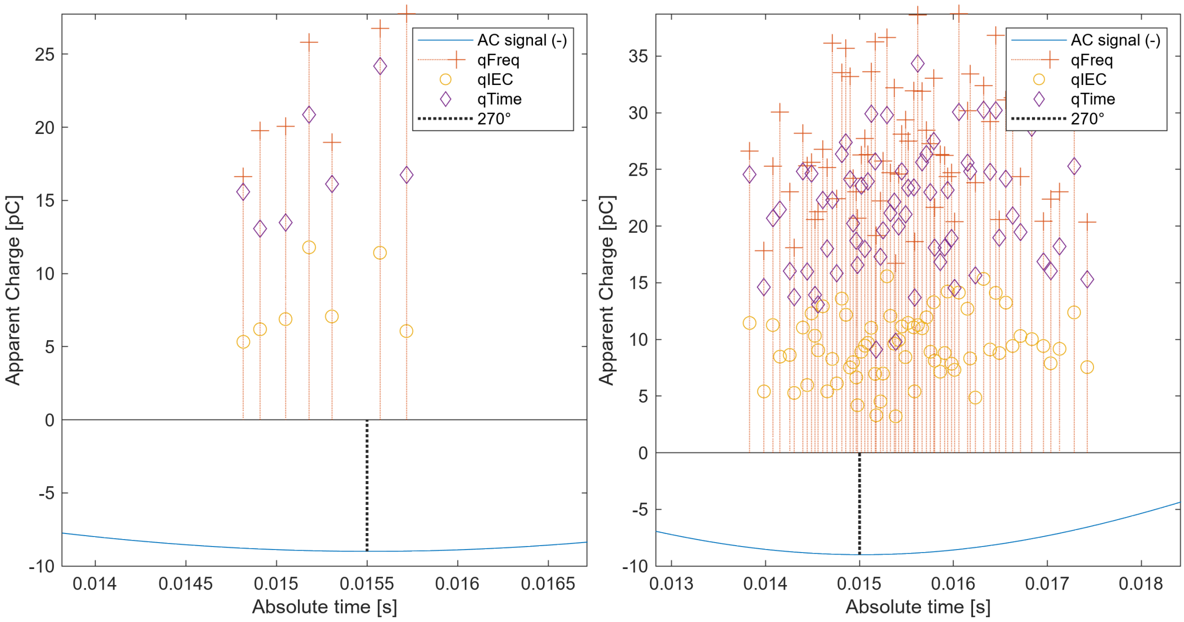

(a) AC cycle 1 (of 1400) at 1.00 PDIV **(b)** AC cycle 1 (of 136) at 1.20 PDIV

Figure 7.10: The PDs plotted in absolute time, for AC Cycle 1 of the 0.3 MPa measurement at 1.0 PDIV & 1.2 PDIV.

Histogram Δt

To further describe these discharges that quickly follow up another PD, the Δt between discharges in the negative cycle was calculated. Figures 7.11, 7.12 and 7.13 show the Δt of a measurement in histograms for the 0.2, 0.3 and 0.4 MPa measurement set respectively. Based on manual analysis a seperation between PDs quickly following up Table 7.6 displays the selection threshold for each measurement, and the count of PDs occurring above and below this threshold. As can be seen in Figure 7.11c, this separation becomes less clear as the pressure increases and the PDs follow each other up faster in

general. Which makes it hard Figures 7.14, 7.15 and 7.16 contain scatter plots showing the relation between Δt and the peak current amplitude for the 0.2, 0.3 and 0.4 MPa measurement set.
In Appendix C.2 the correlation between each method and between the peak current magnitude after seperation with this treshold can be found.

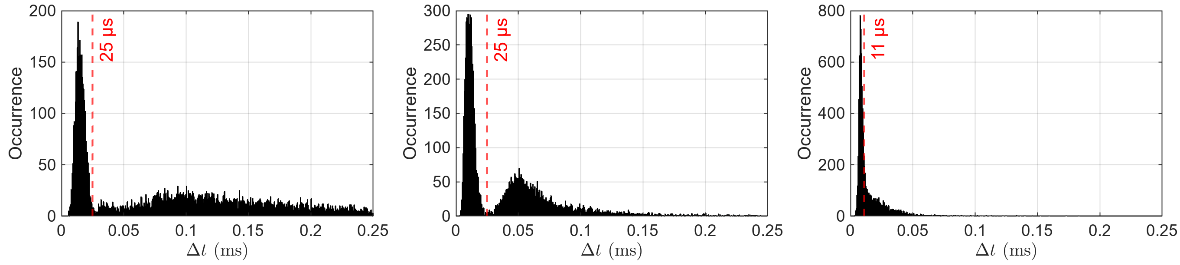

(a) (b) (c)

Figure 7.11: Histogram of the time interval (Δt) to the next partial discharge for the CO_2/O_2 (70%/30%) mixture at 0.2 MPa, evaluated at (a) 100%, (b) 120%, and (c) 150% of the PDIV.

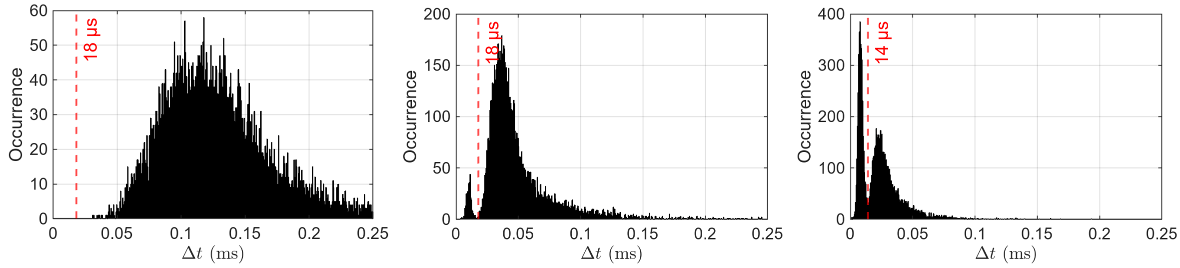

(a) (b) (c)

Figure 7.12: Histogram of the time interval to the next partial discharge for the CO_2/O_2 (70%/30%) mixture at 0.3 MPa, evaluated at (a) 100%, (b) 120%, and (c) 150% of the PDIV.

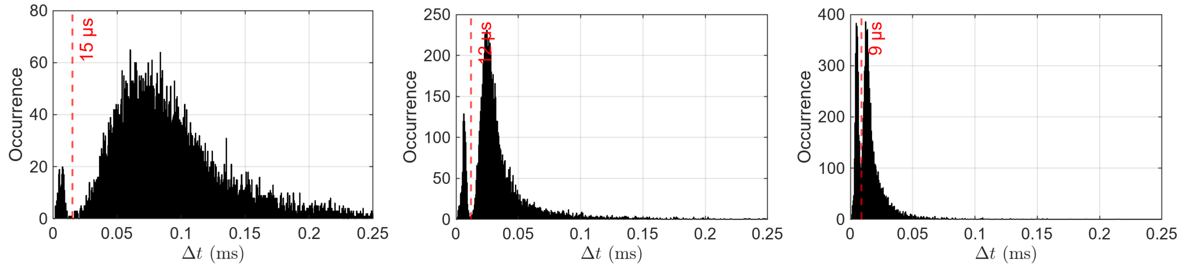

(a) (b) (c)

Figure 7.13: Histogram of the time interval to the next partial discharge for the CO_2/O_2 (70%/30%) mixture at 0.4 MPa, evaluated at (a) 100%, (b) 120%, and (c) 150% of the PDIV.

Table 7.6: Number of discharges above and below the selected Δt threshold per measurement condition

Pressure (MPa)	**PDIV (%)**	$\Delta t_{\text{threshold}}$ (μs)	Above	Below
0.20	100	25	6110	3213
	120	25	4761	5141
	150	11	3564	5201
0.30	100	18	8596	0
	120	18	9545	319
	150	14	6339	3618
0.40	100	15	9122	211
	120	12	8953	948
	150	9	7167	2783

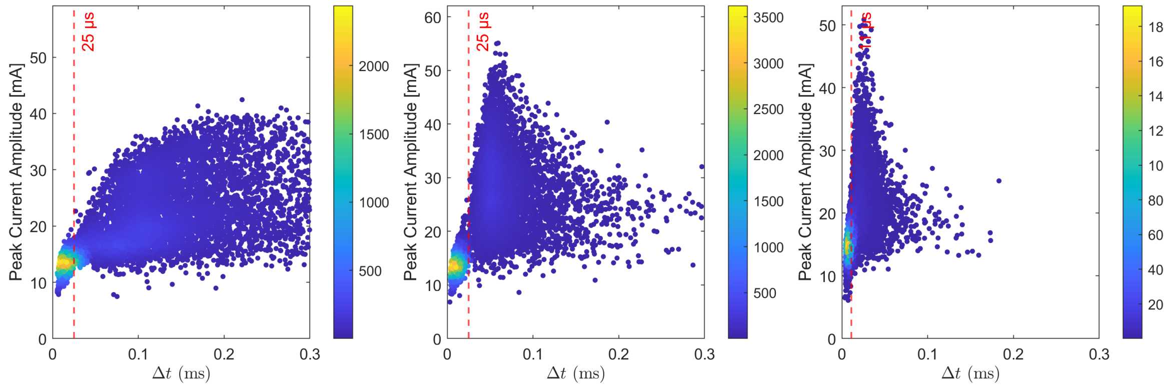

(a) (b) (c)

Figure 7.14: Peak Amplitude vs Δt for CO_2/O_2 mixture at 0.4 MPa, measured at PDIV of (a) 100%, (b) 120% and (c) 150%.

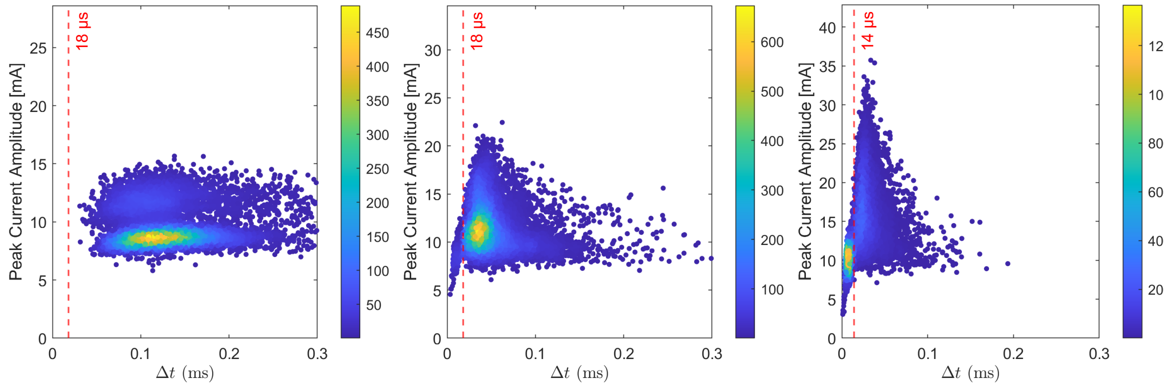

(a) (b) (c)

Figure 7.15: Peak Amplitude vs Δt for CO_2/O_2 mixture at 0.3 MPa, measured at PDIV of (a) 100%, (b) 120% and (c) 150%.

7.1.7. Time based analysis - Positive AC (0° - 180°)

This section performs the same time based analysis but for the positive part of the AC cyle. It only contains results for 0.2 MPa, 150% of PDIV which was the only measurement where multiple discharges were observed in the positive part. Figure 7.17a and Figure 7.17b show cycle 4 and 11. In both figures, a primary discharge is observed, followed by a series of additional discharges with lower apparent charge magnitudes.

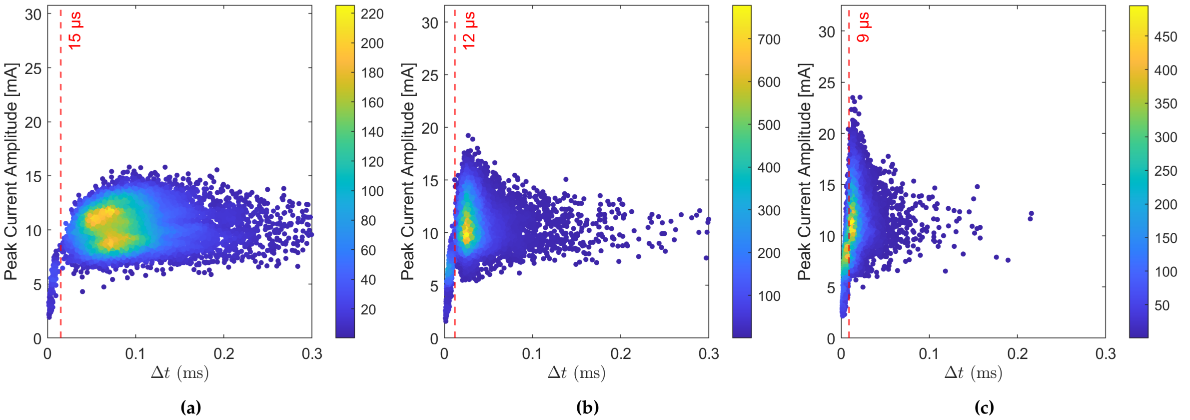

Figure 7.16: Peak Amplitude vs Δt for CO_2/O_2 mixture at 0.4 MPa, measured at PDIV of (a) 100%, (b) 120% and (c) 150%.

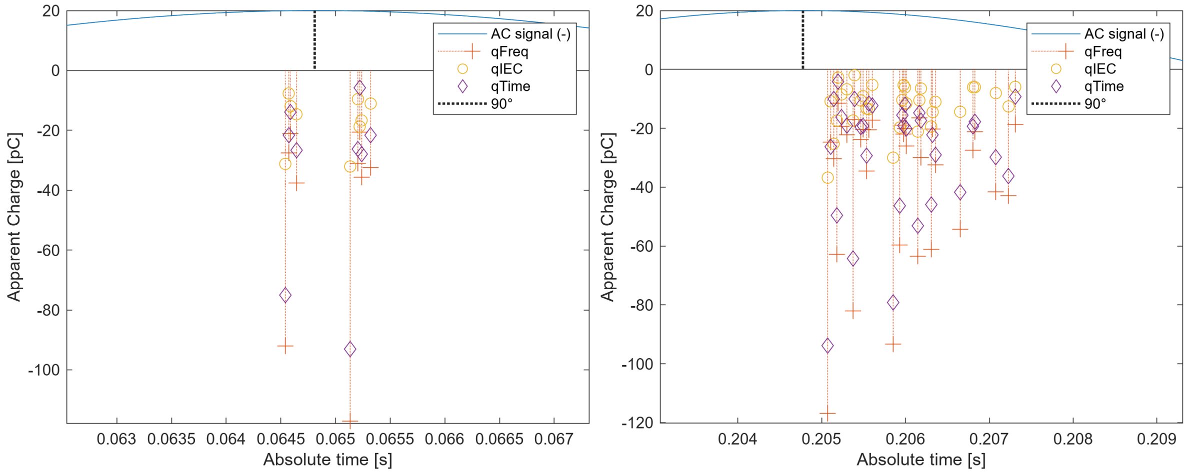

(a) AC Cycle 4 (0° - 180°)

(b) AC Cycle 11 (0° - 180°)

Figure 7.17: 0.2 MPa, 150% of PDIV, Positive PDs plotted

8

Discussion

8.1. Results CO_2/O_2 (70%/30%)

Several observations align with known behaviour of HV-side corona discharges in other gases. As expected, the PDIV increases with rising pressure, while the apparent charge magnitude decreases. Additionally, higher applied voltages result in increased repetition rates. Negative PDs occur earlier in the AC cycle than positive ones, and their distribution broadens over a larger phase window as the voltage increases.
What can additionally be seen, is that the PD magnitude is voltage related, which is especially pronounced for the 0.2 MPa measurements.
In Section 7.1.6, which describes the time-based analysis of PDs occurring in the negative AC cycle, the time between discharges after each other varies wildly. Some discharges are followed up within microseconds by another discharge with a lower magnitude. This effect is seen for all measurements, except for the 0.3 MPa 100% PDIV measurement. The time to this next discharge decreases with pressure and voltage, which suggest a physical phenomenon.
This effect has not been reported in existing literature and warrants further investigation. A logical first step would be to repeat the measurements in a well-characterised reference gas to confirm that the observation is not an artefact of the measurement setup.
The addition of O_2 does have an impact on the effective ionisation coefficient (Figure 2.2, which could be a basis for an explanation of the effect. Figure 8.1 shows the impact of varying the O_2 content in a C_4FN mixture, and it can be seen that even small changes in composition lead to differences in the PRPD patterns.

No measurable differences were observed in the frequency spectrum. This result is however constrained by the bandwidth limitations of the measurement circuit. (Section 8.2)

8.2. Evaluation of measurement circuit

No significant change in rise times was observed between any of the measurements, although the rise time is expected to decrease at higher pressures. The rise time is limited by the measurement circuit. The measurement results of all PDs have a peak at the oscillation frequency of the measurement circuit, and the signals frequency components after 165 MHz are negligible. This is probably a result of the transmission parameter of the OV protection, which was found in Section 5.3.1 to have a transfer characteristic with a -3db cut-off frequency at 148 MHz.
The repetitive excitations that followed the main pulse which could be seen in Figures 7.2 are most likely a reflection. The excitations repeat every 13 ns, assuming a signal propagation velocity of $0.7 \cdot c$, this corresponds to a distance of approximately 2.73 m. As this length closely matches twice the length of the coaxial cable (1.5 m) connecting the oscilloscope to the protection devices, this suggests these excitations are due to a reflection of the signal occurring between these devices.

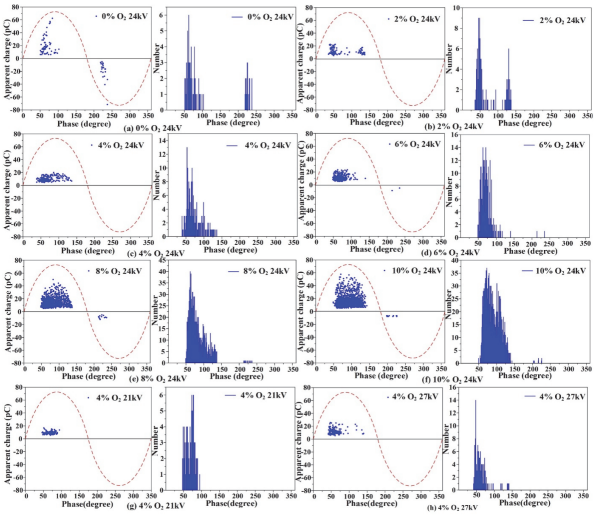

Figure 8.1: PRPDs of a C4FN mixture in which the O_2 content is varied [14]

8.3. Charge Estimation Methods

The results in Section 7.1.5 show that the frequency domain method results in the highest mean charge magnitude, closely followed by the time integration method. The IEC quasi-integration method results in significantly lower values, less than half of those found using the other methods. This suggests that the charge is underestimated for the IEC method.

This could be explained through the fact that the calibration pulse has a much slower risetime than the actual PDs. The integration of noise, which resulted in a lower calibration factor in Section 6.2.3 might be less of an issue for the PDs which have a much larger peak current magnitude.

As a result of the slower risetime, the frequency content of the calibration pulse is also more present in the lower frequencies than for the PDs. As a result, the calibration pulse does not accurately represent the PD during quasi-integration, which happens in the frequency range of 500 to 800 kHz. This results in an overestimation of the calibration signal compared to the PDs, again resulting in a lower calibration factor.

8.3.1. Usage of the Pearson correlation coefficient to evaluate the results

The Pearson correlation coefficient is used to evaluate the consistency between the charge estimation methods and the peak current amplitude value. It would seem logical that these value should be related, especially for unipolar pulses as the charge is related to the current, and from the values logical conclusions can be derived. However, no literature was found employing a similar correlation-based evaluation, so a strong correlation is can not be assumed direct evidence of a good charge estimation method.

8.3.2. Magnitude dependent correlation

In general, the larger the charge magnitude, the higher the correlation. This can be explained through the fact that the noise influences the charge estimation methods. Especially for the IEC method, this results in a very poor correlation at higher pressures. This does not explain why the 1.0 PDIV measurement at 0.3 & 0.4 MPa have a very poor correlation, which improves as the voltage is increased.

Another contributing factor to the poor performance of the IEC method is the limited overlap between the HFCT bandwidth, which declines sharply below 1 MHz and the bandpass filter. As a result, the signal is poorly distinguishable from noise, increasing the influence of noise on the charge estimation. A possible solution to improve the signal strength in the portion that is quasi-integrated is to move the bandpass filter bandwidth to a region above 1 MHz, but this would not be in accordance to IEC 60270. The adapted version of the frequency method has a very strong correlation and seems less impacted by noise than the other methods.

8.3.3. IEC Calibration

As mentioned above, the IEC estimation method not only performs poorly for smaller charge magnitudes, but the charge magnitude in general is underestimated. Found in Section 4.5.2 was already that the current setup does not adhere to the IEC 60270 requirement that the capacitance of the calibrator is larger than $0.1 \cdot C_a$. As a result, sufficient charge transfer cannot be guaranteed. That the calibration pulse is not representative of the actual PD can also be confirmed through the fact that the smallest calibration charge that could be measured was 50 pC, while the charge magnitude results of the measurements are significantly smaller.

Figure 8.2 shows a calibration method proposed by IEC 60270 that would make it possible to achieve a calibration capacitance that adheres to the requirements.

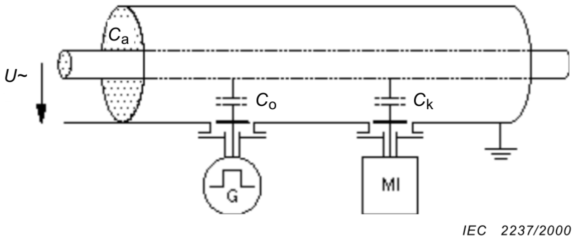

Components

$U_{\sim}$	high-voltage supply
MI	measuring instrument
C_a	test object
C_k	coupling capacitor
C_o	calibration capacitor
G	step voltage generator

Figure 8.2: Test circuit for measurement in GIS [17]

8.4. Recommendations future experiments

8.4.1. Definition of PDIV

It is difficult to describe a rate of rising voltage, as when it seems that PDIV has been reached, the PDs can stop again. Then the voltage has to be increased again and the rate of increase is no longer adhered to. As a result, it would seem that the PDIV of the 0.3 MPa measurement has been estimated at a relatively lower voltage (Table 7.1) than the 0.2 & 0.4 MPa measurements. This assumption is based on the lower repetition rate, the absence of PDs in the positive cycle at 1.5 PDIV and an absence of the follow up PD effect until the voltage is increased. For a mixture with a slightly different ratio but for the same field utilization factor the PDIV was also found to be linear (Figure 3.2).

This underestimation of the PDIV complicates a fair evaluation of measurement results at different pressure levels. An improved definition of the inception voltage than "voltage at which repetitive discharges are observed" could be the definition proposed by IEC 61934 [30]:

- **PDIV** is the impulse voltage when the first PD pulse is detected.
- **RPDIV** is the minimum impulse voltage when a mean of five PD pulses occurs on ten voltage impulses of the same polarity. When fewer than ten impulses are tested at the same voltage, the ratio of PD pulses to voltage impulses can be used.
- After maximum voltage, the repetitive impulses fall with a decreased voltage step.
- **RPDEV** is the maximum voltage at which a mean of five PD pulses occurs on ten voltage impulses of the same polarity.
- **PDEV** is the impulse voltage when no PD pulse is detected.

For these AC measurements, the repetitive PDIV would be reached when PDs occur in half of the AC waves. This value would be lower than the PDIV values found in this experiment, where PDs occur in every AC cycle, even for the 0.3 MPa measurement at PDIV.

This would not solve another issue with the determination of the PDIV that was experienced, which is that after a period of consistent PDs the PDs would cease occurring and the voltage would have to be increased before achieving repetitive discharges again. Some sources, such as [39] use a UV light source to make that this variation is not a result of lacking starting electrons.

8.4.2. Improving Bandwidth & Sensitivity

The upper bandwidth is not constrained by the HFCT itself but by the overvoltage protection device. If this limitation were addressed, the next bandwidth-limiting factors would be the signal decay of the RS coaxial surge protector and the coax connections themselves. The lower bandwidth limit, which as discussed in Section 8.3 could impact the charge estimation, could be lowered by selecting a different HFCT.

As the design of an HFCT is a trade-off primarily dominated by the number of turns for a HFCT of given dimensions, the sensitivity could be improved by accepting a lower value for the upper bandwidth. In this measurement circuit, where the upper bandwidth is not constrained by the HFCT, increasing the number of turns would enhance sensitivity without compromising bandwidth.

8.4.3. Needle Degradation

During the experiments, a number of breakdowns occurred. Even though the discharge power is limited through the use of the resistor, the needle still degrades. [5] recommends that laboratories should report an estimate on the energy deposited for each breakdown to quantify this degradation, especially when performing breakdown tests. [4] performed test in a setup with a similar field utilization factor of 4%, and found that the negative inception voltage is greatly impacted even after 1 arc.

9

Conclusion & Recommendations

9.1. Conclusion

This work presents the development and application of a high-bandwidth measurement circuit designed to enable detailed characterization of PDs in alternative insulation gases under AC voltage stress. Designed was an experimental compartment for charge-based measurements which includes an electrode configuration to create corona discharges and uses a high-frequency current transformer as a measurement impedance.

Initial measurements using a conventional IEC 60270 configuration revealed a resonance frequency of 3.5 MHz, limiting the effective bandwidth of the measurement system. To address this, the internal capacitance of the setup was analysed using both measurements and FEM simulation. Based on this evaluation, the traditional external coupling capacitor was removed, and the inherent capacitance between the conductor in the bushing and the GIS enclosure was used as a coupling capacitor. By using the bushing as a coupling capacitor, the resonance frequency of the measurement circuit was shifted from 3.5 MHz to 144 MHz, significantly increasing bandwidth while improving sensitivity. To further reduce the impact of resonance and suppress signal distortion, a damping resistor block was implemented.

The transmission parameters for each section of the measurement circuit were characterised using a Vector Network Analyser, enabling quantification of the transfer function and the derivation of the current from the measured voltage signal. This made it possible to apply charge estimation methods directly without relying on a calibration factor, as required in the IEC 60270 method.

The setup was applied to study corona discharges in a CO_2/O_2 (70%/30%) mixture under various pressures and voltage levels. Across the measurements, a novel voltage-related PRPD pattern was observed that is not reported in existing literature. Multiple charge estimation methods were applied and compared to the peak current magnitude to assess their consistency. A modified version of the frequency domain method showed the highest correlation across all conditions, including at lower charge magnitude levels, indicating that it is the most robust approach for use in this measurement circuit.

Overall, the thesis objectives have been met: the measurement circuit enables detailed PD characterisation in alternative gases, and the CO_2/O_2 mixture was successfully evaluated, providing new insights into its discharge behaviour which require further investigation.

9.2. Recommendations

Further investigation into the partial discharges that occur in rapid succession within the CO_2/O_2 mixture (Section 8.1) should begin with repeating the experiments using a gas mixture with well-characterised behaviour. This ensures that the observed phenomenon is not an artefact of the measurement setup.
Once this is confirmed, a series of tests can be performed in which the O_2 concentration in a CO_2 mixture is systematically increased. This would allow identification of the threshold at which the phenomenon of these closely spaced PD pulses begins to appear.
Recommendations regarding the measurement circuit are elaborated on in the discussion. (Section 8.4.2. Improvements are possible, but it should be considered what the effect of these improvments would be on the evaluation of the characterisation in alternative gases.

References

[1] E. A. Ray, F. L. Moore, J. W. Elkins, *et al.*, “Quantification of the SF6 lifetime based on mesospheric loss measured in the stratospheric polar vortex,” *Journal of Geophysical Research*, vol. 122, no. 8, pp. 4626–4638, 2017. doi: `10.1002/2016JD026198`.

[2] T. Uchii, A. Majima, T. IIjima, T. Inoue, and T. Yasuoka, “High-Voltage Switchgear Technology Applying CO2/O2 Natural-Origin Gas Mixture as an Alternative Insulating and Interrupting Medium to SF 6,” CIGRE, Tech. Rep., 2023.

[3] S. Kumar, T. Huiskamp, A. J. M. Pemen, M. Seeger, J. Pachin, and C. Franck, “Electrical Breakdown Study in CO2 and CO2-O2 Mixtures in AC, DC and Pulsed Electric Fields at 0.1-1 MPa Pressure,” *IEEE Trans. Dielectr. Electr. Insul.*, vol. 28, no. 1, pp. 158–166, Feb. 2021. doi: `10.1109/TDEI.2020.009115`.

[4] H. E. Nechmi, M. Michelarakis, A. Haddad, and G. Wilson, “Clarifications on the behavior of alternative gases to sf6 in divergent electric field distributions under ac voltage,” *Energies*, vol. 14, no. 4, Feb. 2021. doi: `10.3390/en14041065`.

[5] CIGRE WG D1.67, “TB 849 - Electric performance of new non-SF6 gases and gas mixtures for gas-insulated systems,” Tech. Rep., 2021.

[6] A. Küchler, *High Voltage Engineering Fundamentals · Technology · Applications*. 2017.

[7] European Union, *Regulation (EU) 2024/573 of the European Parliament and of the Council of 7 February 2024 on fluorinated greenhouse gases*, `http://data.europa.eu/eli/reg/2024/573/oj`, Feb. 2024.

[8] M. Rabie and C. M. Franck, “Assessment of Eco-friendly Gases for Electrical Insulation to Replace the Most Potent Industrial Greenhouse Gas SF6,” *Environmental Science and Technology*, vol. 52, no. 2, pp. 369–380, Jan. 2018. doi: `10.1021/ACS.EST.7B03465`.

[9] I. P. o. C. C. (IPCC), “Climate Change 2021 – The Physical Science Basis: Working Group I Contribution to the Sixth Assessment Report of the Intergovernmental Panel on Climate Change,” *Climate Change 2021 – The Physical Science Basis*, Jul. 2023. doi: `10.1017/9781009157896`.

[10] M. Perret, T. Berteloot, Y. Kieffel, and A. Ficheux, “C4-FN MIXTURES FOR HIGH-VOLTAGE EQUIPMENT,” GE Vernova & Hitachi Energy, Tech. Rep.

[11] 3M Company, *3M™ Novec™ 4710 Insulating Gas – Technical Data Sheet*, Dec. 2022.

[12] W. M. Haynes, Ed., *CRC Handbook of Chemistry and Physics*, 93rd. Boca Raton: CRC Press, 2012, pp. 6–221, Accessed via TU Delft library. doi: `10.1201/b12286`.

[13] M. S. Dincer, S. S. Tezcan, H. Duzkaya, and S. Dincer, “Synergism analysis in dielectric strength of CO2+N2+O2 ternary mixtures,” *Alexandria Engineering Journal*, vol. 61, no. 5, pp. 3747–3756, May 2022. doi: `10.1016/J.AEJ.2021.08.080`.

[14] F. Ye, X. Zhang, Y. Li, *et al.*, “Effect of O2 on AC Partial Discharge and Decomposition Behavior of C4F7N/CO2/O2Gas Mixture,” *IEEE Transactions on Dielectrics and Electrical Insulation*, vol. 28, no. 4, pp. 1440–1448, Aug. 2021. doi: `10.1109/TDEI.2021.009626`.

[15] B. Zhang, Y. Yao, M. Hao, X. Li, J. Xiong, and A. B. Murphy, “Study of the dielectric breakdown strength of CO2–O2 mixtures by considering ion kinetics in a spatial–temporal growth avalanche model,” *J. Appl. Phys*, vol. 132, p. 93 302, 2022. doi: `10.1063/5.0093568`.

[16] Z. Wu, Z. Qiaogen, J. Ma, and L. Pang, “A phase synchronization photography method for AC discharge,” *Review of Scientific Instruments*, vol. 89, p. 56 107, May 2018. doi: `10.1063/1.5031080`.

[17] IEC, “IEC 60270 High-Voltage test techniques: Partial discharge measurements,” p. 117, 2000.

[18] G. Stone, “Importance of bandwidth in PD measurement in operating motors and generators,” *IEEE Transactions on Dielectrics and Electrical Insulation*, vol. 7, no. 1, pp. 6–11, 2000. doi: `10.1109/94.839335`.

[19] G. C. Stone, A. Cavallini, G. Behrmann, and C. A. Serafino, *Practical Partial Discharge Measurement on Electrical Equipment*. Hoboken, NJ, USA: Wiley, Aug. 2023. DOI: 10.1002/9781119833345.

[20] A. J. Reid and M. D. Judd, "Ultra-wide bandwidth measurement of partial discharge current pulses in SF6," *Journal of Physics D: Applied Physics*, vol. 45, no. 16, p. 165 203, Apr. 2012. DOI: 10.1088/0022-3727/45/16/165203.

[21] H. Hama, J. S. Okabe, J. R. Bühler, *et al.*, "TB 730 - DRY AIR, N2 , CO2 AND N2/SF6 MIXTURES FOR GAS-INSULATED SYSTEMS," 2018.

[22] *IEC 60270: High-voltage test techniques – Partial discharge measurements*, Geneva, Switzerland: International Electrotechnical Commission, 2000.

[23] IEC, "IEC 62478 test techniques - Measurement of partial discharges by electromagnetic and acoustic means,"

[24] F. H. Kreuger, *Industrial High Voltage: [Vol. 2.], 4.Coordinating, 5.Measuring, 6.Testing*. Delft University Press, 1992.

[25] F. H. Kreuger, *Partial discharge detection in high-voltage equipment*. London: Butterworths, 1989.

[26] *IEC 60270: High-voltage test techniques – Charge-based measurement of partial discharges*, Geneva, Switzerland: International Electrotechnical Commission, 2025.

[27] Fischer Custom Communications, Inc., *Current probe catalog*, Available from: https://accelonix.nl/wp-content/uploads/FCC-Current-Probe-Overview.pdf.

[28] A. Rodrigo-Mor, F. A. Muñoz, and L. C. Castro-Heredia, "Principles of Charge Estimation Methods Using High-Frequency Current Transformer Sensors in Partial Discharge Measurements," *Sensors 2020, Vol. 20, Page 2520*, vol. 20, no. 9, p. 2520, Apr. 2020. DOI: 10.3390/S20092520.

[29] J. V. Kluss, A. P. Elg, and C. Wingqvist, "High-Frequency Current Transformer Design and Implementation Considerations for Wideband Partial Discharge Applications," *IEEE Transactions on Instrumentation and Measurement*, vol. 70, 2021. DOI: 10.1109/TIM.2021.3052002.

[30] IEC, "IEC 61934 Electrical measurement of partial discharges (PD) under short rise time and repetitive voltage impulses," 2024.

[31] A. R. Mor, L. C. C. Heredia, and F. A. Muñoz, "Estimation of charge, energy and polarity of noisy partial discharge pulses," *IEEE Transactions on Dielectrics and Electrical Insulation*, vol. 24, no. 4, pp. 2511–2521, 2017. DOI: 10.1109/TDEI.2017.006381.

[32] K. K. Murty, "Fundamentals of condenser bushings," *Transformers Magazine*, vol. Special Edition, no. Bushings, 2017.

[33] C. R. Paul, *Inductance: Loop and Partial*. Wiley, Dec. 2009. DOI: 10.1002/9780470561232.

[34] L. C. C. Heredia and A. R. Mor, "Effects of RLC Parameters of a Measuring Circuit on the Frequency Spectrum of Partial Discharges," in *2018 IEEE Electrical Insulation Conference (EIC)*, 2018, pp. 196–199. DOI: 10.1109/EIC.2018.8481131.

[35] Mraz P., Eckert M., and Hammer U., "TD-118 PD measurement above 1 MHz - limitations, challenges, solutions," Haefely AG, Basel, Switzerland, Tech. Rep., 2023.

[36] A. Cavallini, G. C. Montanari, and M. Tozzi, "PD apparent charge estimation and calibration: A critical review," *IEEE Transactions on Dielectrics and Electrical Insulation*, vol. 17, no. 1, pp. 198–205, 2010. DOI: 10.1109/TDEI.2010.5412018.

[37] A. Rodrigo Mor, L. C. Castro Heredia, D. A. Harmsen, and F. A. Muñoz, "A new design of a test platform for testing multiple partial discharge sources," *International Journal of Electrical Power & Energy Systems*, vol. 94, pp. 374–384, Jan. 2018. DOI: 10.1016/J.IJEPES.2017.07.013.

[38] FEMTO Messtechnik GmbH, *HCA-400M-5K-C High Speed Current Amplifier Datasheet*, https://www.femto.de/images/pdf-dokumente/de-hca-400m-5k-c.pdf, Berlin, Germany, Mar. 2019.

[39] B. Korthauer, O. Šefl, C. M. Franck, and J. Biela, "Partial discharge inception voltage modeling in air gaps at low to atmospheric pressure," *Journal of Physics D: Applied Physics*, vol. 58, no. 23, Jun. 2025. DOI: 10.1088/1361-6463/add6b1.

A

FEM Simulation

This appendix describes the finite element simulations performed to support the design and analysis of the measurement setup. The simulations were carried out using the *Electrostatics* physics module in COMSOL Multiphysics.

Two studies were conducted:

- **Study 1: Stationary (Parametric)** Used to evaluate the electric field distribution in the electrode arrangement under varying geometric parameters. The geometry is parametrized to evaluate the effect of changes in electrode configuration on the electric field distribution.
- **Study 2: Stationary Source Sweep** Used to determine the Maxwell capacitance matrix and perform separation of internal capacitances.

Both studies were based on a 2D axisymmetric model for which the geometry, material settings, parameter sweeps, and simulation methodology are outlined below.

A.1. Geometry

The model was constructed using a 2D axisymmetric approach due to the (mostly) rotational symmetry of the setup. This reduces the required processing time, but was primarily chosen as this significantly reduces the time required for modelling.
Figure A.1 shows the model as well as the actual test compartment. The oval shape of the compartment is approximated with a sphere. The geometry of the capacitively graded foil is fictitious and is only implemented to confirm the impact of capacitive grading on the electric field distribution.
As there is a large difference in scale between the needle and the rest of the compartment, the mesh generation is set to extremely fine. The standard meshing functionality decreases geometry and simulation detail too much in the region of interest, which is near the needle tip. Since the field distribution of the COMSOL model outside of the compartment does not represent the actual distribution, the simulation space of the air outside the compartment is reduced to improve detail in the compartment.

A.1.1. Materials

The bushing is modelled with a relative permittivity of $\varepsilon_r = 4$, while all other regions in the domain simulated are defined as air. The electric field distribution does not change for other gases, as the relative permittivity (ϵ_r) at 20 ° C can be assumed 1.00. Only after the 4th significant digit does the permittivity start to differ [12] for the gases of interest.

A.1.2. Evaluating different electrode configurations

As the geometry is fully parametrized, changes in electrode geometry such as gap distance, tip radius and protrusion length can easily be varied. By setting `enable_TB849_electrode` to 0, a new electrode geometry can easily be constructed and evaluated too.

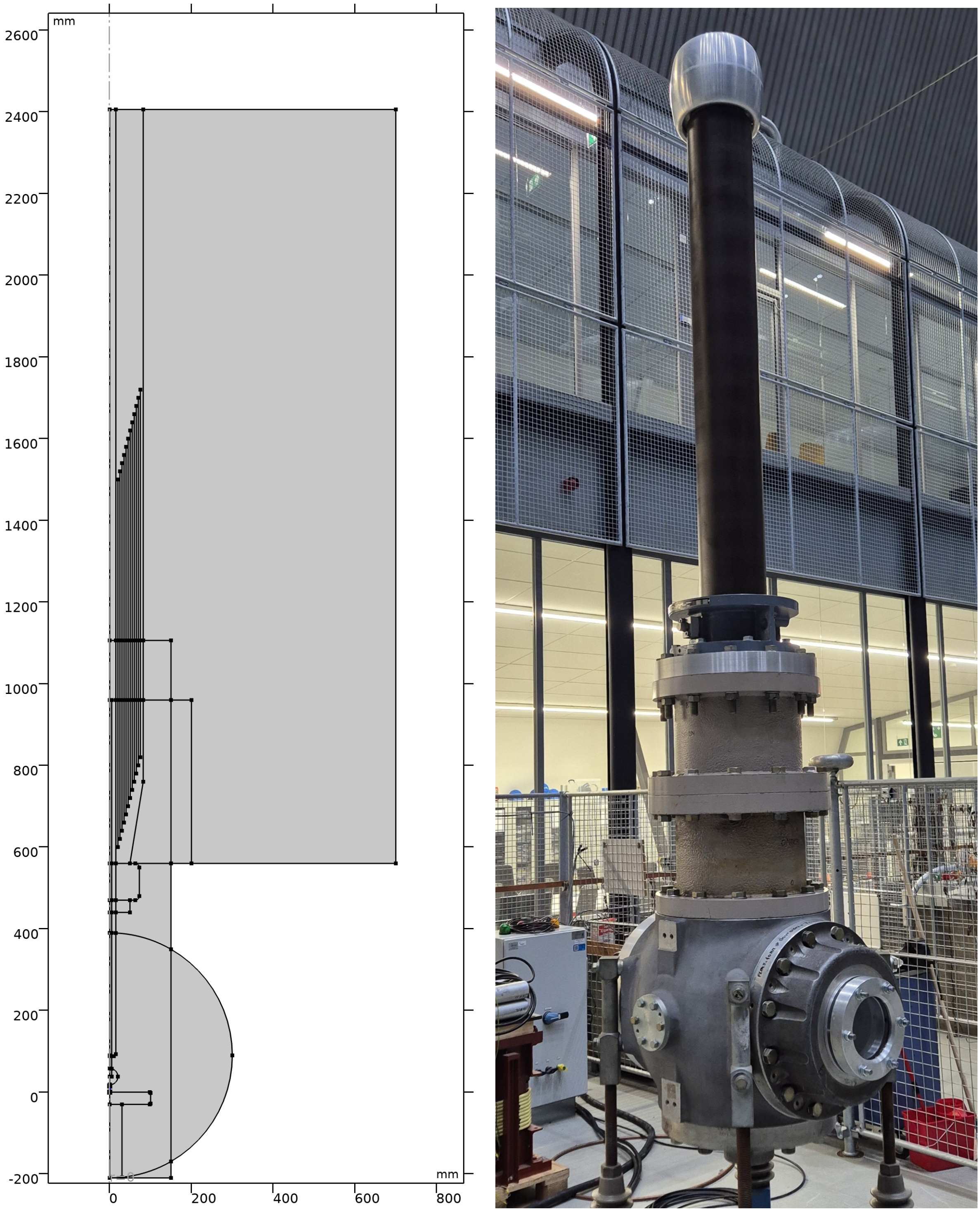

(a) The 2D axisymmetric **(b)** A picture of the test compartment

Figure A.1: Comparison between the model geometry and the actual test compartment. The oval shape of the compartment is approximated with a sphere. The geometry of the capacitively graded foil is fictitious, and is only implemented to confirm the impact of capacitive grading on the electric field distribution.

A.2. Study 1: Stationary (Parametric):

This study was used to evaluate the electric field distribution at the needle tip for different geometry parameters to evaluate the effect on the field utilization factor. A potential of 1 kV was applied to the HV terminal which includes the electrode configuration.

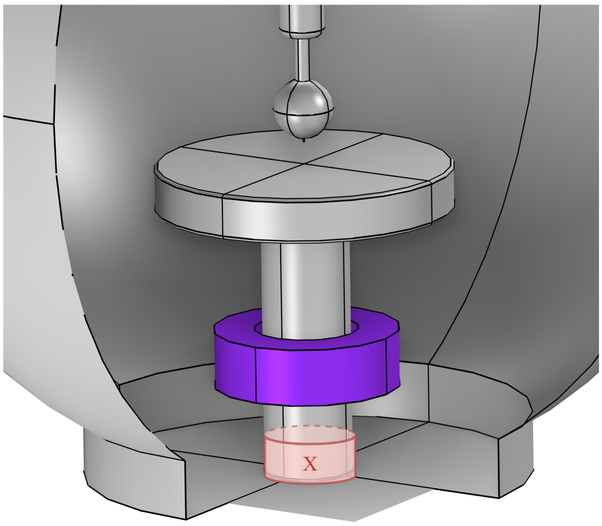

Figure A.2: A 3D representation of the cut in the geometry to be able to assign a terminal to the ground plane. The HFCT, which is shown in purple is not simulated.

A parametric sweep was performed on two parameters: the radius of the needle tip and the inclusion of a smoothing sphere. The sweep settings are listed in Table A.1.

Table A.1: Parametric Sweep Settings

Parameter Name	Parameter Value List	Parameter Unit
tip_radius	0.05, 0.1, 0.125, 0.15, 0.2, 0.25, 0.3	mm
smoothing_sphere_enable	0, 1	–

A.3. Study 2: Source Sweep

To perform the separation of C_{a1} and C_{a2} through evaluation of the Maxwell capacitance matrix $\mathbf{C}$ after modification of the geometry, the source sweep method is used with some changes in the model.
Figure A.2 shows a 3D representation of the cut in the geometry used to isolate the ground plane and rod from the grounded compartment. The separated geometry is assigned a terminal, which allows for decomposing the capacitance using a source sweep. During the source sweep, simulations are performed while 1 V is applied to a terminal while all other terminals are grounded. As there are only two terminals in this simulation, two simulations are run before the simulation is finished. From the results a Maxwell capacitance matrix can be constructed. In this matrix, each column corresponds to the charge response when one terminal is excited while all others are grounded. The diagonal elements represent self-capacitance, while the other terms are mutual coupling between terminals.
A more in-depth explanation including illustrations can be found in this blog by COMSOL about using the source sweep method to construct the Maxwell capacitance matrix.

In this matrix, each column corresponds to the charge response when one terminal is excited while all others are grounded.

Table A.2: Geometry Parameters for TB849 Strongly Non-uniform Configuration

Name	**Expression**	**Value**
enable_TB849_electrode	1	1
r_smoothing_sphere	20 [mm]	0.02 m
r_needle	0.5 [mm]	5E-4 m
protrusion_length	3 [mm]	3 mm
tip_radius	0.3 [mm]	3E-4 m
tan15deg	0.268	0.268
tip_transition_length_tot	r_needle / tan15deg	1.8657 mm
tip_transition_length_correction	tip_radius / tan15deg	1.1194 mm
tip_transition	tip_transition_length_tot - tip_transition_length_correction	7.4627E-4 m
smoothing_sphere_enable	1	1

B

Code Signal Processing

Most of the MATLAB code used to perform the processing steps can be downloaded from the Gitlab project page of the HVsoftware project. The project currently is an internal tool, but access to the project page can be requested, which is also possible for those not employed by the TU Delft.
Contained are a general framework for evaluating PD measurements based on HFCT measurements, which includes the methods used to derive the PD Parameters. Specific code relating to these measurements, such as sorting, plotting and statistical analysis and the data itself is not included in the codebase. Therefore these things have been placed on a Personal Gitlab page. Access can be requested through the same channels as for the HVsoftware project.

B.1. Loop Inductance

Listing B.1: Calculation of loop inductance for a nonsimplified rectangular geometry [33]

```
function L_loop = nonsimplified_rectangular_loop_inductance(l, w, r_w)
    mu0 = 4 * pi * 1e-7; % Permeability of free space

    term1 = -(l - r_w) * asinh((l - r_w) / (w - r_w)) - (w - r_w) * asinh((w - r_w) / (l - r_w));
    term2 = (l - r_w) * asinh((l - r_w) / r_w) + (w - r_w) * asinh((w - r_w) / r_w);
    term3 = r_w * asinh(r_w / (w - r_w)) + r_w * asinh(r_w / (l - r_w));
    term4 = 2 * sqrt((l - r_w)^2 + (w - r_w)^2) - 2 * sqrt((w - r_w)^2 + r_w^2);
    term5 = -2 * sqrt((l - r_w)^2 + r_w^2) - 2 * r_w * log(1 + sqrt(2)) + 2 * sqrt(2) * r_w;

    L_loop = (mu0 / pi) * (term1 + term2 + term3 + term4 + term5);
end
```

C

Results expanded

This appendix contains the PRPD patterns where the magnitude corresponds to the apparent charge found through the respective charge estimation method.

C.1. PRPD Charge Estimation Methods

C.1.1. qIEC

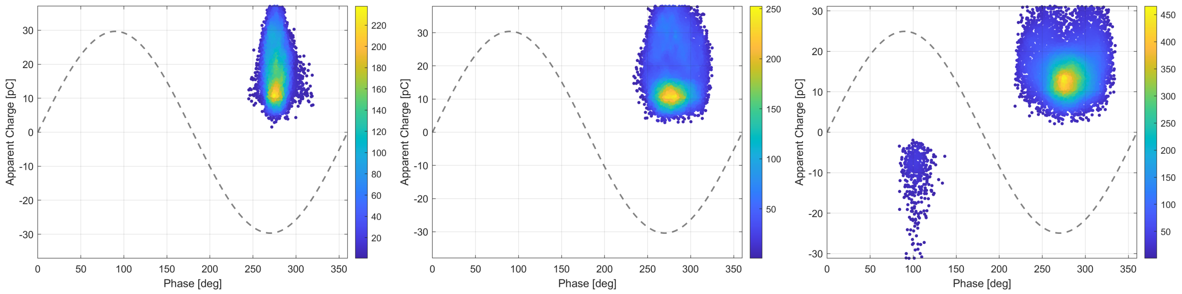

(a) **(b)** **(c)**

Figure C.1: PRPD patterns for CO_2/O_2 mixture at 0.2 MPa, measured at a voltage of (a) 100%, (b) 120% and (c) 150% PDIV. Charge Magnitude evaluated using the IEC method.

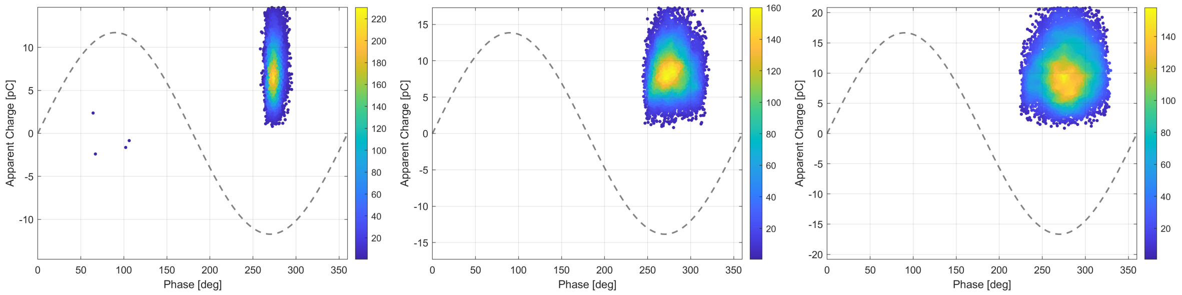

(a) **(b)** **(c)**

Figure C.2: PRPD patterns for CO_2/O_2 mixture at 0.3 MPa, measured at a voltage of (a) 100%, (b) 120% and (c) 150% PDIV. Charge Magnitude evaluated using the IEC method.

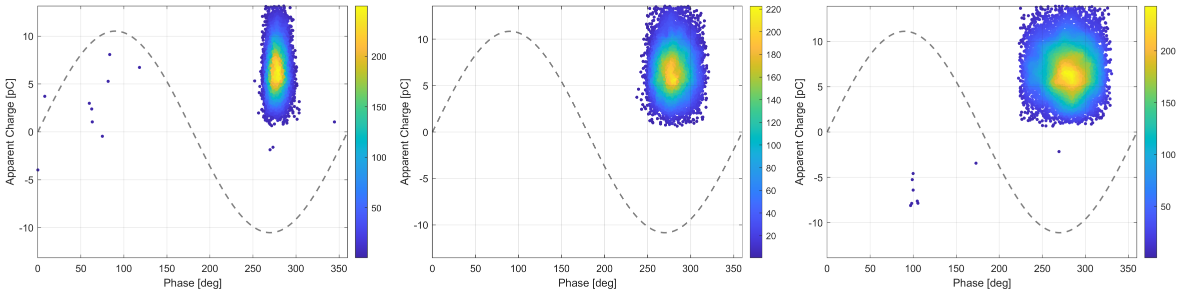

(a) (b) (c)

Figure C.3: PRPD patterns for CO_2/O_2 mixture at 0.4 MPa, measured at a voltage of (a) 100%, (b) 120% and (c) 150% PDIV. Charge Magnitude evaluated using the IEC method.

C.1.2. qTime

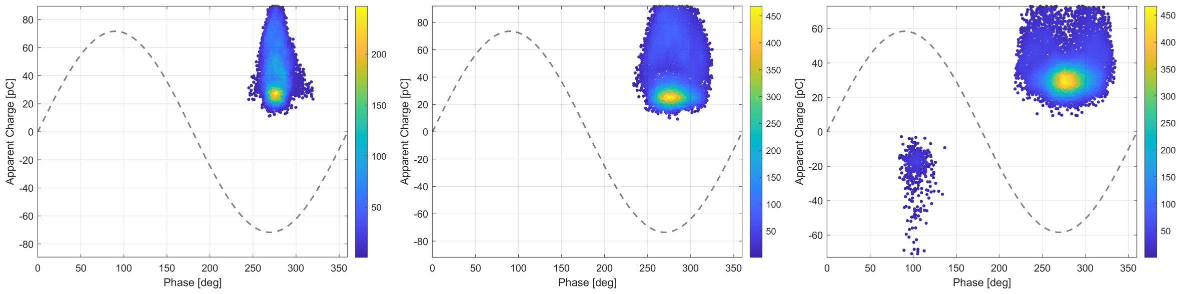

(a) (b) (c)

Figure C.4: PRPD patterns for CO_2/O_2 mixture at 0.2 MPa, measured at a voltage of (a) 100%, (b) 120% and (c) 150% PDIV. Charge Magnitude evaluated using the Time method.

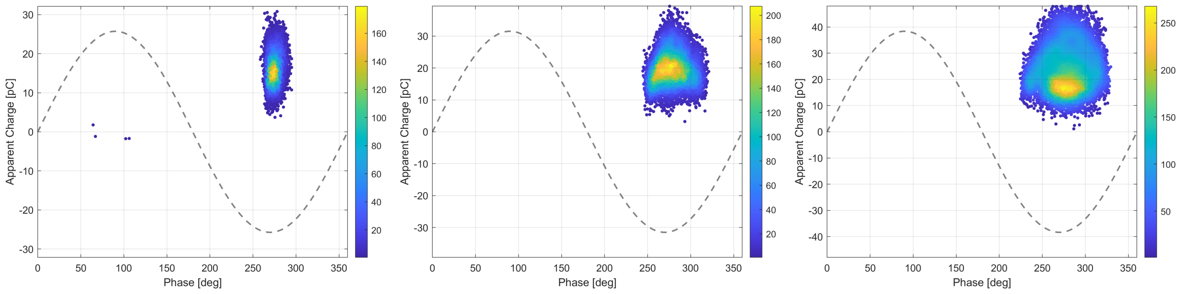

(a) (b) (c)

Figure C.5: PRPD patterns for CO_2/O_2 mixture at 0.3 MPa, measured at a voltage of (a) 100%, (b) 120% and (c) 150% PDIV. Charge Magnitude evaluated using the Time method.

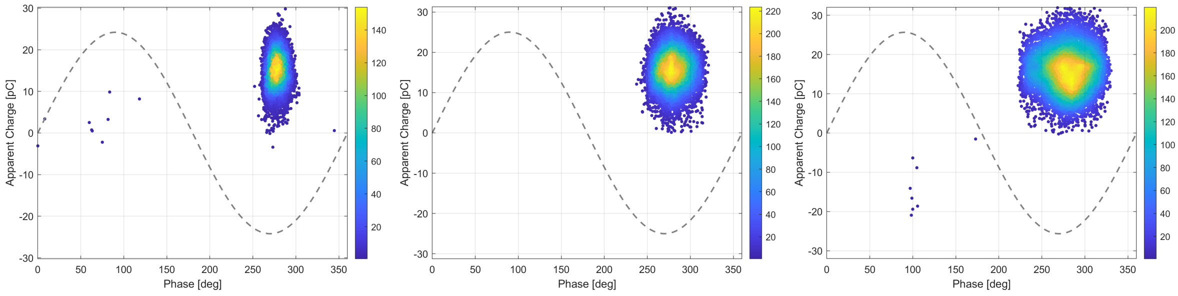

(a) **(b)** **(c)**

Figure C.6: PRPD patterns for CO_2/O_2 mixture at 0.4 MPa, measured at a voltage of (a) 100%, (b) 120% and (c) 150% PDIV. Charge Magnitude evaluated using the Time method.

C.1.3. qFreq

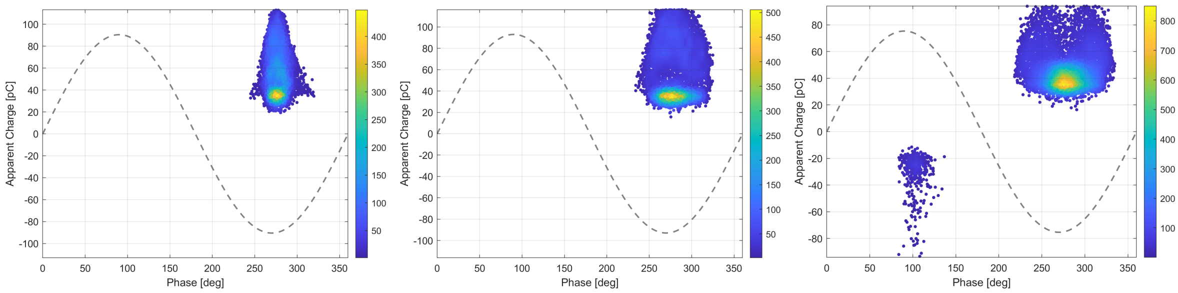

(a) **(b)** **(c)**

Figure C.7: PRPD patterns for CO_2/O_2 mixture at 0.2 MPa, measured at a voltage of (a) 100%, (b) 120% and (c) 150% PDIV. Charge Magnitude evaluated using the Freq method.

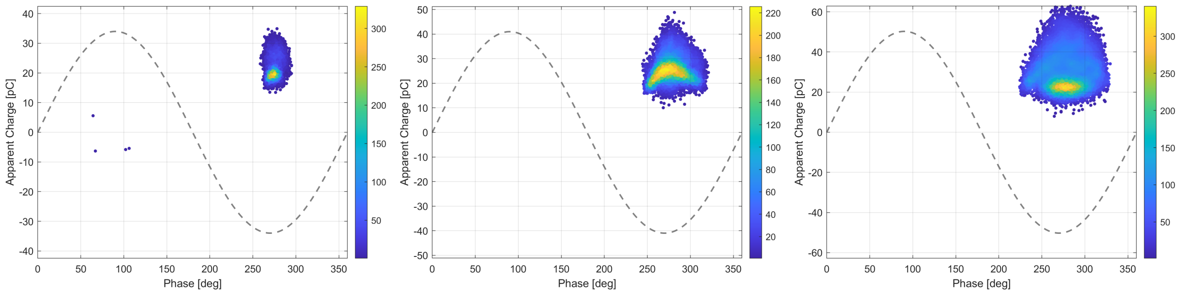

(a) **(b)** **(c)**

Figure C.8: PRPD patterns for CO_2/O_2 mixture at 0.3 MPa, measured at a voltage of (a) 100%, (b) 120% and (c) 150% PDIV. Charge Magnitude evaluated using the Freq method.

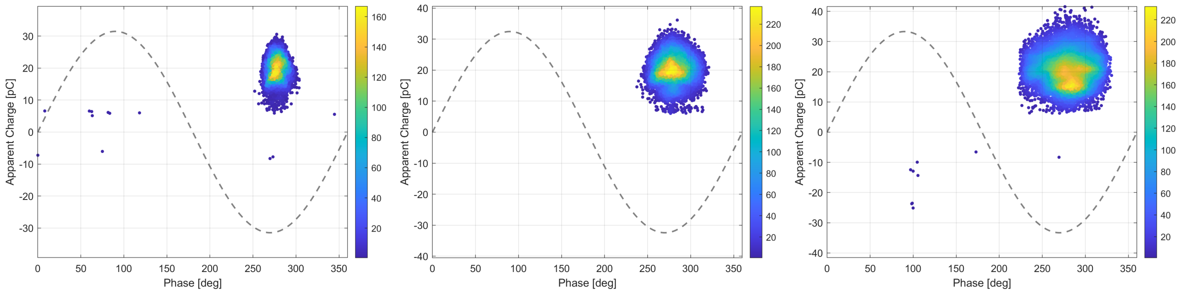

(a) **(b)** **(c)**

Figure C.9: PRPD patterns for CO_2/O_2 mixture at 0.4 MPa, measured at a voltage of (a) 100%, (b) 120% and (c) 150% PDIV. Charge Magnitude evaluated using the Freq method.

C.2. Cross-correlation Charge Estimation Methods based on Δt selection

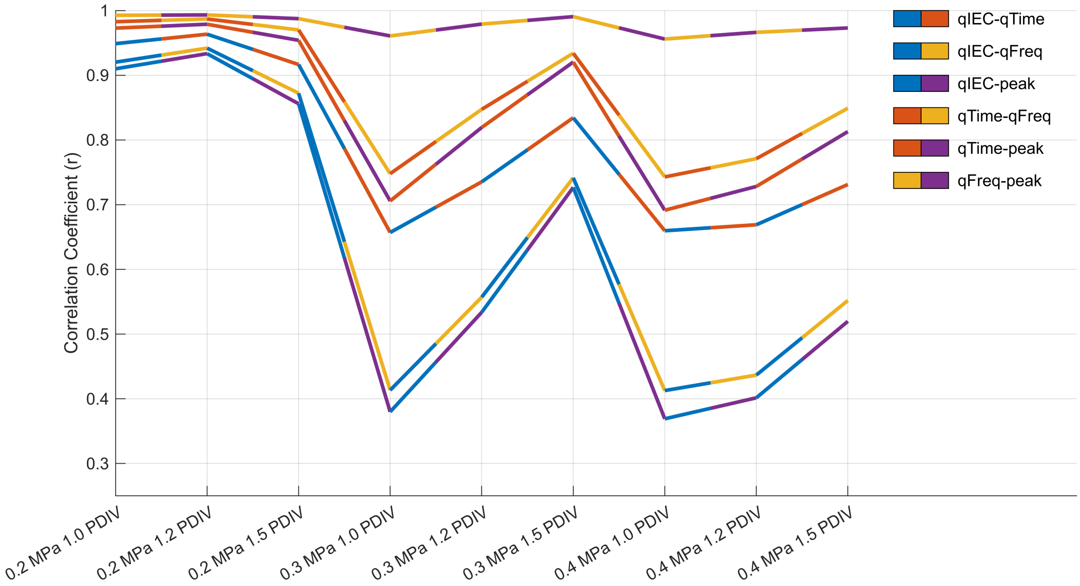

Figure C.10: Cross correlation between all charge estimation methods for pulses above the Δt selection treshold

C.3. Negative cycle Δt vs Charge Magnitude

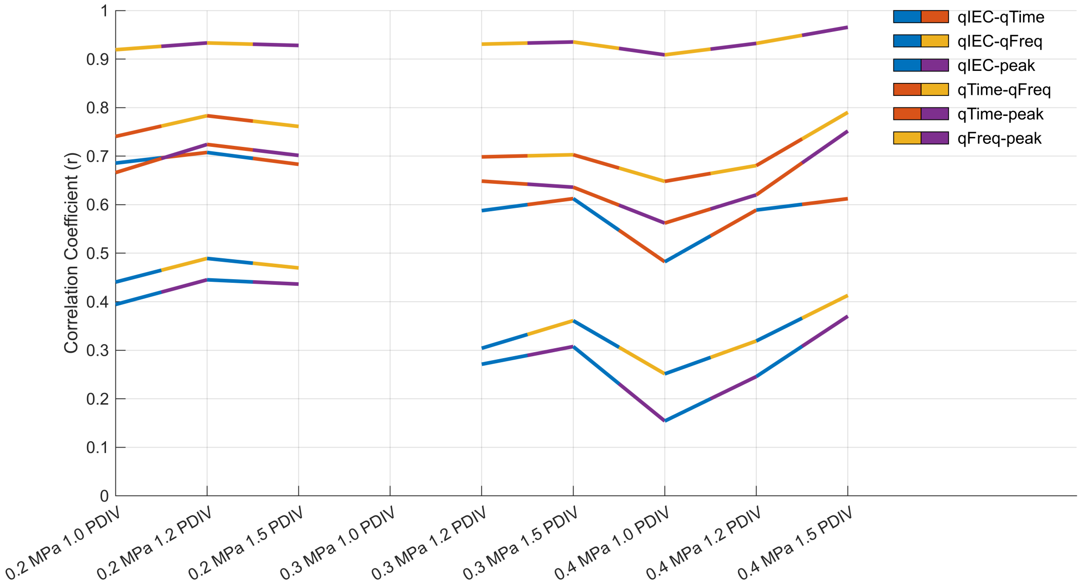

Figure C.11: Cross correlation between all charge estimation methods for pulses below the Δt selection treshold

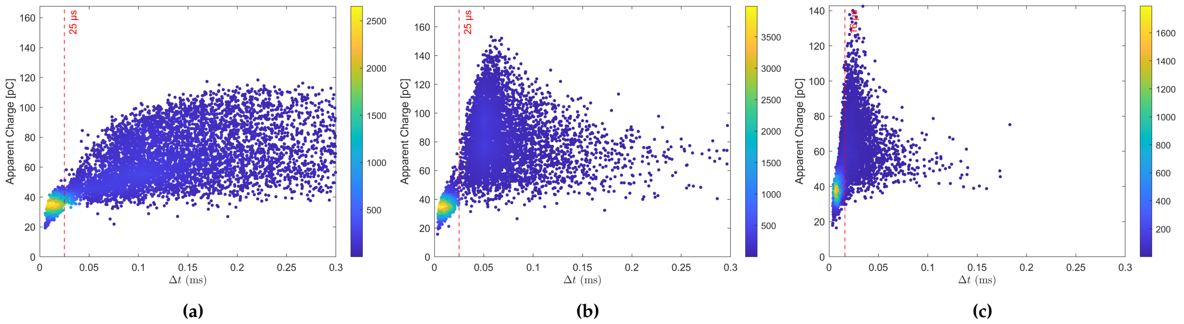

(a)

(b)

(c)

Figure C.12: Charge magnitude (q_{Freq}) vs Δt for CO_2/O_2 mixture at 0.2 MPa, measured at PDIV of (a) 100%, (b) 120%, and (c) 150%.

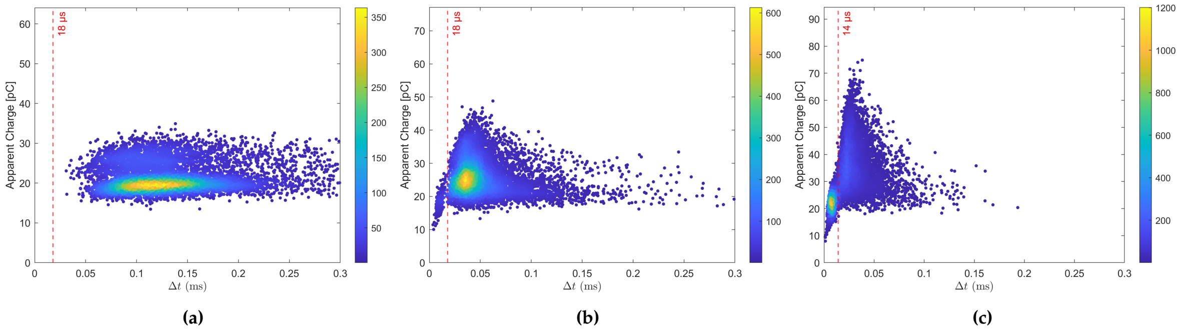

(a)

(b)

(c)

Figure C.13: Charge magnitude (q_{Freq}) vs Δt for CO_2/O_2 mixture at 0.3 MPa, measured at PDIV of (a) 100%, (b) 120%, and (c) 150%.

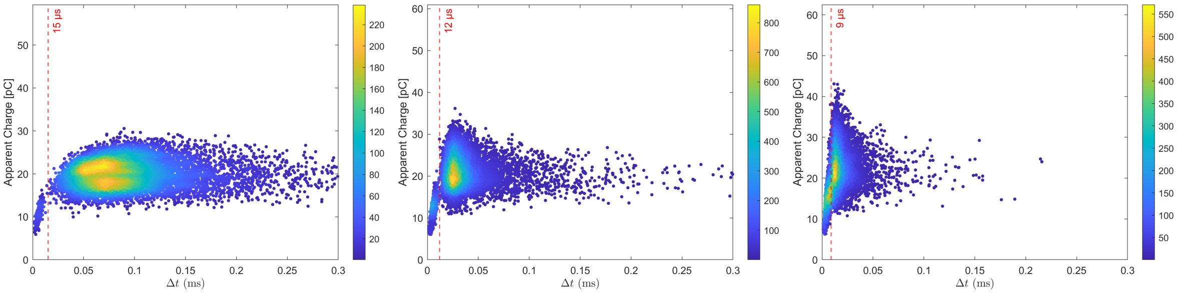

(a) **(b)** **(c)**

Figure C.14: Charge magnitude (q_{Freq}) vs Δt for CO_2/O_2 mixture at 0.4 MPa, measured at PDIV of (a) 100%, (b) 120%, and (c) 150%.